UiO : Institute of Theoretical Astrophysics
University of Oslo

A Modular Framework for Studying Neutron Star Structure and Cooling

With Dark Matter Applications

Jakob Borg

Master's Theses, Spring 2021

Thesis submitted for the degree of Master of Science in Astronomy.

Cover credit: Renate Røsæg.

[1] www.publiclibraryofscience.org

Abstract

Numerical modeling of neutron star cooling under full general relativity is treated with a new numerical framework in Python, capable of describing both neutron star structure and cooling for a given equation of state (EoS). The framework is developed with a heavy emphasis on flexibility and modular, simple code, facilitating both easy expandability in a gradual and consistent fashion, and simple comparison of a wide range of different models. The ease of using the framework to study and learn about neutron stars, combined with the simple way of including new physics to the model in the logically structured code, probably makes the framework one of a kind. Multiple EoS models are developed, and results obtained for both structure and cooling are in good agreement with qualitative and quantitative comparisons to other detailed works. We've also applied the most realistic models found to a cooling scenario including an exciting temperature-independent heating mechanism driven by annihilation of dark matter particles (WIMPs) in the interior, resulting in a stable minimum temperature plateau for neutron stars that has cooled for timescales of $t \sim 10^7$ yrs.

Acknowledgments

I originally nicknamed this thesis *'How Neutron Stars are so Cool'*, intended as a cheap pun, but also to be quite descriptive and reflect my newly acquired fascination for these stars. I didn't know particularly much about neutron stars beforehand, and I would like to thank my supervisor Øystein Elgarøy for providing me with such an interesting, *cool* and fulfilling master project. Thank you for guiding me along the way, answering all my questions, taking me seriously, and meeting with me every week for conversions I always looked forward to during this year. I could not have asked for a better fit. Thanks to Øystein, I've now heard many funny stories and fascinating «inside information» normally only encountered through years of experience in the field.

A big thanks also go to Morten Hjort-Jensen, for taking the time to meet with us and answer our questions regarding the more recent developments in particle and quantum mechanical many-body simulations, and single out some very useful articles describing some promising equations of state from the last 20 years.

All these years at the University of Oslo have been made much more fun and tolerable thanks to the wonderful friends I've made along the way. First to all the people at *Origo*, and more recently, thanks to my companions in the *Stellar Cellar* at the Institute of Theoretical Astrophysics, for many long nights and discussions – both in the name of science and otherwise. In particular, I would like to mention my close friends with whom I've shared a cubicle over the last years, Daniel Heinesen, Jonas G. S. Lunde, and Julie Thingwall.

Finally, to those I consider family. Dead or alive, you know who you are and what you mean to me. Thanks for letting me go on extended monologues regarding topics you didn't necessarily ask or care for, and reminding me of the other joys of life outside the logic and rationality of physics. My most sincere thanks and love goes to Renate Røsæg, whom I cannot function properly without.

Jakob

Contents

List of Figures

List of Tables

Chapter 1

Introduction

1.1 What is Cosmology?

Cosmology, in my opinion, is the most awesome field of any of the natural sciences. I mean that quite literally, as it by definition is the science of the entire Universe as a whole. All of space, all of time. Cosmologists try to answer the really *big* questions, like – how did the Universe begin? Will it ever end, and if so, how? And how did the Universe evolve to be as beautiful, stunning, and interesting as we observe it to be?

I'm of course a bit biased in saying that, as I've spent several years trying to become a cosmologist. What you are reading now is the culmination of seven years of studies at the University of Oslo. To treat the entire Universe, we first have to take a step back from the tiresome nitpicky details of everyday life and consider the bigger picture. In the language of mathematics, that means we describe the contents we observe in the Universe from a statistical perspective. The quantitative formulation of that perspective is in turn based on how we know the Universe to behave on smaller scales here on earth, for which we have empirical experimentation and evidence to support. Over the last century, the fields of cosmology and astrophysics have developed into a precision science, by combining the high degree of accuracy in observations using modern telescopes and the raw computational power of modern computers. Through statistical analysis of large amounts of observational data, cosmologists are able to quantitatively constrain the uncertainty in the claims and consequences put forward by their theories, revealing some strange components of our Universe we don't fully understand, appearing to only be noticeable when considering sufficiently large scales. And so, in our quest to answer the really big questions there seems to be a rabbit hole around every corner. When we think we are close to an answer, we are instead faced with new and quite often even more interesting questions. To strengthen our understanding we then have to delve back into the details in a search for more observable phenomena that might reveal or clarify some aspects of the laws and properties of the Universe. Needless to say, to study

the whole Universe, cosmologists have to apply a wide range of physics. In order to understand the large scales, described by Einstein's theory of general relativity, we also have to understand the small scales of particle physics and quantum mechanics. And that is where this thesis belongs, in an effort to conclude some behavior on the small scales of neutron stars, which we can later apply on the larger scales of the Universe. In the process we also wish to convey our fascination and intrigue for these objects, living an extreme life on the edge of what the laws governing our Universe allow.

1.1.1 Why Neutron Stars?

The stars in the Universe age, evolving over time as their interior particle composition is gradually transformed by fusion reactions made possible by the immense density and temperature set up by the large gravitational forces in their cores. Stars a few times larger than our Sun end their lives in spectacular supernovae, possibly outshining entire galaxies. This gradual evolution and explosive finale will be left untouched in this thesis, but if the initial star is not too massive, a neutron star is the final product after the supernova.

Neutron stars are the most compact type of star we have observed in the Universe. As we'll get back to, they are so compressed as to be dangerously close to collapsing onto themselves and turning into black holes. In addition, neutron stars are in fact «dead» stars, in the sense that the mentioned fusion reactions of normals stars are no longer maintained. Therefore they don't have the same source of internal energy production and are cooling over time. This is the main topic of this thesis, the study of neutron star cooling.

By comparing simulated cooling curves, that is the time evolution of temperature, to the observed temperature, age, mass, and radius of neutron stars out there in the Universe, we may put constraints on - or even rule out - some of the theories used to describe such dense systems. Thus, neutron stars serve as an excellent astronomical laboratory for studying how the laws that govern our Universe cause matter to behave under extreme densities and energies. Both on small scales regarding what types of particle compositions we expect to find in neutron stars, and on slightly larger scales regarding the stability of small gravitationally bound systems. And finally, as we'll get to in due time, we inspect how we might infer tests for on one of the most popular dark matter particle *candidates* - physics originating from the large scale modern cosmology - by comparing our resulting cooling curves to observations of old and cold neutron stars.

1.2 The Scope of this Work

As the title of this thesis entails, our goal has been to develop a flexible and modular framework for studying both neutron star structure and cooling, which also is easily expandable to include more and exciting physics in the future through logically structured code, designed to compare and learn from the many intricate relationships encountered in neutron stars. Here we summarize the overarching assumptions and approximations defining how we model the system:

- Assume a spherical symmetric, non-rotating neutron star. Thus the entire star is completely described by one-dimensional radial profiles, as illustrated in fig. 1.1. Throughout the thesis we'll only refer to these profiles, while imagining the rest of the sphere in three dimensions.
- Assume a static interior, thus the balance of gravity and pressure is described in hydrostatic equilibrium, with no internal velocity fields. That means also no heat transfer by convection.
- As a basis for particle composition we initially assume a gas of pure neutrons, thought to be a rough but relatively accurate approximation for a basic neutron star. As we'll see, the actual particle composition, and the behavior of these particles under the immense pressure in neutron stars, are still uncertain. This is one of the main reasons for the expandable nature of the code, as it's the way we model how the particles behave, and the types of particles present, that effectively is the main variable of the calculations.

1.3 Organization of the Thesis

The problem at hand, how neutron stars cool over time, is threefold. To have any actual stars we can study the cooling process of, we first of all need models describing the one-dimensional structure profiles of neutron stars. This in turn is divided into two distinct categories: the macroscopic, how distributions of matter in the Universe behave and respond to gravity and motion on large scales; and the microscopic, how individual components, or particles, of the said matter distribution contribute to local thermodynamical properties like pressure and emissivity. Thus we can separate the problem into three pieces, and this grouping by threes will be evident throughout.

The thesis is organized to reflect the process of the workflow, as close as possible. Our general strategy may be summarized as follows: Start with a simplified description of the eventual system we want to model, working as a basic test case for numerical methods and comparison to later more realistic descriptions. Then gradually expand

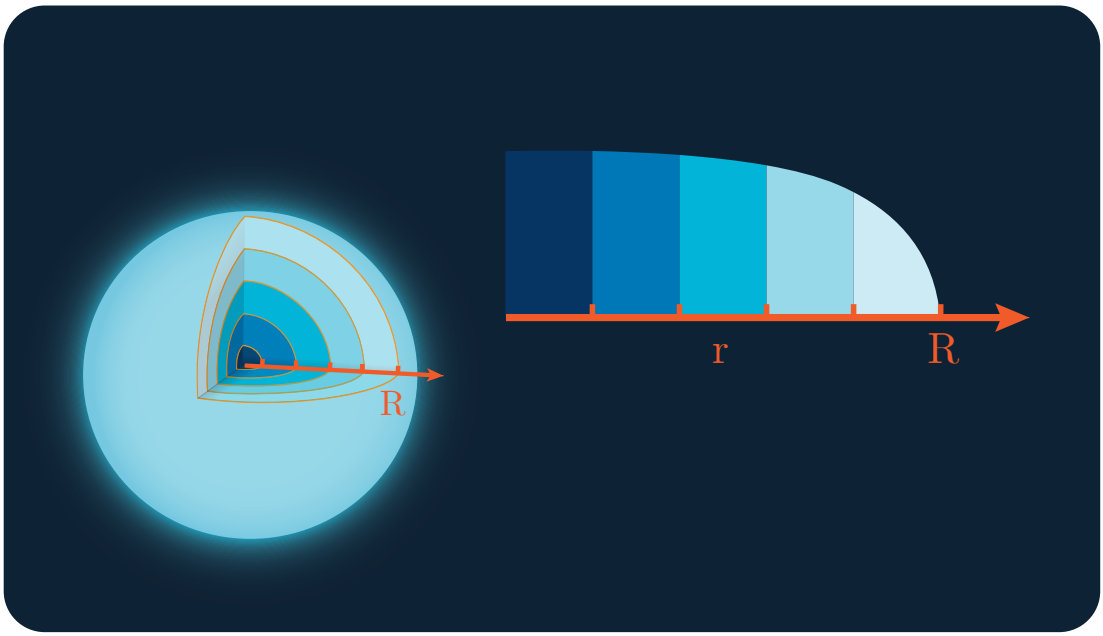

Figure 1.1: Schematic of spherical symmetry and one-dimensional radial profiles, completely describing the neutron star and its interior. The profile may again be described as many small homogenous volume cells where the physical quantities change from the core to the surface. In the profile we see on the right, the size of the individual cells is not to scale, but the actual shape of the continuous curve along the top is based on results obtained with our framework, and the color gradient indicate decreasing density. Figure credit: Renate Røsæg.

upon the simplified case, learning from the effects and changes of individual improvements to the model. As such, the conventional format of most scientific papers is intentionally avoided. Instead, we've tried to produce a more pedagogical structure. In part I we lay out all the relevant equations needed to describe neutron stars and how they cool, largely based on Shapiro and Teukolsky (1983). Each of the three mentioned pieces of the puzzle has been devoted separate chapters, with a gradual build-up of complexity. Hopefully, even with little background from physics, most readers will be able to follow at least the opening sections of each chapter. In part II we describe how we've implemented the theory in our modular numerical framework in Python, again divided into the three distinct pieces, albeit with an additional fourth chapter describing some general structure of the code. Here we wish to convey the rather intricate connections between the different parts, and hopefully the amount of work that has been done in order to make this framework as consistent, flexible, and expandable as possible. Finally, in part III, we include some results of the many possible neutron stars we are able to simulate with our framework, and try to summarize some general conclusions and learning outcomes, as well as future prospects and possibilities.

As a heads up if you're easily spooked by a lot of equations . . . there's gonna be quite

a lot of equations. Therefore, we've included some of our produced figures and results as a visual reference of the types of quantities we are discussing in each chapter. For this, we've mostly used intermediate results from some of the simpler stages of development, intended as pedagogical illustrative examples for the reader – just like they helped me get a better grip of the various physics involved along the way.

All of the graphs we'll encounter in this thesis are made with the accompanied plotter functionality of the framework, mainly developed to compare and test the models alongside the implementation. As such the legends describing the contents of each plot is formatted automatically in the way it's intended to be used on multiple models at once, where the relevant parameters and model names are described using acronyms. Some of the ones we'll encounter the most are listed here.

TOV	Tolman-Oppenheimer-Volkoff
Sch	Schwarzschild scaling
EoS	Equation of state
poly	Polytropic EoS
QMC	Quantum Monte Carlo
cgs-units	Centimeter-gram-second unit system
RHS	Right hand side (of an equation)

Part I

Theoretical Foundation, How We Describe Neutron Stars

Chapter 2

Crash Course in Stellar Structure Theory

The life and death of stars are governed by gravity, and the balance between gravity and pressure. Gravity is the cause of their initial formation from sparse clouds of gas into energy-efficient fusion reactors illuminating the Universe, and is also the cause of their eventual demise. For stars turning into neutron stars, gravity continues to dominate their lives. Neutron stars are nature's final defense against the crushing force of gravity, and the most compact configuration matter in the Universe may be compressed into before imploding, forming a black hole. To model stellar structure we need a thorough understanding of the balance of gravity and pressure, starting with Newtonian gravity in section 2.1. For the extreme gravitational fields in neutron stars we really have to include relativistic effects from Einstein's general theory of relativity, which modifies the Newtonian description in section 2.2. Opposing gravity is the outwards force induced by the pressure of matter and radiation. In this chapter we merely assert how the equations for pressure must be to balance the force of gravity. The characteristics of the corresponding matter distribution are left for chapter 3, where we explore our limited understanding of how matter behaves when reaching these extreme densities.

Full treatment of stellar structure involves Euler's fluid equations for conservation of mass, energy and momentum in three dimensions, including magnetohydrodynamic effects. As we are mainly investigating neutron star cooling, we simplify the structural picture to be non-rotating, spherical symmetric, and without internal velocity fields. Thus, we only need to consider hydrostatic physics and equations. As mentioned, our goal for this chapter is to determine the equations needed to model the one-dimensional structure profiles. Along the way, fig. 2.1 demonstrates the resulting profiles for Newtonian neutron stars of four different core densities, solved with our framework.

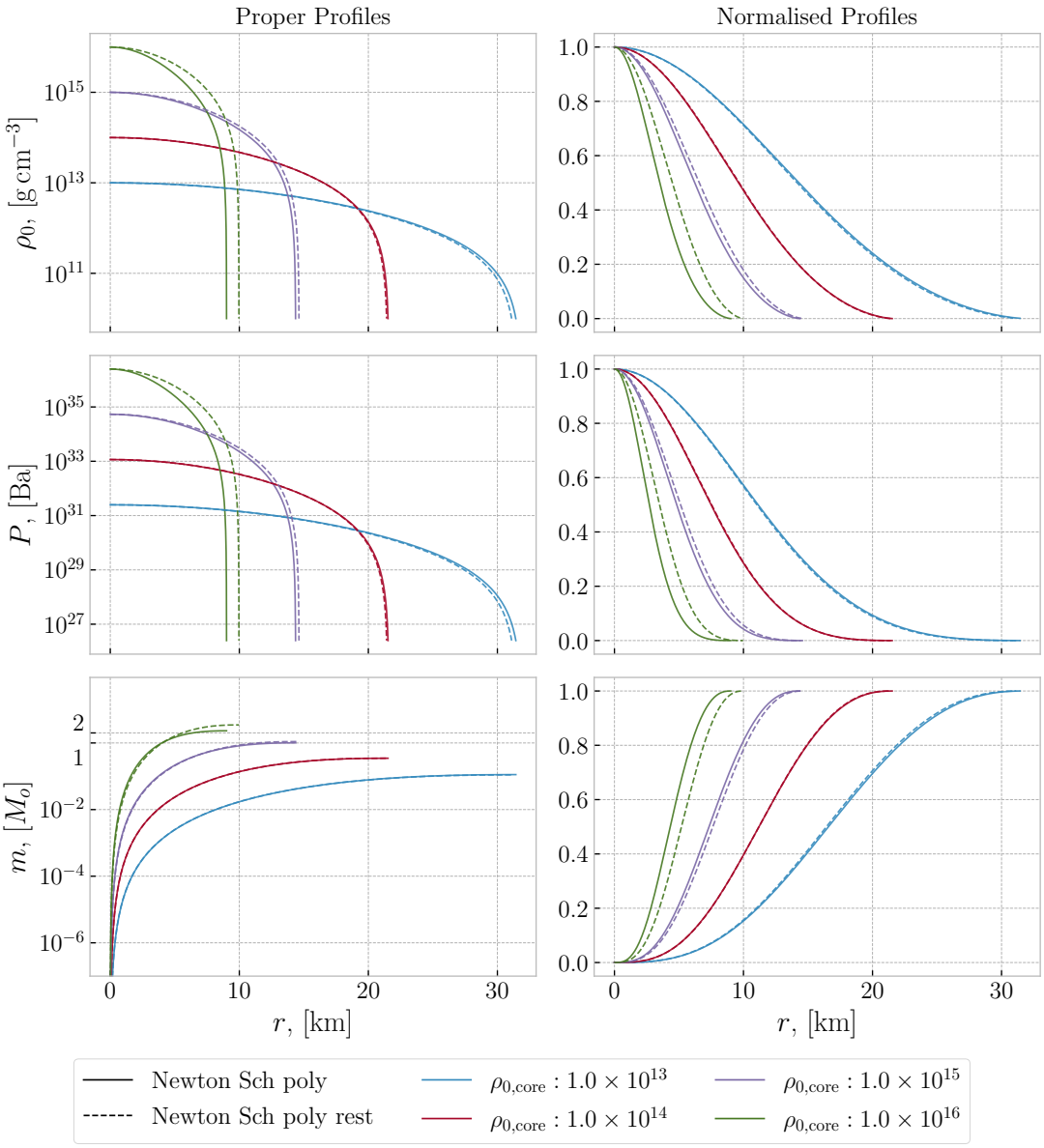

Figure 2.1: Demonstrative example of structure profiles for density, pressure, and mass as functions of radius, solved with Newtonian gravity. The full profiles are shown to the left, with cgs-units for pressure and density, and the mass measured in solar masses. To the right are the appropriately normalized profiles. Four different values for the core density are shown, illustrating the effect of varying core density – resulting in neutron stars with rather different total mass and radius. These models employ the polytropic equation of state [cf. sections 2.1.1 and 7.2 and chapter 3].

2.1 Newtonian Stellar Structure

For a star to be stable against self-gravitating collapse, the massive inwards force of gravity must be countered by an equal outwards pressure force. For models with static interiors, such as ours, one can solve for the one-dimensional structure of the star at any time by balancing these forces radially throughout the profile from the core to the surface. As long as the net force acting in each volume element of the star is zero, the star is in equilibrium. As a first cause of action, we brush up on our knowledge of gravity as Newton formulated it.

Newton's law of universal gravitation is the first approximation to quantitatively describe the gravitational attraction between two bodies of mass m and M. In this picture gravity is an ordinary *force* acting on both objects, described as

$$\vec{\mathbf{F}} = -G\frac{mM}{r^2}\hat{\mathbf{r}}, \tag{2.1}$$

where G is the familiar gravitational constant, r is the distance between the two bodies' respective centers of mass, and $\hat{\mathbf{r}}$ is the unit vector pointing between the two bodies describing the direction of the force. For our purposes it's more useful to express the gravitational effect the stars have on themselves through the gravitational potential, $\phi = \phi(r)$, given by Poisson's equation for Newtonian gravity

$$\nabla^2\phi = 4\pi G\rho, \tag{2.2}$$

where $\rho = \rho(r)$ is the mass density and ∇^2 is the Laplace operator. The potential fully describes the gravitational force acting throughout the profile of the star as a scalar field, thus being more convenient to work with. For a spherical symmetric field and using spherical polar coordinates, the only nonzero component of the gradient $\boldsymbol{\nabla}\phi$ is the radial part, $d\phi/dr$. As such we can fully express the Newtonian gravitational potential as

$$\frac{d\phi}{dr} = \frac{Gm}{r^2}, \tag{2.3}$$

where $m = m(r)$ is interpreted as «the cumulative mass inside radius r» and is given by

$$\frac{dm}{dr} = 4\pi r^2\rho. \tag{2.4}$$

Note the familiar result from Newtonian theory, that the gravitational field a distance r from the center of a spherical distribution is solely determined by the mass interior to that point. Equation (2.4) may be solved for the total mass, $M = m(R)$, of a star with radius R as

$$M = \int_0^R 4\pi r^2\rho\, dr\,. \tag{2.5}$$

Now, for the star to be in equilibrium the gravitational force must be balanced by a pressure force, or in other words a pressure gradient, at every point through the profile.

Thus, we must have

$$\frac{dP}{dr} = -\rho\frac{d\phi}{dr} = -\rho\frac{Gm}{r^2}, \tag{2.6}$$

where $P = P(r)$ is the pressure. This way the inwards attraction due to the gravitational potential is exactly balanced by the outwards pressure gradient, and the interior is in equilibrium. We have now introduced all the fundamental variables we need to describe the structure profile of our modeled neutron stars: mass, density, pressure, and radius.

2.1.1 Forming a Closed System

Equations (2.3), (2.4) and (2.6) forms the coupled equations governing the stellar structure in Newtonian hydrostatic equilibrium. They describe the mass and gravitational potential, along with the counterbalancing pressure, all as a function of radial distance from the core. However, as an observant reader may have noticed, we seemingly have no equation for the actual density. With four fundamental variables, and only three equations, the system is per definition open – there is no *one* unique solution to be found. To close the system we need one more equation, a relation between the pressure and density

$$P = P(\rho).$$

This is called the equation of state (EoS), describing the resulting pressure in a system due to its density (or vice versa). This relation is of huge importance in close to all branches of physics, used to determine the fundamental state of matter distributions in a given configuration.

This is by far the most uncertain piece of the theory regarding neutron stars that is relevant under our assumptions. Over the last century since Einstein (1915) published his masterpiece, *general relativity*, the theory has been extensively tested and confirmed by the rest of the scientific community. Attempts have been made, and are continuously worked at, to disprove Einstein and give alternating explanations for some of the uncomfortable consequences of applying his theory to the whole Universe, where we've discovered the need for substances like dark matter and dark energy to explain the reality we observe around us. So far these alternative theories have had little success at describing as many of the different ways our universe behaves equally successfully as Einstein's theory does. As such, the theory described in this chapter, with emphasis on the remaining relativistic version in section 2.2, is broadly accepted as correct among most physicists today and based on Hobson et al. (2006); Shapiro and Teukolsky (1983). Thus, when studying neutron stars, the main «variable» is in fact how we choose to model the EoS, which we'll come back to in chapter 3. First, let's take a look at how we must adjust the classical theory to account for relativity, and try to understand why.

2.2 Relativistic Hydrostatic Equilibrium

Neutron stars are quite lightweight compared to black holes or other massive stars such as giants or supergiants. Their suggested typical mass is within one or a few solar masses $M_\odot$ [cf. table A.1]. What makes neutron stars stand out in a crowd is their density. While the mass is comparable to our sun, the typical radii of neutron stars are $\sim 10\,\mathrm{km}$, approximately 7×10^{-4} times that of the solar radius $R_\odot$. The relatively high mass compressed into a sphere of such low radii generates so strong gravitational fields that relativistic effects from Einstein's theory of general relativity must be considered. To put the so-called *supernuclear* densities of neutron stars in perspective, we can do some rough estimates. Assuming the average weight of a human to be $\sim 70\,\mathrm{kg}$, and the number of people alive on earth today to be ~ 7.9 billion $\left(7.9 \times 10^9\right)$,[1] the total mass of everyone combined is $\sim 5.5 \times 10^8$ tons – that is $550\,000\,000\,000\,\mathrm{kg}$. But if we wanted to squeeze every single human into a sphere of similar density to neutron stars $\sim \rho_{\mathrm{nuc}}$, the radius of that sphere would only be about $0.8\,\mathrm{cm}$.

2.2.1 Spherical Symmetric Gravitational Fields

In general relativity, gravity is treated as a geometric property of a manifold, the four-dimensional spacetime, described by the metric tensor $g_{\mu\nu}$. The matter and energy contained in a region of spacetime bend and distort the temporal and spatial coordinates of the manifold, forming a curved spacetime where time dilation and length contraction are results of the intrinsic geometry. The line element, ds, then gives the proper interval between *events*[2] in spacetime, defined as

$$ds^2 = g_{\mu\nu}\, dx^\mu\, dx^\nu\,, \tag{2.7}$$

following Einstein's summation convention. In contrast to the metric tensor, the line element is a scalar quantity. Equation (2.7) is nevertheless a *tensor* equation, meaning it must hold in any reference frame – as long as we transform the tensors on the right-hand side appropriately.[3] Independent of reference frame, the contraction over the component pairs μ and ν results in the same line element, thus ds is invariant under any coordinate transformation. For a spherical symmetric gravitational field, we can conveniently choose spherical polar coordinates as

$$x^0 = ct, \quad x^1 = r, \quad x^2 = \theta, \quad x^3 = \phi,$$

[1] According to worldometers.info, last checked 14.06.2021.

[2] An event describes a single point in the four-dimensional manifold, by specifying three spatial coordinates and one time coordinate.

[3] We are constraining the discussion here to the parts relevant for the eventual hydrostatic equilibrium equations, that is the line element. Proper definitions of tensors and how they transform in general relativity is not included, but we'll like to point out the rather amusing qualitatively descriptive definition often encountered when first learning of tensors: «A tensor is a mathematical object that transforms and behaves like a tensor.»....

where c is the speed of light, acting as a «bridge» connecting the spatial and temporal coordinates. Then, the metric and the line element are completely described by the time and radial coordinates, t and r. Distances along a sphere of the same radius at a given time, angular distances, can be found through the combination $d\Omega^2 \equiv d\theta^2 + \sin^2(\theta)\, d\phi^2$. This is not as relevant in our case, as we model the star as a one-dimensional radial profile, but we still include it here to showcase the general approach to working with the line element.

The most general spherical symmetric metric gives, after some manipulation, a general line element as

$$ds^2 = -A(t,r)\, dt^2 + B(t,r)\, dr^2 + 2C(t,r)\, dt\, dr + D(t,r)\, d\Omega^2\,, \tag{2.8}$$

where the metric coefficients A, B, C and D are arbitrary functions of t and r. As the line element is invariant, we know there exists a reference frame where the radial coordinate is described as

$$r'^2 = D(t,r).$$

Assuming we perform this transformation we can eliminate the arbitrary coefficient for the angular part. Renaming the new coordinate $r' \to r$ without the prime we have

$$ds^2 = -E(t,r)\, dt^2 + F(t,r)\, dr^2 + 2G(t,r)\, dt\, dr + r^2\, d\Omega^2\,, \tag{2.9}$$

where the new coefficients are functions of t and the new coordinate r, and are related to the coefficients in eq. (2.8) through the reverse transformation. We can also eliminate the G coefficient of the cross term $dt\, dr$ by the same logic in, choosing a new time coordinate defined through

$$dt' = H(t,r)[E(t,r)\, dt - G(t,r)\, dr], \tag{2.10}$$

where $H(t,r)$ is some function such that eq. (2.10) is a perfect differential. By this substitution we are left with only two metric coefficients

$$ds^2 = -\exp(2\Phi)\, dt^2 + \exp(2\lambda)\, dr^2 + r^2\, d\Omega^2\,, \tag{2.11}$$

where we again have dropped the prime, $t' \to t$, and written the coefficients on a more convenient form. Here Φ and λ are called the metric functions, and are in general functions of t and r.

The important result from Newtonian theory, that the gravitational field at any point outside a spherical distribution of total mass M depends only on the distance to the center of the distribution, is still valid in general relativity. It is then known as Jebsen-Birkhoff's Theorem, which states that the only spherical symmetric gravitational field in a vacuum[4] is static, and is called the Schwarzschild metric

$$ds^2 = -\left(1 - \frac{2GM}{c^2 r}\right) dt^2 + \left(1 - \frac{2GM}{c^2 r}\right)^{-1} dr^2 + r^2\, d\Omega^2\,, \tag{2.12}$$

[4]Hereby meaning an «empty» region of spacetime nearby a spherical symmetric gravitational source. Or a region where if any matter present, the gravitational field produced by said matter is negligible compared to the nearby source.

where M is the mass of the spherical source, $M = m(R)$. The Schwarzschild metric applies everywhere outside to the spherical mass, i.e. star, outside its surface, $r \geq R$.

The physical interpretation of the new coordinates is rather simple. At any radius r there exists a 2-sphere, or a two-dimensional spherical surface centered around the point $r = 0$, such that the proper circumference and area of the 2-sphere is $2\pi r$ and $4\pi r^2$ respectively. This can be shown, for example for the circumference of the 2-sphere, by setting the time and radial component to constants so the line element becomes just $ds^2 = r^2\, d\Omega^2$. Integrating the line element at a fixed $\theta = \pi/2$ around a closed path gives the physical measured circumference

$$\oint_{\theta=\pi/2} ds = \int_0^{2\pi} r\, d\phi = 2\pi r. \tag{2.13}$$

Note however, that along the radial direction[5], the proper distance between two points r_2 and r_1 is

$$\int_{r_1}^{r_2} ds = \int_{r_1}^{r_2} \left(1 - \frac{2GM}{c^2 r}\right)^{-1/2} dr \neq r_2 - r_1. \tag{2.14}$$

The time component is less relevant, determined by eq. (2.10). However, we don't really need to assign a physical interpretation. The resulting field is invariant under the transformation $t \to t + \Delta t$, emphasizing the stationary nature of the system. It's also normalized to be equal the Minkowski time coordinate in the weak field limit, $r \gg M$, where the whole metric reduces to the Minkowski geometry of special relativity. On the other end, in the limit $r \to R_\mathrm{S} = 2GM/c^2$, called the Schwarzschild radius for a body with mass M, the metric functions diverge, and the line element heads to infinity. If the surface of a massive body falls behind or touches this radius, the body will collapse and form a Schwarzschild black hole with an event horizon at R_S. Taking a neutron star of $M = 1\,\mathrm{M}_\odot$ and $R = 10\,\mathrm{km}$, the radius is only ~ 3.4 times larger than its Schwarzschild radius [cf. table A.2]. This is dangerously close to the limit of compactness our universe allows before forming an event horizon, effectively creating a region of spacetime from which we cannot extract information, a disjointed, one-way, dead-end for the exterior reality. Fortunately, neutron stars are able to form equilibrium, allowing us to study how matter in the Universe behaves when approaching the «edge of reality», albeit from a considerable distance instead of in the lab.

[5] Set the time and angular components to constants, so $ds^2 = \left(1 - 2GM/c^2 r\right)^{-1} dr^2$.

2.2.2 Adjustments from General Relativity

To accurately describe the gravitational potential throughout the profile of neutron stars we have to solve for the metric functions in eq. (2.11), where eq. (2.12) defines the required border values. By solving the full Einstein field equations for the metric coefficients inside the star, one can find two differential equations with respect to radius that must be satisfied by Φ and λ. For λ the equation takes the form

$$\left(1 - \frac{1}{\exp(2\lambda)}\right) + \frac{r\frac{d\exp(2\lambda)}{dr}}{\exp(2\lambda)^2} = \frac{8\pi G}{c^2} r^2 \rho, \tag{2.15}$$

or equivalently

$$\frac{d}{dr}\left(r - \frac{r}{\exp(2\lambda)}\right) = \frac{8\pi G}{c^2} r^2 \rho. \tag{2.16}$$

By integrating eq. (2.16) with respect to r, and using that the associated integration constant must be zero demanded by eq. (2.15), we find the solution for the metric function inside the interior given as

$$\exp(2\lambda) = \left(1 - \frac{2Gm(r)}{c^2 r}\right)^{-1}, \tag{2.17}$$

now evaluated at $r < R$, where R is the radius of the star, and $m(r) < M$ is the interior cumulative mass instead of the total mass. As the interior is static we can neglect the time dependency of the metric function.

For Φ the obtained differential equation must be solved numerically alongside the mass and pressure [cf. eq. (2.26)], and must match smoothly onto the exterior Schwarzschild metric at the surface, giving it a natural boundary condition

$$\Phi(r = R) = \frac{1}{2} \ln\left(1 - \frac{2GM}{c^2 R}\right). \tag{2.18}$$

Following the convenient notation by Thorne (1977), rewritten to replicate the stellar structure equations from Shapiro and Teukolsky (1983), the relevant relativistic corrections to the Newtonian theory is expressed in terms of the following four dimensionless variables

$$\mathcal{R}(r) \equiv \exp(\Phi) \tag{2.19}$$

$$\mathcal{V}(r) \equiv \exp(\lambda) = \left(1 - \frac{2Gm}{c^2 r}\right)^{-1/2} \tag{2.20}$$

$$\mathcal{G}(r) \equiv \left(1 + \frac{4\pi r^3 P}{c^2 m}\right) \tag{2.21}$$

$$\mathcal{H}(r) \equiv \left(1 + \frac{P}{\rho c^2}\right). \tag{2.22}$$

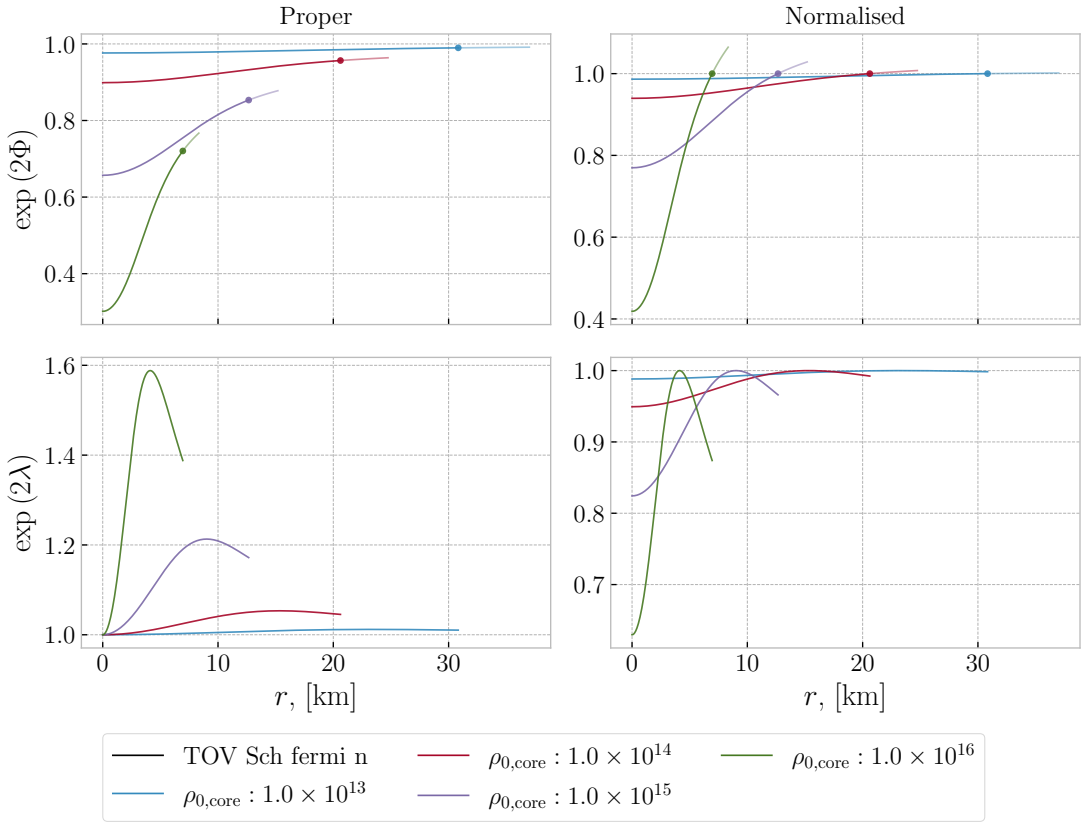

Figure 2.2: Demonstrative example of metric coefficients as functions of radius. The left column showing the proper solutions, with the normalized version to the right. The dot in the top row indicate the surface of the star where the metric match smoothly onto the exterior, included as the dimmer line extending to higher radii.

The full equations for stellar structure in general relativity are derived in most standard textbooks regarding the topic and are not included here. This notation emphasizes the correlation with Newtonian theory in a straightforward fashion. These factors constitute the relativistic effects of respectively gravitational redshift due to time dilation, volume correction due to length contraction, gravitational acceleration, and enthalpy corrections. All of which reduces to unity in the Newtonian limit.[6] Using these variables eq. (2.11) is expressed as

$$ds^2 = -\mathcal{R}^2 c^2\, dt^2 + \mathcal{V}^2\, dr^2 + r^2\, d\Omega^2\,. \tag{2.23}$$

We've included the resulting coefficients from one of our relativistic models in fig. 2.2,

[6]Note the subtle difference of Φ and ϕ following conventions from the field; ϕ is the standard Newtonian gravitational potential from eq. (2.3) while Φ is the analogous part in general relativity, which reduces to $\Phi \to \phi/c^2$ in the Newtonian limit.

to give some reference to the types of metric functions obtained at various densities. The figure also shows how the temporal coefficient matches onto the exterior metric at the surface of the star, indicated by the dot on the curves in the upper panels. The solid line showing the interior metric, and the dimmer line showing the exterior analytical metric.

We can then reproduce the relativistic stellar structure equations, often abbreviated to TOV (Tolman-Oppenheimer-Volkoff), by adding the appropriate factors to the Newtonian system of equations

$$\frac{dm}{dr} = 4\pi r^2 \rho \tag{2.24}$$

$$\frac{dP}{dr} = -\frac{Gm\rho}{r^2}\mathcal{HGV}^2 \tag{2.25}$$

$$\frac{d\Phi}{dr} = -\frac{1}{\rho c^2}\frac{dP}{dr}\mathcal{H}^{-1}, \tag{2.26}$$

where eq. (2.24) is unchanged from the Newtonian version, but with a subtle and important difference. For the mass density entering in eqs. (2.24) to (2.26) we have to remember Einstein's preceding theory of *special relativity* (Einstein, 1905), of which general relativity was built upon. One of the groundbreaking results of special relativity is Einstein's mass-energy equivalence – probably the most famous equation in all of physics

$$E = mc^2. \tag{2.27}$$

This equation merely states that mass and energy are two sides of the same coin, again linked by the fundamental constant for the speed of light, this time squared. However, the beloved equation written on this form is only strictly valid to describe the energy (or mass) of e.g. a particle in that particle's own *rest frame*, meaning a reference frame traveling along the path of the particle. Thus, the energy associated with the movement of the particle is not considered, and eq. (2.27) actually gives the *rest mass* of the particle (or equivalently the *rest energy*). The extension to describe the energy of particles in motion, often called the energy-momentum relation, is given as

$$E = \sqrt{(m_0 c^2)^2 + (pc)^2}, \tag{2.28}$$

where p is the momentum of the particle and m_0 is the mentioned rest mass. In the case of zero momentum, eq. (2.28) reduces to the more familiar form. We can still use eq. (2.27) to weigh composite systems' mass, by summing up relevant present energy contributions and dividing by c^2.[7] The density entering in eqs. (2.24) to (2.26) is therefore not only the rest mass density,[8] but may include contributions from various forms of energy through Einstein's mass-energy equivalence. The density can be expressed

[7] Relevant here is intentionally vague. More precisely, all energy that is attributed the object, and not the geometrical part of spacetime.

[8] The rest mass density takes the same role as the mass density did in the classical theory Newton knew.

as $\rho = \rho_0 + \rho_{\text{rel}}$, where we use ρ_0 to denote the rest mass density and ρ_{rel} is used to denote the additional mass-energy contribution. More conventionally we write the mass density as $\rho = \epsilon/c^2$, where ϵ is the full *energy density*.

Equations (2.24) to (2.26), combined with a chosen equation of state, forms the complete set of equations for spherical symmetric and static relativistic stellar structure. Equation (2.5) still gives the observable total mass of the star which enters in the Schwarzschild metric, provided we use the full mass density. This is not including the negative contribution from gravitational binding energy, which is energy attributed to the geometry of spacetime itself, not its content. This fact is somewhat hidden in the relatively simple appearance of the TOV equations, as there are no volume adjustments in eq. (2.24). To include the contribution from the negative gravitational energy, one has to use the proper volume element

$$d\mathcal{V} = \left(1 - \frac{2Gm}{c^2 r}\right)^{-1/2} 4\pi r^2 \, dr \tag{2.29}$$

instead of just $4\pi r^2 \, dr$.

We model the types of energies included through the choice of EoS, which we'll come back to in chapter 3. Without more details, we close out this chapter by hinting at the solid and dashed curves in fig. 2.1 – distinct for the higher initial densities, and restating that the relationship between mass and energy changes from classical to relativistic theory.

Chapter 3

Equation of State, The Microphysics

An equation of state (EoS) in physics and thermodynamics is an equation describing the *state* of matter under a given set of conditions. Expressed using this terminology it might not make much sense right away, but more or less everyone has some intuitive understanding of this rather complicated field – maybe even more than you know! First of all, what is matter? We have used this term quite freely in chapter 2, just assuming everyone is on par with its definition. In a nutshell, matter is everything made of «stuff» that has a nonzero rest mass, and occupy some volume in spacetime. Like a bicycle or a bird. Up close, stuff is molecules, atoms, and particles, like neutrons, protons, and electrons. Simply put, most «stuff» is matter. Massless particles, like photons, are usually not considered matter, but are rather categorized as radiation. As we'll see a particular example of in section 4.2.3, some types of matter are given special names because of the way they behave.

So an EoS describes the state of a given distribution of matter. For example, most people know that water is a liquid in temperatures between 0 °C and 100 °C. The matter distribution, in this case a volume of water, is then described as being in a liquid state and can be assigned an appropriate EoS. By changing the physical conditions, e.g. cooling the water, the state of the matter will change according to its EoS. If cooled sufficiently, the water turns into ice, changing its behavior quite dramatically. The water is now no longer a liquid, but a solid, and the matter must be described by a new EoS appropriate to the state of ice. When matter changes form like this, it's called a phase transition. Such transitions usually infer a discontinuous change in behavior, and are often quite tricky to simulate. For the EoS we are looking at in this chapter, we are not including possible phase transitions throughout the profile of our neutron stars. We brought it up here as it's a quick and simple example most are familiar with.

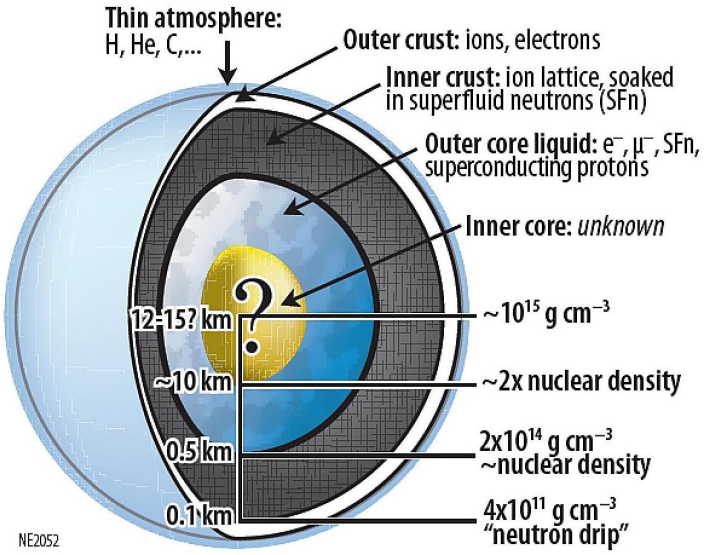

Figure 3.1: Schematic of possible neutron star composition, showing the density and radius of the different parts thought to make up a fully realistic neutron star. Note however, that the inner core composition is accurately described as 'unknown'. Figure credit: K.C. Gendreau et al. (2012), SPIE, 8443, 13

The interior particle composition of neutron stars is still uncertain, including the possible states and phase transitions of said composition. As mentioned, this is the main variable in studying neutron stars, and is the link between the structural part of chapter 2 and cooling of chapter 4. In fig. 3.1 we see a schematic of a possible neutron star interior, separated into regions of outer and inner crust, and outer and inner core – as well as a thin atmosphere. Following the initial scope for the framework laid out in section 1.2, we are for now modeling the neutron star to be of pure neutrons.[1]

3.1 Some Preliminaries

We started this chapter by mentioning thermodynamics, which as the name suggests, is a theory considering temperature, energy, and change. Temperature is in fact our macroscopic term to describe *thermal* energy in a system, which in turn is a result of microscopic random motion of particles, making temperature a measure of average *internal* kinetic energy. Combined with quantum mechanics, a statistical description of the microscopic behavior of particles, the laws of thermodynamics can be used to describe how such forms of internal energies affect macroscopic and measurable physical properties of matter. We'll come back to this in chapter 4, for now it's sufficient to understand that internal energy of matter is one of the deciding factors in an EoS. This subject is highly theoretical in the case of extremely dense distributions, as it's

[1] We'll explore the addition of protons and electrons as well.

hard to reproduce the environments needed to gather empirical evidence to support any theories put forward. As mentioned in section 2.2.1, this is where neutron stars come in handy, acting like astronomical laboratories. Note that none of the equations from chapter 2 have been directly dependent on the temperature of the star, describing the large scale properties of matter and its response to gravity. The thermodynamical state of the matter is contained within the EoS. By measuring and placing upper (and lower) limits on observable quantities of neutron stars, like their mass and radius, we can infer constraints on the EoS appropriate under such dense conditions.

In kinetic theory, thermodynamical quantities are completely described by the number density of particles in *phase space*, a kind of six-dimensional volume with three dimensions for position and three dimensions for momentum in each spatial direction. This number density is written on infinitesimal form (to the left) as

$$\frac{d\mathfrak{N}}{d^3x\, d^3p} = \frac{g}{h^3} f(\vec{\mathbf{x}}, \vec{\mathbf{p}}, t), \tag{3.1}$$

where on the right-hand side we have defined the equivalent dimensionless *distribution function* f describing the number of particles in a unit volume with average momenta $\vec{\mathbf{p}}$ and position $\vec{\mathbf{x}}$. h^3 is used for the volume element in phase space, where h is Planck's constant. What we usually think of as temperature, internal kinetic energy, is here accounted for by the momentum $\vec{\mathbf{p}}$ of particles. g is the statistical weight of the specific particle type; for massive particles $g = 2S + 1$, where S is the quantum mechanical spin. For neutrons, protons, and electrons, being fermions with half-integer spin, we have $g = 2$.

Quantities like the physical number density, energy density, and pressure are all given in general as integrals over all momenta in the phase space number density as follows

$$n = \int \frac{\mathfrak{N}}{d^3x\, d^3p}\, d^3p \tag{3.2}$$

$$\epsilon = \int E \frac{\mathfrak{N}}{d^3x\, d^3p}\, d^3p \quad \text{where} \quad E = \left(p^2c^2 + m^2c^4\right)^{1/2} \tag{3.3}$$

$$P = \frac{1}{3} \int pv \frac{\mathfrak{N}}{d^3x\, d^3p}\, d^3p \quad \text{where} \quad v = \frac{pc^2}{E}. \tag{3.4}$$

The last equation for the pressure on this form is only for an isotropic distribution of momenta,[2] and effectively states that the pressure is just a momentum flux. These equations look rather complicated, requiring us to think in terms of this six-dimensional phase space. By eq. (3.1) it's easier to work with the distribution function.

[2]Thats why the factor 1/3 comes in.

3.1.1 The Distribution Function

The distribution function is particularly useful when considering ideal gases in equilibrium, simplified gases composed of noninteracting particles. Ideal gases are first of all pedagogical, but also successfully describes many ordinary gases we encounter in everyday life. It then takes the following form, where the time, position, and momentum dependency is incorporated into the average energy E_i for particle type i

$$f_i(E_i) = \frac{1}{\exp[(E_i - \mu_i)/(k_\mathrm{B}T)] \pm 1}. \tag{3.5}$$

The combination $k_\mathrm{B}T$ is interchangeable with thermal energy, where T is the temperature of the system and k_B is Boltzmann's constant. The sign in the denominator is determined by whether the particle species that make up the gas, call it i, are fermions$(+)$ or bosons$(-)$. For our purposes, we may confine our discussion to fermions, such as ordinary neutrons, protons, and electrons.[3] Systems of fermions described by eq. (3.5) are said to obey *Fermi-Dirac statistics*. The important quantity μ_i is the chemical potential of species i, describing the change in energy for the system given a unit change in number density for species i, while keeping the volume, entropy, and number densities of other particle species constant.

As mentioned in chapter 2, it's the internal pressure that is opposing the gravitational potential in stars, preventing them from collapsing. When considering neutron stars, the pressure normally associated with classical gases is no longer enough to counteract gravity, and the constituent fermions are forced closer together in space, forming a *degenerate* Fermi gas. In degenerate matter, some counterintuitive quantum mechanical behavior must be considered. According to quantum theory, particles confined within a volume are only able to be in *discrete* quantifiable energy states, in contrast to continuous energy. Additionally, we have Pauli's exclusion principle, stating that identical fermions cannot occupy the same quantum state in phase space simultaneously. As the fermions in neutron stars are forced together into a tiny volume, their only option is to occupy higher and higher energies, i.e. momenta, in phase space. This kinetic energy induced by degeneration is the source of the increased pressure, and we may associate this additional kinetic energy to a *Fermi temperature*. In a system where the Fermi temperature is comparable to the «normal physical» temperature, classical thermal effects are comparable in strength to quantum effects. As an extension, systems where the Fermi temperature is so large that classical thermal effects are negligible in comparison, are called *completely degenerate* matter. For typical neutron star densities, the Fermi temperature takes large values about $10^{11} \sim 10^{12}\,\mathrm{K}$, considerably higher than the estimated temperature in the inner core of the sun $\sim 1.5 \times 10^7\,\mathrm{K}$. Taking eq. (3.5)

[3] We have here avoided too much unnecessary details and specific definitions encountered when entering what is often called the *particle zoo*. In the models currently included in this framework, we are only treating at most these three fermions and the neutrino lepton.

in the limit of zero temperature[4]

$$T \to 0 \quad \text{or} \quad \frac{\mu_F}{k_\mathrm{B} T} \to \infty, \tag{3.6}$$

the chemical potential at this temperature defines the Fermi energy, $\mu_F \equiv E_F$, and the mentioned Fermi temperature $T_F = E_F / k_\mathrm{B}$. The distribution function then reduces to the simple form, applicable to completely degenerate matter,

$$f_i(E_i) = \begin{cases} 1, & E_i \leq E_F \\ 0, & E_i > E_F. \end{cases} \tag{3.7}$$

As it turns out, it's easier to understand the distribution function in this special case, while it still describes the same phenomena: it quantifies the average occupation number of a given state in phase space with energy E. We now have a quantitative definition of completely degenerate matter – that is matter which is distributed according to eq. (3.7). On average, every state below the Fermi energy is occupied, while non of the states above are filled. This transition is referred to as the Fermi surface of species i, which is at a constant energy as long as the number density of the involved species don't change in time. The number of available quantum states increases exponentially with energy, and so the average particle in degenerate matter is actually relatively close to this surface. The distribution function on this form greatly simplifies the general integrals for the physical number density, pressure, and energy density in eqs. (3.2) to (3.4).

In the dense interior of neutron stars the expected Fermi temperature is very high, two or three orders of magnitude higher than the actual interior temperature. As such we can treat neutron stars as being completely degenerate, and apply the limit of zero temperature. Therefore, the common types of EoS applied to neutron stars are often called *cold* equations of state, and in extension, neutron stars are often described as cold compact objects. This statement may seem rather obscure in a paper mainly regarding the *cooling* of neutron stars, but remember there definitely is *some* physical thermal energy present. It's just that the effect this thermal energy has on the equation of state is negligible, with most of the particles in states at (or close to) the constant Fermi surface distributed according to eq. (3.7) in phase space.[5] As the Fermi energy is constant, so follows a static EoS, in line with our assumptions from chapter 2. When later studying the actual cooling process of neutron stars in chapter 4, we'll just assign an initial physical thermal temperature to the matter, and treat the interior as static. As we'll see, within reasonable physical limits, how we choose to assign this temperature doesn't really matter.

[4] We don't know of any mechanism able to cool matter to true absolute zero temperature, but by taking the limit we should be safe.

[5] At least to a good approximation. In regions closer to the surface, where gravity is the weakest, there should exists non-degenerate components.

With the Fermi energy established, we define the corresponding Fermi momentum, $p_{F,i}$, and dimensionless Fermi momentum, x_i, for particle species i through

$$E_{F,i} \equiv \sqrt{(m_i c^2)^2 + (p_{F,i} c)^2} \tag{3.8}$$

$$x_i = \frac{p_{F,i}}{m_i c}. \tag{3.9}$$

The dimensionless Fermi momentum, or «relativity parameter» as we will call it, is more convenient to work with mathematically than the dimensional Fermi energy or momentum. We'll thus use it for most of the mathematical representation in the thesis, while qualitatively referring to either the Fermi energy or momentum in the text.

In sections 3.2 and 3.3 we present the theory behind the first and simplest equations of state constructed by Chandrasekhar in his pioneering work on degenerate matter and white dwarfs (Chandrasekhar, 1939; Shapiro and Teukolsky, 1983). These equations are indeed rough approximations, and definitely incorrect in many ways. In our theoretical description of the matter we have to guess for the relevant energy sources and particle reactions taking place, as we have no experimental environment which can reach these densities here on earth. The large uncertainty in different possible phases and states the degenerate matter may occupy at different densities, combined with the wide range of densities present from the core to the surface of neutron stars, make our theoretical description an educated guess at best. As in chapter 2, we include fig. 3.2 to have some visual representation of what we're dealing with in these equations.

In the years since Chandrasekhar (1939), our understanding and numerical modeling techniques have increased significantly, alongside new and increasingly accurate observational data of neutron stars from pulsars and supernova remnant nebule. In section 3.4 we present the parameterized EoS by Gandolfi (2012), resulting from more recent and detailed many-body quantum simulations.

3.2 Ideal, Completely Degenerate Neutron Fermi Gas

The first and simplest neutron star particle composition is a spherical distribution of noninteracting, degenerate, free neutrons. Using eqs. (3.1) and (3.2) with the distribution function from eq. (3.7) the number density of the neutrons are

$$n_n = \frac{2}{h^3} \int_0^{p_{F,n}} 4\pi p^2 \, dp = \frac{8\pi}{3h^3} p_{F,n}^3, \tag{3.10}$$

with the statistical weight $g = 2$ for neutrons, and the integral now only going to p_F as that's where the distribution function is non-zero. Using the relativity parameter instead, we have

$$n_n = \frac{x_n^3}{3\pi^2 \lambda_n^3}, \tag{3.11}$$

where $\lambda_n = \hbar/(m_n c)$ is the neutron Compton wavelength [cf. table A.2]. From eq. (3.11) we see that the number density for a completely degenerate ideal fermi gas is only dependent on the relativity parameter, i.e. the «height» of the Fermi surface for the specific particle. Thus, the Fermi energy of a given distribution of such gas is determined solely by the number density, reflecting the effect of Pauli's exclusion principle briefly discussed in section 2.1. This is also true for the rest mass density ρ_0, which is simply the number density multiplied by the particle mass of neutrons

$$\rho_{0,n} = n_n m_n. \tag{3.12}$$

Similarly, the pressure is found from eq. (3.4) as

$$\begin{aligned} P_n &= \frac{1}{3}\frac{2}{h^3}\int_0^{p_{F,n}} \frac{p^2c^2}{\left(p^2c^2 + m_n^2c^4\right)^{1/2}} 4\pi p^2\, dp \\ &= \frac{8\pi m_n^4 c^5}{3h^3}\int_0^{x_n} \frac{x^4}{\left(1+x^2\right)^{1/2}}\, dx \\ &= \frac{m_n c^2}{\lambda_n^3}\Theta(x_n), \end{aligned} \tag{3.13}$$

$$\text{where} \quad \Theta(x) = \frac{1}{8\pi^2}\left[x\sqrt{1+x^2}\left(\frac{2x^2}{3} - 1\right) + \ln\left(x + \sqrt{1+x^2}\right)\right]. \tag{3.14}$$

The energy density, including rest mass energy, is given from eq. (3.3)

$$\begin{aligned} \epsilon_n &= \frac{2}{h^3}\int_0^{p_{F,n}} \left(p^2c^2 + m_n^2c^4\right) 4\pi p^2\, dp \\ &= \frac{m_n c^2}{\lambda_n^3}\chi(x_n) \end{aligned} \tag{3.15}$$

$$\text{where} \quad \chi(x) = \frac{1}{8\pi^2}\left[x\sqrt{1+x^2}\left(1+2x^2\right) - \ln\left(x + \sqrt{1+x^2}\right)\right]. \tag{3.16}$$

From eq. (3.15) the mass density is found simply as

$$\rho_n = \frac{\epsilon_n}{c^2}. \tag{3.17}$$

Equations (3.13), (3.15) and (3.17) determines the EoS for ideal, degenerate, free neutrons and is sometimes referred to as the Chandrasekhar EoS. However, we will refer to this as the Fermi n EoS.

Note that all the above equations presented for neutrons in this section are trivially scaled to ideal distributions of other particle types, by interchanging the subscript n to the appropriate particle; that is changing the particle mass m_i and statistical weight g_i.

3.2.1 The Polytropic Formula

Equations (3.14) and (3.16) reduces through Taylor expansions to a polynomial form in the non-relativistic ($x \ll 1$) and ultra-relativistic ($x \gg 1$) limit respectively

$$x \ll 1, \quad \begin{cases} \Theta(x) \to \frac{1}{15\pi^2}\left(x^5 - \frac{5}{14}x^7 + \frac{5}{24}x^9 + \ldots\right) \\ \\ \chi(x) \to \frac{1}{3\pi^2}\left(x^3 + \frac{3}{10}x^5 - \frac{3}{56}x^7 + \ldots\right) \end{cases} \tag{3.18}$$

$$\tag{3.19}$$

$$x \gg 1, \quad \begin{cases} \Theta(x) \to \frac{1}{12\pi^2}\left(x^4 - x^2 - \frac{1}{2}\ln(2x) + \ldots\right) \\ \\ \chi(x) \to \frac{1}{4\pi^2}\left(x^4 + x^2 - \frac{1}{2}\ln(2x) + \ldots\right). \end{cases} \tag{3.20}$$

Then, to first order, the equation of state can be written on *polytropic* form as a function of the *rest mass* density ρ_0

$$P(\rho_0) = \kappa\rho_0^\Gamma, \tag{3.21}$$

where κ and Γ are constants given in the two limits as

$$x \ll 1, \quad \Theta(x) \to \frac{x^5}{15\pi^2}, \quad \Gamma = \frac{5}{3}, \quad \kappa = \frac{3^{2/3}\pi^{4/3}\hbar^2}{5m_n^{8/3}} = 5.3802 \times 10^9 \,\text{cgs} \tag{3.22}$$

$$x \gg 1, \quad \Theta(x) \to \frac{x^4}{12\pi^2}, \quad \Gamma = \frac{4}{3}, \quad \kappa = \frac{3^{1/3}\pi^{2/3}\hbar c}{4m_n^{4/3}} = 1.2293 \times 10^{15} \,\text{cgs}. \tag{3.23}$$

The unit of κ is indicated just as cgs as conventional in the field, as the actual units change between the two limits. This can be seen by a simple dimensional analysis of eq. (3.21) using the two listed values for Γ. To be precise, the units of κ is $\text{cm}^4\,\text{g}^{-2/3}\,\text{s}^2$ in the non-relativistic limit, and $\text{cm}^3\,\text{g}^{-1/3}\,\text{s}^2$ in the ultra-relativistic.

The polytropic form for the EoS is easier to interpret, where the Fermi statistics is encapsulated in the rest mass' dependency on the Fermi energy,[6] and the numerical value of the constants. The equation is especially sensitive to the adiabatic index Γ, referred to as the *stiffness* of the EoS; a *stiff* EoS corresponds to a high numerical value for Γ, while a low Γ is referred to as a *soft* EoS. Keep in mind, it's the combination of the adiabatic index *and* the constant in front that determines the pressure for a given density, the stiffness only describes the slope of the curve for increasing densities. When referring to the *effective* stiffness, we mean the combined behavior fully describing the pressure. In fig. 3.2 the resulting pressure as a function of rest mass density for the Fermi gas models are compared. Here we see how the relativistic approximation overshoots the full Fermi EoS at low densities due to the large value of κ, but fits well at high densities as the slope (stiffness) of the curve is more moderate. The opposite is the case for the non-relativistic approximation.

[6] Indirectly through eq. (3.11) and the relativity parameter.

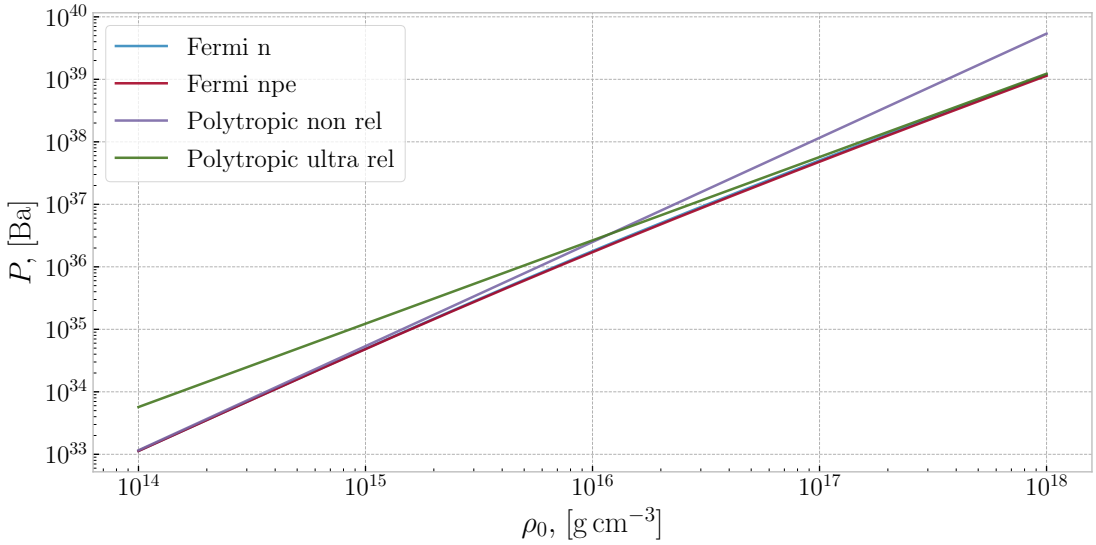

Figure 3.2: Demonstration of the polytropic and Fermi equations of state. The pressure as function of increasing rest mass density are showcased. The non-relativistic and ultra-relativistic polytropic EoS are seen to successfully approximate the Fermi EoS, in the low and high density domain respectively. Note how indistinguishable the two Fermi EoSs are in red and blue – there's seemingly little change in the pressure when including protons and electrons.

3.3 Ideal, Degenerate *n-p-e* Gas

A seemingly immediate improvement to the EoS is to assume a contribution from electrons and protons to the particle composition. While the Fermi EoS for a distribution of free neutrons is useful for establishing the theory, a distribution of pure free neutrons is unlikely to appear in nature.[7] Further, we know that free neutrons have a half-life caused by β-decay

$$n \to p + e^- + \bar{\nu}_e, \tag{3.24}$$

where n, p and e^- is the neutron, proton and electron respectively, and $\bar{\nu}_e$ is the electron antineutrino. Thus, our assumptions for a pure ball of neutrons from section 3.2 seems lacking.

However, this decay channel is blocked if the density is sufficiently high so the electron Fermi surface is above the energy of the emitted electron. If so, all energy levels the emitted electron *could* fill are already occupied. With reaction 3.24 blocked, the inverse β-decay process

$$e^- + p \to n + \nu_e \tag{3.25}$$

[7] Considering that neutron stars are the supernova remnant of massive stars with a complex particle composition and metallicity.

efficiently transforms protons and electrons into neutrons instead. Reaction 3.25 is possible in general if the initial electron acquires high enough energy to make up the difference in mass between the proton and neutron

$$Q_{n,p} = (m_n - m_p)c^2 \approx 1.29\,\mathrm{MeV}. \tag{3.26}$$

Free electrons normally don't reach such high energies , but that's no longer true in high density degenerate matter where most of the electrons approach the Fermi momentum.

3.3.1 The *n-p-e* Equilibrium Solution

To characterize the properties of such a gas of free electrons, protons and neutrons we can consider the ideal equilibrium solution. β-equilibrium is then defined by requiring equality in the constituent's chemical potential

$$\mu_e + \mu_p = \mu_n, \tag{3.27}$$

where the chemical potential of neutrinos is set to zero, as they are assumed to leave the system once created.[8] Taking the chemical potential equal to the Fermi energy and using the relativity parameter for each particle,[9] eq. (3.27) reduces to

$$m_e\sqrt{1+x_e^2} + m_p\sqrt{1+x_p^2} = m_n\sqrt{1+x_n^2}. \tag{3.28}$$

Assuming charge neutrality implies a relation between the number density of negative and positive charged particles, that is

$$n_e = n_p \tag{3.29}$$

$$\frac{x_e^3}{3\pi^2\lambda_e^3} = \frac{x_p^3}{3\pi^2\lambda_p^3} \tag{3.30}$$

$$\Rightarrow m_e x_e = m_p x_p, \tag{3.31}$$

where we have used the equations from section 3.2 scaled to electrons and protons. Thus, we have a $1-1$ relationship between the number densities of the three species, as well as for the relativity parameter.

The EoS can now be constructed for a given particle composition in terms of one of the particle's relativity parameter, assuming each particle species behaves like an ideal gas in the equilibrium solution. By specifying for example x_p, eq. (3.31) gives x_e and eq. (3.28) gives x_n. The total pressure, energy, and number density is then found as a

[8] We'll come back to this in chapter 4.
[9] Equations (3.8) and (3.9)

sum over the ideal contribution from each particle species

$$P = \frac{m_e c^2}{\lambda_e^3}\Theta(x_e) + \frac{m_p c^2}{\lambda_p^3}\Theta(x_p) + \frac{m_n c^2}{\lambda_n^3}\Theta(x_n) \tag{3.32}$$

$$\epsilon = \frac{m_e c^2}{\lambda_e^3}\chi(x_e) + \frac{m_p c^2}{\lambda_p^3}\chi(x_p) + \frac{m_n c^2}{\lambda_n^3}\chi(x_n) \tag{3.33}$$

$$n_B = n_n + n_p = \frac{x_p^3}{3\pi^2\lambda_p^3} + \frac{x_n^3}{3\pi^2\lambda_n^3}. \tag{3.34}$$

In eq. (3.34) we have defined the baryonic number density, which we will come back to in chapter 4. This is often used instead of the total number density including electrons. For example, when considering the rest mass density of the system, the electrons' contribution is negligible in a charge-neutral distribution

$$\begin{aligned}\rho_0 &= \sum_i \rho_{0,i} = \sum_i n_i m_i \quad \text{for} \quad i \in \left\{n, p, e^-\right\} \\ &= n_n m_n + n_p(m_p + m_e) \quad \text{where} \quad n_p = n_e \\ \rho_0 &\approx n_n m_n + n_p m_p. \end{aligned} \tag{3.35}$$

Note that the equations of this section are only applicable to describe equilibrium when we assume a fixed charge, baryon number, and lepton number.[10] Full treatment of gravitational collapse with escaping neutrinos is not a closed system, and thermodynamic equilibrium cannot be achieved. In a more detailed treatment the *n*-*p*-*e* composition should be determined by solving the reaction rate equations. In line with the naming for the pure neutron gas, we adopt the label Fermi npe EoS for this model.

3.4 Interacting Quantum Many-Body Neutron Gas

To obtain a refined EoS we have to abandon the ideal gas approximation and allow for continued interactions between the particles. Our presentation of the equations here is brief by necessity, as the complete description requires the full apparatus of many-body quantum theory. Among particle and nuclear physicist the importance of the two- and three-body nuclear forces in dense systems are well known, and Gandolfi (2012) employed the auxiliary field diffusion Monte Carlo method (Schmidt and Fantoni, 1999) to model these reactions in a pure neutron gas. They considered a nuclear Hamiltonian containing the kinetic energy, the neutron-neutron (2n) interaction, and the three-neutron (3n) interaction potentials.

[10] The lepton number is chosen to be zero here, $n_\nu = 0\,(\mu_\nu = 0)$.

Table 3.1: Numerical values of fitting coefficients for the QMC EoS from Gandolfi (2012) defined in eq. (3.36). The table includes varying models for the 3n potential and symmetry energies, which we have given label names to distinguish. Note specifically the rather large variance in the value for b.

3n Potential†	Label Name*	a [MeV]	α	b [MeV]	β
none	QMCnone	12.7	0.49	1.78	2.26
$V_{2\pi}^{PW} + V_{\mu=150}^{R}$	QMC1	12.7	0.48	3.45	2.12
$V_{2\pi}^{PW} + V_{\mu=300}^{R}$	QMC2	12.8	0.488	3.19	2.20
$V_{3\pi} + V_R$	QMC3	13.0	0.49	3.21	2.47
$V_{2\pi}^{PW} + V_{\mu=150}^{R}$	QMC4	12.6	0.475	5.16	2.12
$V_{3\pi} + V_R$	QMC5	13.0	0.5	4.71	2.49
UIX	QMCUIX	13.4	0.514	5.62	2.436

† These are the names used to describe the fitting coefficients for various 3n potential models as they are listed in Gandolfi (2012). We include them here to ease the comparison to their article, but will only refer to the label names* we have given them.

Gandolfi (2012) presents the resulting parameterized EoS from the quantum Monte Carlo (QMC) simulations in terms of energy per particle as a function of number density

$$E(n) = a\left(\frac{n}{n_0}\right)^{\alpha} + b\left(\frac{n}{n_0}\right)^{\beta}, \tag{3.36}$$

where $n_0 = 1.6 \times 10^{38}\,\mathrm{cm}^{-3} = 0.16\,\mathrm{fm}^{-3}$ is the nuclear saturation density. By construction, the coefficients a and α are dominating in the low-density regime, while b and β are sensitive to the high-density behavior, listed for seven different 3n models in table 3.1. We have given these models some simple label names as we don't go into details regarding the 3n interactions. Comparing this representation to the polytropic formula from section 3.2.1 we see how the QMC EoS more accurately can describe a wider range of density values without abandoning the underlining assumptions, by changing the effective stiffness above and below n_0. The numerical values of most of the coefficients vary slightly dependent on the model for 3n interaction potential, except for b, which is consistent with the known uncertainty in the high-density regime.

Of all the available QMC models, we've chosen to show results for four of them in this thesis, picked to emphasize their differences. In both ends of the extreme we have the QMC none model with no 3n interaction energies, and the QMC UIX model with a substantial contribution from the 3n interaction at high densities. The models we have given number labels, increase in effective stiffness above saturation density with increasing label number, which entail increased energy associated with the 3n interaction. The most interesting of these intermediate stiff models are the QMC 3 and 4, which we'll look at in addition to the none and UIX models in fig. 7.3 and chapter 10.

Chapter 4

Cooling of Neutron Stars

Here on earth, everyone knows that if you leave your coffee for too long it turns cold. But why does it go cold, and more importantly, how? This turns out to be a complicated question to answer, and physicists have spent years developing the theory of thermodynamics . The initial state of the coffee, and the cup itself, at the point in time when you leave it be, determine the outcome of how the collective coffee-cup system cools over time. This is described by a swell of factors and dependencies, determined by the complexity of the system in question and the relevant heat transport mechanisms available. The initial temperature of the coffee and the cup is of course always relevant, and is described as a result of the collective thermal energy of the particles that make up the system. But also the ratio of water to coffee grains, and maybe sugar or milk, the thickness, and material of the cup, all relevant in determining the exact density, mass, particle composition, and thermal conductivity of the system. The coffee will cool faster if you use a spoon to stir it with, accelerating the cooling process by inducing convection, even more so if the spoon is cold! If you place the cup outside in the wind, it will cool faster than inside, again caused by convection and conduction with the surrounding relatively endless in size heat sink of the cool atmosphere. The list goes on and on, all of this is what we try to describe and quantify in thermodynamics. As an additional cooling effect, Max Planck discovered that all objects in the universe shine, or radiate, dependent on the object's temperature. This radiation may come from many different types of sources, and on all the wavelengths of the electromagnetic spectrum, and must be described as a quantum theory. The thermal radiation, usually in the infrared here on earth, also contributes to the cooling process of the coffee-cup system, albeit a relatively small part at everyday temperatures.

The same may be said for planets, moons, huge clouds of intergalactic gas, even black holes, and finally the stars themselves! Left out in the Universe for too long they will eventually cool down. But with the grim empty space as their surrounding environment, the only available heat transport mechanism to remove energy from their

system is through radiation out into the Universe.[1] Much of the complexity behind the coffee's cooling process is determining the interactions with its environment. For neutron stars in hydrostatic equilibrium, that interaction is relatively simple. Just determine how much energy that leaves the star per unit time through radiation, called the star's luminosity, and how the temperature of the matter in the star change based on the radiated thermal energy. This is dependent on the types of matter present in the star. The matter, or coffee, in the above example, is mostly water with the added flavor of coffee grains – analogous to fermions, specifically neutrons, in our neutron stars. In this picture, including protons and electrons is kind of like adding milk and sugar. The protons (liquid with milk flavor) being very similar to neutrons (liquid with coffee flavor), but making up less of the total amount of matter, and the electrons (sugar) dissolving freely into the mixture. Quantitatively describing the luminosity and temperature change may be demanding, dependent on the model used to describe the system. Following our structure of gradually building complexity, we lay out the ground rules for homogeneous and isothermal objects in section 4.1. Then we look at some relevant sources for cooling and heating in section 4.2, before introducing the adjustments needed to model the more realistic inhomogeneous and isotropic objects in section 4.3. Finally we'll add the modifications from general relativity in section 4.3.1.

4.1 The Cooling Equation

When we usually think of stars, we don't think of objects that start out hot and gradually cool down, but flaming oceans of plasma and energy. However, just like all other objects, stars continuously cool through all the energy they release into the Universe by radiation. But most of them also continuously fuse particles in energy-efficient fusion driven by the crushing force of gravity in their cores. These particle reactions produce all the star's energy and radiation in the first place, and as discussed in chapter 2, it's the pressure of the matter and radiation from the cores that keeps the stars in hydrostatic equilibrium. This means that even though the star is constantly «cooling» by thermal radiation, it's equally heated by the fusion reactions, and only excess heat above the equilibrium energy is released. The result is a net zero change in the star's temperature.

We can quantify radiative cooling of a homogeneous, isothermal volume in an ordinary differential equation

$$\begin{aligned} \frac{dU}{dt} &= C_v \frac{dT}{dt} = -(Q_c - Q_h) \\ \text{or} \quad \frac{dT}{dt} &= -\frac{Q_c - Q_h}{C_v}, \end{aligned} \tag{4.1}$$

[1] This is somewhat simplified to fit with the cooling mechanisms we are looking at here. Radiation like we are including indeed accounts for the dominating and most common cooling process found in most stars.

where U is the total thermal energy, t is the time coordinate, T is the temperature, C_v is the total heat capacity[2] and Q_c and Q_h are the cooling and heating rate respectively. For our purposes we will use the equation on the latter form, as we are not as interested in the total thermal energy. As mentioned, for «normal» stars living in hydrostatic and thermal equilibrium on the main sequence,[3] the sum of thermal energy lost and gained is zero, resulting in a constant temperature

$$\begin{aligned} Q_c - Q_h &= 0 \\ \Rightarrow \frac{dT}{dt} &= 0. \end{aligned} \tag{4.2}$$

For neutron stars, this balance is no longer maintained. As the equilibrium pressure preventing the star from collapsing is almost exclusively from degenerate fermions, not from fusion reactions, there's little contribution to the heating rate. Through particle reactions, which we dive into in section 4.2, the cooling rate of the star remains relatively high, at least compared to the heating rate which is significantly lower, or even zero. The result is a negative temperature time derivative, cooling the neutron star over time

$$\begin{aligned} Q_c - Q_h &> 0 \\ \Rightarrow \frac{dT}{dt} &\propto -(Q_c - Q_h) < 0. \end{aligned}$$

The cooling rate describes energy loss per unit time through radiation. This is just the sum of the different luminosities generated by the star through the mentioned reaction rates. Excluding heating completely for now, we write the cooling rate simply as

$$Q_c = \sum_i L_i \quad \text{for} \quad i \in \{\nu, \gamma, \ldots\} \tag{4.3}$$

where L_i is the total luminosity generated from each reaction or source i. We can then write the cooling equation as

$$\frac{dT}{dt} = -\frac{\sum_i L_i}{C_v}, \tag{4.4}$$

describing the change in temperature during an infinitesimal time interval, in terms of the two governing factors for radiational heat transfer:

The heat capacity: the energy required to change the temperature of matter. C_v encapsulates the relevant micro-physics behind the amount of heat, i.e. energy, that is required to change the temperature of matter with total mass M in a constant volume V by one kelvin, $\Delta T = 1\,\mathrm{K}$. For the temperature to increase, C_v amounts of energy need to enter V from outside, and for the temperature to *decrease*, C_v amounts of energy

[2]Note, not the *specific* heat capacity

[3]Main sequence stars are a group of «alive» stars, defined to the main sequence by the fact that they still produce energy in their core through fusion of hydrogen.

need to leave V. It's as simple as that. Including the dominant Fermi energy as the only relevant factor for degenerate non-interacting fermions in a homogeneous soup of N particles with mass m_i in a constant volume V, the total heat capacity as given by Chandrasekhar (1939) is

$$C_v = \left.\frac{dU}{dT}\right|_{N,V} = \frac{\pi^2\sqrt{x_i^2+1}}{x_i^2} N k_{\mathrm{B}} \frac{k_{\mathrm{B}}T}{m_i c^2} \tag{4.5}$$

where $x_i = p_F/mc$ is the relativity parameter from eq. (3.9), which in this context can be thought of as the dimensionless number density of species i – in phase space to be precise.

The total luminosity: the sum of energy radiated away per unit time. This is a sum over multiple reaction sources, and how we calculate the involved factors is highly dependent on the complexity and detail desired, and the model used to describe the environment. To quantify this we need insight into some of the particle reactions taking place in an extreme environment such as the interior of neutron stars, how we model these reactions, and the resulting emissivities, ϵ_i. Emissivity measures radiated energy per unit time per unit volume, which we need to calculate the total luminosity of a volume. The main goal of section 4.2 is to quantify these emissivities for different reactions i. In the homogeneous and isothermal case, obtaining the total luminosity resulting from reaction i is only a case of integrating a constant emissivity over the volume of the system. The more realistic non-isothermal case is revisited in section 4.3.

4.2 Particle Reactions and Emissivity

As mentioned in chapter 3, the composition and state of neutron star interiors are still uncertain. By combining observations of the mass and radius of neutron stars with the time evolution of their effective surface temperature, we can infer constraints on the mystery regarding their interior. Some of the most relevant reactions and cooling mechanisms are the subject of this section.

Calculating the energy loss rate from nuclear interactions is a complicated field, deserving of a couple of master theses on its own. The main factors involved are first the rate of the reactions, how many of the relevant reactions that take place during a unit time. The second factor is the actual energy released from each reaction, usually easier to approximate than the rate, but highly dependent on the actual reaction in question and how you model the nuclear forces and potentials. The reaction rate is a numerical beast, dependent on the density and energy of the system, as well as the reaction probability amplitude. Actually computing the elements of these matrices involves solving complicated many-body Schrödinger equations including weak and strong

nuclear interaction Hamiltonians. For our purpose we are mostly interested in how the different reactions affect the cooling process, and trust in the work done by others. In the following sections we will briefly discuss some of the reactions studied in connection with neutron stars over the last century, with emphasis on the *modified* Urca process.

4.2.1 The Modified Urca Rate

We are interested in the long term period of neutrino cooling of the neutron star from a temperature of a few 10^9 K. This is after the star has settled into hydrostatic equilibrium and the initial cooling from around $T \gtrsim 10^{11}$ K at the formation of the proto-neutron star is completed. Below 10^9 K it can be shown that the mean free path of an electron neutrino is much larger than the assumed radii of common neutron stars, and thus the star is transparent to neutrinos (Shapiro and Teukolsky, 1983). That is, once the neutrinos are created, whatever the reaction, they can freely escape through and out of the neutron star without interacting and transporting energy to other regions of the star.

Most stars emit some amount of neutrinos. About 100 billion neutrinos originating from the sun travel straight through your thumbnail every second.[4] The types and amounts of neutrinos created are heavily dependent on the temperature of the environment where the reactions take place. In the very high core temperatures of massive stars, $T \gtrsim 10^{10}$ K, or during a supernova core collapse, the most dominating reaction is the normal and inverse β-decay channels [cf. section 3.3]. These are called the Urca reactions,

$$n \to p + e^- + \bar{\nu}_e, \quad p + e^- \to n + \nu_e, \tag{4.6}$$

where ν_e, n, p and e^- are the electron-neutrino, neutron, proton and electron respectively. These reactions are a perfect sink for the large amount of energy in the star, and are the main mode for energy loss through neutrinos. They're so efficient the name Urca is actually in part inspired by the Urca casino in Rio de Janeiro;

> ... the Urca process results in a rapid disappearance of thermal energy from the interior of a star, similar to the rapid disappearance of money from the pockets of the gamblers on the Casino de Urca. (Gamow (1970))

However, for degenerate matter this process is heavily suppressed, such as in a neutron star that has cooled to $\sim 10^9$ K. This can be demonstrated through conservation of energy and momentum, which we describe for a system of ideal degenerate gas with free electrons, protons, and neutrons in a similar fashion to section 3.3. Degenerate interior matter in equilibrium must satisfy the β-equilibrium condition

$$\mu_n = \mu_p + \mu_e, \tag{4.7}$$

[4] According to Fermi National Accelerator Laboratory, neutrinos.fnal.gov/sources/solar-neutrinos/ last checked 15.01.2021.

where μ_i is the chemical potential of the neutrons, protons, and electrons in the system.[5] As mentioned, for the temperature range we are looking at the neutrinos are assumed to leave the system once created, as the neutron star is transparent to neutrinos, so their number density and hence chemical potential within the system are set to zero.[6] The energy associated with the reaction is thought to leave the system with the neutrino, contributing to the cooling rate. The chemical potentials are to a good approximation just the Fermi energies, which at nuclear densities such as in a neutron star is

$$\begin{aligned} E_{F,i} &\simeq m_i c^2 + \frac{p_{F,i}^2}{2m_i} \quad \text{for} \quad i \in \{n, p\} \\ E_{F,e} &\simeq p_{F,e} c. \end{aligned}$$

We also require charge neutrality in the system, which through eqs. (3.8) and (3.11) can be written using the Fermi momentum as

$$p_{F,e} = p_{F,p}, \tag{4.8}$$

requiring equal number density of electrons and protons. Inserting this into eq. (4.7) we have

$$E_{F,n} = E_{F,p} + E_{F,e} \tag{4.9}$$

$$\Rightarrow \frac{p_{F,n}^2}{2m_n} \simeq p_{F,e} c \left(1 + \frac{p_{F,p}}{2m_p c}\right) - Q_{n,p}, \tag{4.10}$$

where $Q_{p,n}$ is the rest mass difference of protons and neutrons from eq. (3.26), and is comparably small to the other term in eq. (4.10). Using eqs. (3.9) and (4.8), and that the proton mass dwarfs that of the electron $m_e/m_p \sim 5.4 \times 10^{-4}$, we can write the first term as

$$p_{F,e} c \left(1 + \frac{p_{F,p}}{2m_p c}\right) \simeq p_{F,e} c \left(1 + \frac{m_e x_e}{2m_p}\right) \simeq p_{F,e} c = E_{F,e}.$$

And so the Fermi energy of the neutron (minus rest mass) turns out to be more or less equal to that of the electron

$$E'_{F,n} \equiv \frac{p_{F,n}^2}{2m_n} \simeq p_{F,e} c = E_{F,e}. \tag{4.11}$$

Now, for energy and momentum to be conserved we see that the neutron's Fermi momentum must be much larger than that of the electron, again due to the large value of

[5] Here we address the normal neutron decay reaction. The proceeding is similar for the reverse reaction case.

[6] No μ_ν term in the equilibrium condition.

the neutron mass and the speed of light. Also, the proton's Fermi energy must be much smaller than the neutron's for both eqs. (4.9) and (4.11) to be satisfied, so we have

$$p_{F,e} = p_{F,p} \ll p_{F,n} \tag{4.12}$$

$$E'_{F,p} \ll E'_{F,n} \approx E'_{F,e}. \tag{4.13}$$

For the degenerate matter we are interested in, only neutrons with energy relatively close to the Fermi surface are capable of decaying, say within one $\sim k_{\mathrm{B}}T$. By energy conservation, the final proton and electron must also be within $\sim k_{\mathrm{B}}T$ of their Fermi surfaces, and likewise the energy of the escaping neutrino $\sim k_{\mathrm{B}}T$ (Shapiro and Teukolsky, 1983). Equation (4.12) requires the momenta of the emerging proton and electron to be small relative to the neutron momentum, but this is impossible! The proton can't simultaneously have small momenta and small energy compared to the neutron, while also conserving energy and momentum.

For the reaction to be possible, there needs to be something nearby to absorb and conserve the momentum in the reaction. With the large soup of free neutrons in the degenerate matter of neutron stars, a bystander neutron is likely to be available for the reactions

$$n + n \to p + e^- + \bar{\nu}_e \tag{4.14}$$

$$n + p + e^- \to n + n + \nu_e. \tag{4.15}$$

These are called the «modified» Urca reactions, suggested by Chiu and Salpeter (1964) to be important for neutron star cooling. During the period dominated by neutrino cooling, this reaction is the primary source for the electron neutrinos, and the main focus for this thesis.The process also comes in muon- and tau-neutrino emitting form, each requiring higher densities. As the rest mass of electrons is the smallest of the three leptons, it's the preferable process initially. The electron Fermi surface/energy is then gradually increased as electrons are produced and their number density increase. Eventually, the electron chemical potential, which is equal the Fermi energy, exceeds the rest mass energy of muons. Then it suddenly starts being energy efficient to produce muons and muon-neutrinos instead of electrons. Newly created electrons can only occupy high states in phase space above the current Fermi energy, while the as until now absent muons can start to fill in the lowest energy states and only the rest mass is needed to create the particles. The criteria for a reaction channel to open can be expressed as

$$\mu_e \simeq E_{F,e} > m_i c^2 \quad \text{for} \quad i \in \{\mu, \tau\}.$$

The density is not normally high enough in neutron stars to achieve these energies for the tau neutrino[7] while the muon-neutrino reactions opens at a more relevant density, around $\rho \gtrsim 2.9\rho_{\mathrm{nuc}}$, where ρ_{nuc} is the typical nuclear density $\rho_{\mathrm{nuc}} = 2.8 \times 10^{14}\,\mathrm{g\,cm^{-3}}$, also listed in table A.2.

[7] With $m_\tau c^2 = 1776\,\mathrm{MeV} >> \mu_e$.

As the modified Urca reactions involve an additional particle, the computation of the reaction rate involves a few more terms. But the main takeaway is that the modified Urca rate is slower than the normal. This is again due to the properties of the dense degenerate gas, where the low-energy states in phase space on average are occupied. Therefore, when computing the rate of these reactions, a so-called blocking factor is included to reflect the restrictions caused by the reduced number of possible final states for each particle species after the reaction. As the distribution function, f_i, [cf. eq. (3.5)] describes the average occupation number of a given state for particles species i, $(1 - f_i)$ is used as the mentioned blocking factor to represent the mean number of unoccupied states.

To arrive at a meaningful neutrino emissivity we follow the original approach of Bahcall and Wolf (1965), as outlined by Shapiro and Teukolsky (1983), describing the reaction in eq. (4.14) for the electron antineutrino emissivity as

$$\epsilon_{\bar{\nu}_e} = \left(6.1 \times 10^{19}\,\mathrm{erg\,cm^{-3}\,s^{-1}}\right)\left(\frac{\rho}{\rho_{\mathrm{nuc}}}\right)^{2/3} T_9^8, \tag{4.16}$$

where T_9 is the temperature in units of $10^9\,\mathrm{K}$ and $\rho_{\mathrm{nuc}} = 2.8 \times 10^{14}\,\mathrm{g\,cm^{-3}}$ is the mentioned typical nuclear density.

Then, by time-reversal invariance, the *normal* electron neutrino emissivity is equal to the antineutrino emissivity, so for the total electron neutrino emissivity we need to add a factor 2 to eq. (4.16).

We also need to account for possible muon-neutrinos. Effectively, the muon reactions are identical to the electron-neutrino reaction, and only differ in the phase space factor of the Hamiltonian as the electron and muon are of different masses. The contribution from muon-neutrinos to the total neutrino emissivity can be included by adding a factor $(1 + F)$ to eq. (4.16), where

$$F = \begin{cases} 0, & \rho \lesssim 2.9\rho_{\mathrm{nuc}} \\ \sqrt{1 - \left(\frac{m_\mu c^2}{E_{F,e}}\right)}, & \rho \gtrsim 2.9\rho_{\mathrm{nuc}} \end{cases} \tag{4.17}$$

is the ratio of muon- to electron-neutrino energy loss rate. Finally the full neutrino emissivity from the modified Urca process is found as[8]

$$\epsilon_\nu^{\mathrm{Urca}} = \left(7.4 \times 10^{20}\,\mathrm{erg\,cm^{-3}\,s^{-1}}\right)\left(\frac{\rho}{\rho_{\mathrm{nuc}}}\right)^{2/3} T_9^8(1 + F). \tag{4.18}$$

The total luminosity of a homogeneous body is then found by integrating the uniform density over the whole volume

$$L_\nu^{\mathrm{Urca}} = \left(5.3 \times 10^{39}\,\mathrm{erg\,s^{-1}}\right)\frac{M}{M_\odot}\left(\frac{\rho_{\mathrm{nuc}}}{\rho}\right)^{1/3} T_9^8(1 + F) \tag{4.19}$$

[8]The numerical value differs slightly from the original by Bahcall and Wolf (1965) due to an updated value used for the nuclear density ρ_{nuc} and the β-decay coupling constants.

for a neutron star of total mass M.

4.2.2 Blackbody Photon Emission

Neutron stars don't shine as bright as normal stars in the electromagnetic spectrum. Photons are mainly created through excitation and de-excitation of bound electrons, but this effect is also highly suppressed in degenerate matter. As all adjacent quantum states are occupied for electrons below the Fermi surface this process is prohibited and no photons are produced. Closer to the surface where the density drops to zero this is no longer the case, and one should expect photons to be produced. Simulating this effect computationally costly, so instead we model all photon emission through the neutron star's total blackbody radiation.

As mentioned, effectively all objects emit blackbody radiation determined solely by its temperature following Planck's law of blackbody radiation. Integrating the spectral radiance over all frequencies and multiplying with the surface area of the star, the total blackbody emission from the surface is defined as

$$L_\gamma = 4\pi R^2 \sigma_{\mathrm{SB}} T_s^4 \tag{4.20}$$

where σ_{SB} is the Stefan-Boltzmann constant and R is the radius of the star. T_s is the effective surface temperature, usually found through an envelope model of the thin atmosphere of neutron stars. While the atmosphere is computationally expensive to simulate alongside the rest of the profile, involving a gradual transition from degenerate to non-degenerate matter, its effect on the resulting structure is minimal in most cases. The thickness being of order 100 m or less, with low density compared to the interior, the change in radius and total mass when including the atmosphere is negligible (Page et al., 2004). Thus, the actual atmosphere is currently not included in the structural part of our model, further justified in section 6.1. Instead, we'll use a general so-called T_b-T_s relationship, found by other detailed envelope model calculations.

An envelope model provides a relationship between the boundary temperature of the star at the bottom of the atmosphere denoted T_b,[9] to the effective surface temperature – so that the luminosity of the envelope is equal the total surface luminosity of the star from eq. (4.20). We denote this effective surface temperature as T_s. We include an example of a simple envelope model as indicated by Tsuruta (1974, 1979)

$$\frac{T_s}{T_b} \sim 10^{-2}\alpha \quad \text{for} \quad 0.1 \lesssim \alpha \lesssim 1, \tag{4.21}$$

roughly suggesting $T_s \propto 10^{-2} T_b$, with all structural model alterations incorporated into the numerical constant α. For a more refined model we adopt the approximation

[9] That is where our structural computation ends.

presented in Kouvaris (2008); Page et al. (2004), and references therein

$$T_s = 0.87 \times 10^6\,\mathrm{K}\Big(\frac{g_s}{10^{14}\,\mathrm{cm\,s^{-2}}}\Big)^{1/4}\left(\frac{T_b}{10^8\,\mathrm{K}}\right)^{0.55}, \tag{4.22}$$

where $g_s = GM/R^2$ is the surface gravity of the neutron star. From this model we therefore have a rough $T_s \sim T_b^{0.55}$ relationship.[10]

We can write eq. (4.20) on a similar form to a conventional form to eq. (4.19) to point out an important comparison. By scaling the radius to units of 10 km, and temperature to units of 10^9 K, we write

$$L_\gamma = \big(7.13 \times 10^{44}\,\mathrm{erg\,s^{-1}}\big)\left(\frac{R}{10\,\mathrm{km}}\right)^2\left(\frac{T_s}{10^9\,\mathrm{K}}\right)^4. \tag{4.23}$$

Assuming for clarity a homogenous neutron star, due to the heavy temperature dependency of the modified Urca process, being proportional to T_9^8, we expect at early times when the temperature is high the neutrino emission to dominate the cooling process. After the temperature has been driven down sufficiently the contribution from neutrinos will be dampened, and photon emission will start dominating the cooling.

4.2.3 An Exciting Possible Heating Mechanism – Dark Matter

There are a lot of internal heating mechanism suggested to be operating in neutron stars, e.g. (Gonzalez and Reisenegger, 2010): decay of magnetic fields; cracking of the star surface, so-called *star quakes*; friction from internal velocity fields, and superfluid vortex creep; non-equilibrium reactions; and finally, what we are currently interested in, dark matter accretion.[11] As we touched upon in the introductory chapter, we don't know exactly what dark matter is. We call it matter because of the main observable feature attributed to dark matter, the fact that it has a nonzero mass and seems to interact mainly through gravity. With all the various observation techniques developed over the last century we are able to «*see*» the entire matter content of the Universe directly,[12] by analyzing the light received in our telescopes. However, this is not the case for dark matter. As the name suggests, it's dark, meaning it doesn't interact with the electromagnetic force, and is therefore invisible – that is to direct observations. We can still «see» the presence of dark matter indirectly, by e.g. observing the gravitational effect it has on the environment and the luminous matter we actually can see around it.[13] This is in fact how we know something like dark matter *must* exist. Without it,

[10] We'll use this rough approximation when we find analytical solutions in section 8.2.1. The full eq. (4.22) is used in to code.

[11] However, as discussed, our framework is implemented in such a way to facilitate future expansions to include more of these mechanisms in a straight forward way.

[12] Of course somewhat restrained by the distance to the source.

[13] Luminous matter is often used to describe the normal matter we are used to in everyday life, in contrast to dark. Another conventional name is baryonic matter.

the Universe we observe would not have had time to form any structures yet – there would simply not be enough matter in the Universe for gravitational attraction to keep anything together. In other words, there would be no galaxy clusters, or individual galaxies for that matter. Hence no stars or planetary systems . . . no you and me.

In line with what we know regarding ordinary baryonic matter and particle physics, one way to describe dark matter is as a type of exotic particle. We've come impressively far in the endeavor of constraining some of the physical properties and attributes such particles must possess, considering no one has ever seen a dark matter particle. This might be discouraging, or even make you think that cosmologists are just trying to hide some fundamental error in our theories. However, it's important to note that no one has ever actually seen e.g. an electron or proton directly either, but we've developed tools in order for us to detect them in experiments. Over the years since the discovery of the electron by Thompson (1897), we've improved and used these detection techniques to develop the field of particle physics we know today. Most people tend to accept that these minuscule particles collectively make up all the matter we see around us in the world. When considering dark matter, or dark matter particle candidates, we may draw an analogy to the time preceding Thompson (1897), we don't know how to detect them yet – that doesn't mean dark matter isn't something real, we just don't fully understand it.[14] Many exotic particle *candidates* have been proposed, of which WIMPs (Weakly Interacting Massive Particles) are one of the most popular and promising (Jungman et al., 1996). There is no *one* complete definition of WIMPS, but as the name suggests, they are thought to be particles of very large rest mass interacting as usual through gravity, but also have an interaction with the weak nuclear force, which opens opportunities for possible detections. The nuclear forces are limited to act on very short length scales, and as such WIMP-WIMP interactions are thought to have a tiny cross-section describing the probability of scattering and annihilation which explains why such detections are so difficult to observe – but importantly not impossible.

Among the swell of independent observations strongly indicating the presence of dark matter, we list some of the common examples: the rotational velocity profiles of galaxies (Borriello and Salucci, 2001); gravitational lensing, light trajectories follow geodesics in curved spacetime around strong gravitational fields (van Uitert et al., 2012); the power spectrum of the cosmic microwave background, describing the statistical distribution of the size of fluctuations in the very early Universe (Planck Collaboration, 2016); large scale N-body simulations of dark matter formation and evolution on cosmological scales (Boylan-Kolchin et al., 2009); the velocity dispersion in galaxy clusters, the original discovery that indicated an additional (large) mass requirement to explain the observed velocity of individual galaxies in gravitational bound clusters (Zwicky, 1933).

[14] Some try to explain these observed effects by modified gravitational theories. As mentioned in section 2.1.1, none of these are currently as successful as general relativity to describe the whole Universe on large scales.

From all of these independent clues, and many more observations and simulations, cosmologists try to narrow down the large pool of possible physical properties of dark matter. One of the main motivations for this thesis is to provide an additional possible signature of WIMP particles, as they should contribute to the heating rate of neutron stars, by accreting into their strong potential wells and annihilating by colliding with each other. Our description here is largely based on Kouvaris (2008), although we apply their results in a considerably more complex cooling model, within our flexible and expandable framework for neutron star modeling. The relevant signature may be evident in the cooling process of cold neutron stars at late times, as we'll discuss below. From simulations of structure formation with dark matter, one finds that all the luminous matter we can see in galaxies are dwarfed by a much more massive dark matter *halo*, an approximately spherical distribution, extending far beyond the radius of the luminous part of the galaxy. The density of this halo may be described by a relatively simple profile, decreasing with radial distance from the center of the galaxy Navarro et al. (1996). Following calculations for the accretion and annihilation rate by Kouvaris (2008), we may describe the effect of the annihilation of WIMP particles on the heating of neutron stars with a single parameter. This provides a simple way to eventually compare our results with observations in the future, by crosschecking the temperature of a given observed cold neutron star with the estimated local dark matter density at its radial distance to the center of the galaxy.

We'll model the heating rate, or «heating emissivity» ϵ_h,[15] associated with the annihilation of WIMP particles as

$$\epsilon_{\text{WIMP}} = \mathcal{A}_{\text{WIMP}} \cdot 1.16 \times 10^4 \,\text{erg}\,\text{cm}^{-3}\,\text{s}^{-1}, \tag{4.24}$$

where $\mathcal{A}_{\text{WIMP}}$ is the mentioned parameterization constant that describes the density of the dark matter halo in a given local region, expressed in units of $0.3\,\text{GeV}\,\text{cm}^{-3}$, which is the estimated dark matter density around the earth. So an $\mathcal{A}_{\text{WIMP}} = 10$ would describe a region where the density of WIMPs are 10 times higher than here on earth, $\mathcal{A}_{\text{WIMP}} = 100$ would be 100 times higher, and so on. Integrating this constant emissivity over a spherical volume, and scale the radius as before, we find

$$L_{\text{WIMP}} = \left(1.46 \times 10^{22}\,\text{erg}\,\text{s}^{-1}\right)\mathcal{A}_{\text{WIMP}}\left(\frac{R}{10\,\text{km}}\right)^3. \tag{4.25}$$

Notice that there is no temperature dependency in this heating rate, in contrast to the four powers of (surface) temperature in eq. (4.20) and eight(!) in eq. (4.18). However, the amplitude of the contribution is considerably lower. Neglecting the tem-

[15] Emissivity is most commonly used to describe emitted energy, but we'll use the term here attributed to the heating rate – which neatly fits in the cooling equation for inhomogeneous objects.

perature dependencies for now, we have

$$\begin{aligned} L_\nu^{\text{Urca}} &\sim \left(5.3 \times 10^{39}\,\text{erg}\,\text{s}^{-1}\right) \\ L_\gamma &\sim \left(7.13 \times 10^{44}\,\text{erg}\,\text{s}^{-1}\right) \\ L_{\text{WIMP}} &\sim \mathcal{A}_{\text{WIMP}}\left(1.46 \times 10^{22}\,\text{erg}\,\text{s}^{-1}\right) \end{aligned}$$

for a star of the same radius R. Thus, the heating should be negligible early on. But the star is continuously cooling over time, and so the cooling process associated with photons and neutrinos become less and less efficient as the temperature drops. After a sufficiently long time, the heating should eventually dominate the process – and as this heating is constant, the neutron star should settle in a final minimum temperature. As we'll see in part III, we find that this time is achieved within timescales of $t \sim 10^7$ years, slightly dependent on the EoS. As such we expect to find old and cold neutron stars that might have reached this minimum temperature out there in the Universe.

4.3 Inhomogeneous Objects

A complication when dealing with more realistic systems is distribution inhomogeneity in the volume. As we have seen in chapter 2, for our spherical symmetric non-rotating star model we have a one-dimensional structural profile from the core through the interior and to the surface. Prior to core collapse of the original star, we also know the energy production was mainly in the core, and that the energy is gradually transported outwards by various heat transport mechanisms. This suggests that there also should be an initial temperature profile and gradient from the hot core to the cooler surface. These effects are not reflected in eq. (4.4), which treats the cooling of a whole homogeneous and isothermal body. The isotropic interior density and temperature profile, and how they evolve, has to be considered. The equations presented in the following regarding inhomogeneous cooling and energy balance in general relativity, or profiled cooling as we'll call it, are combined from Page et al. (2006, 2004); Thorne (1977).

As discussed in chapter 2, the structural equations don't vary with the temperature, so we can treat the interior structure as static. But the reaction emissivities depend heavily on both the density and temperature, as well does the heat capacity. In total we have $6 + 2N$ variable profiles: three fixed time-independent profiles for density, mass, and gravitational potential; one time-dependent temperature profile; and lastly $2 + 2N$ auxiliary profiles for the heat capacity and thermal conductivity, λ_{th} [cf. eq. (4.34)], emissivity and luminosity (N is the number of included reactions), all $2+2N$ as functions of the fundamental variables expressed through t and r.

$$\begin{array}{ccc} T = T(t,r) & & \epsilon_i = \epsilon_i(t,r), \qquad i = 1,\, 2, \ldots,\, N \\ \rho = \rho(r) & & L_i = L_i(t,r), \qquad i = 1,\, 2, \ldots,\, N \\ m = m(r) & \Rightarrow & C_v = C_v(t,r) \\ \phi = \phi(r) & & \lambda_{th} = \lambda_{th}(t,r) \end{array}$$

We can think of the one-dimensional profile as dividing the star into a lot of infinitesimal intervals of thickness dr, where each interval is homogeneous in density and temperature. In three dimensions, each dr makes up the thickness of uniform spherical shells at varying radii from the core to the surface. We can now treat the cooling of each individual shell similar to that of the uniform simpler case, but we also have to include energy transport between the shells. Whenever there is a temperature gradient, there is energy transport through heat conduction[16] following Fourier's law

$$\vec{\mathbf{F}} = -\lambda_{th} \boldsymbol{\nabla} T, \tag{4.26}$$

where $\boldsymbol{\nabla} T$ is the temperature gradient. The heat flux, $\vec{\mathbf{F}}$, quantifies the energy transportation as energy per unit area per unit time. As the temperature is radially isotropic, and using that the luminosity is the surface integrated energy flux, we find the energy transport equation at radial distance r from the core

$$\begin{aligned} \boldsymbol{\nabla} T \to \frac{dT}{dr} \quad &\Rightarrow \quad \vec{\mathbf{F}} \to F(r) \\ F(r) = \frac{L(r)}{4\pi r^2} &= -\lambda_{th} \frac{dT}{dr}, \end{aligned} \tag{4.27}$$

where $4\pi r^2$ is the surface area of the shell at radius r.

As mentioned we have to consider the density profile in the emissivity when calculating the luminosity from each shell, but also the balance of energy between individual shells. The energy from shell B a distance r from the core and with thickness dr is then not only the integrated emissivity over the volume of that shell, but also has a contribution from the preceding shell A starting at $r - dr$. This effect of course goes both ways, so the energy from shell B enters into shell C starting a distance $r + dr$ from the core. Adding these contributing terms we find the luminosity in shell C

$$\begin{aligned} L(r + dr) &= L(r) - \left(\frac{dU}{dt} + (\epsilon_c - \epsilon_h) \right) \Big|_{r+dr} \cdot dV \\ \text{or} \quad \frac{dL}{dr} &= -4\pi r^2 \left(\frac{dU}{dt} + (\epsilon_c - \epsilon_h) \right), \end{aligned}$$

where in the last step we have differentiated with respect to r using the volume element $4\pi r^2\, dr$ to get a general differential equation. Again we can express the change in internal thermal energy using heat capacity and the change in temperature [cf. eq. (4.1)], so we have

$$\frac{dL}{dr} = -4\pi r^2 \left(c_v \frac{dT}{dt} + (\epsilon_c - \epsilon_h) \right), \tag{4.28}$$

but instead of the total heat capacity we now must use the specific heat capacity valid for each individual shell. This is found by replacing the number of particles N with the

[16] As long as the thermal conductivity is non-zero.

number density n in eq. (4.5),

$$c_{v,i} = \frac{\pi\sqrt{x_i^2+1}}{x_i^2} n_i k_\mathrm{B} \left(\frac{k_\mathrm{B}T}{m_i c^2}\right), \tag{4.29}$$

where subscript i indicates the relevant particle specie. The total cooling and heating emissivity respectively is found as

$$\epsilon_c = \sum_i \epsilon_i \qquad \text{for each included cooling mechanism } i \tag{4.30}$$

$$\epsilon_h = \sum_j \epsilon_j \qquad \text{for each included heating mechanism } j. \tag{4.31}$$

Equation (4.28) can be solved for the change in temperature $\frac{dT}{dt}$ as a function of the luminosity gradient, and eq. (4.27) can be solved for the luminosity as a function of the temperature gradient. The result is the coupled set of equations found as

$$L = -4\pi r^2 \lambda_{th} \frac{dT}{dr} \tag{4.32}$$

$$\frac{dT}{dt} = -\left(\epsilon_c - \epsilon_h - \frac{1}{4\pi r^2}\frac{dL}{dr}\right)\frac{1}{c_v}, \tag{4.33}$$

which can be solved numerically given an initial temperature profile, $T_i = T(t=0, r)$. Written on this form we have to adjust the interpretation of luminosity slightly. Instead of only describing a source's emitted energy, it is now more appropriate to describe it as the thermal energy entering or leaving a specified volume shell, i.e. and energy flux. As the neutrino emissivity is highly dependent on temperature and density [cf. eq. (4.18)], both decreasing radially from the center, we expect the cooling of the core to be much more efficient than closer to the surface. Hence, early on in the cooling process when the temperature is sufficiently high, the neutrino cooling timescale might be shorter than the thermal conductivity timescale.[17] This would result in a positive temperature gradient in eq. (4.32), and a *negative* local luminosity. This is not actually unphysical, but merely describes a state in which the inward radial transportation of energy through conduction is larger than the locally emitted radiation energy.

The thermal conductivity is a complicated property of the micro-physics involved, and describes a given material's heat transport efficiency through thermal conduction. In degenerate matter the thermal conductivity is very high,[18] suggesting that neutron stars are to a good approximation in fact isothermal.[19] For now we use the results

[17] The time to reach local thermal equilibrium through conduction.

[18] Especially in degenerate electron gas, which is most likely always present in addition to the neutrons.

[19] Again, except in the atmosphere, where an appreciable temperature gradient is expected [cf. section 4.2.2].

from Flowers and Itoh (1981), which at least is a good approximation for a gas of pure neutrons in the density region around ρ_{nuc}

$$\lambda_{th} = \left(2.8 \times 10^{23}\,\text{erg}\,\text{cm}^{-1}\,\text{s}^{-1}\,\text{K}^{-1}\right)\frac{\rho}{\rho_{\text{nuc}}}T_8^{-1}, \tag{4.34}$$

where T_8 is the temperature measured in units of $10^8\,\text{K}$.

4.3.1 Adjustments from general relativity

In the previous sections we have taken energy conservation as a base assumption for all our discussion. Energy conservation is a bit more complex in general relativity, as one has to consider the relative reference frames of different observers. Energy should always be conserved in inertial reference frames, but in general relativity there are no such *true* inertial frames valid over sufficiently large volumes due to the curvature of spacetime. Taking the reference frame of a long distance observer[20] we can instead say that gravitational redshifted energy is conserved.

For example, *isothermal* objects in the Newtonian picture implies that the thermal energy, $k_{\text{B}}T$, is constant in the whole object. In general relativity however, it's the redshifted temperature that is constant in an isothermal star

$$\frac{d(T\mathcal{R})}{dr} = 0 \quad \Rightarrow \quad T\mathcal{R} = \text{constant}. \tag{4.35}$$

This means we have to make redshift adjustments to the energy transport from eq. (4.27), as well as the volume adjustments we saw in section 2.2.2. The resulting energy transport equation in general relativity is found as

$$\frac{d(T\mathcal{R})}{dr} = -\frac{1}{\lambda_{th}}\frac{L\mathcal{R}}{4\pi r^2\mathcal{V}}. \tag{4.36}$$

When adjusting the energy balance from eq. (4.28) we have to remember that the luminosity is energy per unit time. Thus the luminosity *gradient* must be redshifted twice. Once to adjust for the redshifted energy as before, and once to account for time running at different rates in each shell at increasing distance from the core. Similarly the cooling and heating rate must also be redshifted twice. In addition, the internal thermal energy must be redshifted once, and we have the usual volume adjustments. In the end we have the relativistic energy balance equation

$$\frac{d\left(L\mathcal{R}^2\right)}{dr} = -4\pi r^2\mathcal{V}\left(c_v\frac{dT}{dt}\mathcal{R} + (\epsilon_c - \epsilon_h)\mathcal{R}^2\right). \tag{4.37}$$

[20] That is an observer at such a distance that the local gravitational effects are negligible.

To simplify the equations, we define redshifted functions for temperature and luminosity as

$$T \to \mathcal{T} = T\mathcal{R}, \quad L \to \mathcal{L} = L\mathcal{R}^2. \tag{4.38}$$

We also define the baryon number a, the effective number of baryons in a volume, through the number density of baryons and the relativistic volume element

$$da = n_B \, d\mathcal{V} = n_B\big(4\pi r^2 \mathcal{V} \, dr\big). \tag{4.39}$$

We can then write the transport and balance equations as follows

$$\frac{d\mathcal{L}}{da} = -\left(c_v \frac{d\mathcal{T}}{dt} - (\epsilon_c - \epsilon_h)\mathcal{R}^2\right)\frac{1}{n_B} \tag{4.40}$$

$$\frac{d\mathcal{T}}{da} = \frac{1}{\lambda_{th}} \frac{\mathcal{L}}{(4\pi r^2)^2 n_B \mathcal{R}}. \tag{4.41}$$

Solving eqs. (4.40) and (4.41) for the relevant luminosity and temperature time derivative as before we finally have

$$\mathcal{L} = -\lambda_{th}\big(4\pi r^2\big)^2 n_B \frac{d\mathcal{T}}{da}\mathcal{R} \tag{4.42}$$

$$\frac{d\mathcal{T}}{dt} = -\left((\epsilon_c - \epsilon_h)\mathcal{R}^2 - n_B \frac{d\mathcal{L}}{da}\right)\frac{1}{c_v}. \tag{4.43}$$

Again these can be solved numerically given an initial temperature profile. The proper temperature and luminosity are reobtained post calculations, by applying the reverse transformations defined through eq. (4.38).

Part II

Numerical Methods, Solving the Equations

Chapter 5

Brief Introduction to the Numerics

In part I we have laid out the relevant theory needed to solve for the cooling curves for different models defined under our assumptions. In this part we'll discuss some final details we need to solve the equations presented in chapters 2 to 4 numerically. The boundary and initial conditions employed are presented, as well as some numerical considerations and methods used. When referring to different parts of the code structure, `monospaced` font is used to make a clear distinction. The framework is written in a way where the individual parts of the theory are first separated into template classes, defining the minimum attributes required in each class for them to communicate. By expanding upon these template classes, we are free to choose how each part is modeled, as long as it meets these minimum requirements. Throughout the development, the main goal has been a modular and flexible structure, utilizing well-established and tested Python libraries where possible.

As usual in numerical work, the continuous differential equations defined in the previous chapters are first discretized onto one-dimensional grids, before using interpolation methods to represent the solutions as continuous functions within the solution interval.

Software

In this project we've made use of Astropy[1], a community-developed core Python package for Astronomy (Astropy Collaboration, 2013, 2018). As well as SciPy[2], fundamental algorithms for scientific computing in Python (Virtanen et al., 2020).

[1] www.astropy.org
[2] www.scipy.org

5.1 The Modules Developed

As mentioned, each part of the theory are separated in to three modules with multiple available classes:

1. `ns_models` – Classes defining the «right hand side» (RHS) of the structural differential equations from chapter 2. These classes all inherits from a solver class, `solver_structure`, which handles the common operations for all the different classes.
2. `eos_models` – Classes defining the equation of state from chapter 3.
3. `cooling_models` – Classes defining the RHS of the cooling differential equations from chapter 4. Again, these classes inherits from a common solver class, `solver_cooling`.

In addition there is a collection of utility classes, combined into the `utils` module. Of the most important in regards to actual calculations, we have the `Numbers` class and `Scales` class defining the numerical scaling used throughout the code, which we'll come back to in section 5.2.

Instead of conventional storing of results by writing list of numbers to files, we've used the built-in Python module *'pickle'* (Van Rossum, 2020). Pickle includes binary protocols for writing entire Python objects with the objects hierarchy, methods, and stored attributes and variables. It also provides the reverse operation, allowing us to read and write entire instances of our models to file – with all solutions intact, but *also* the actual methods and relationships employed to obtain said solutions.

5.2 Numerical scaling

Common issues in numerical calculations involving a large range of different values are the stability and convergence of integration methods, and floating point precision of small numbers. As an example, we know the density profiles of neutrons stars possibly reach orders of $\mathcal{O}\big(10^{16} \sim 10^{17}\big)$ at the core, while approaching zero at the surface.[3] Also there is the ever troublesome treatment of different unit conventions. To handle this problem consistently for all possible combinations of models and future expansions, we developed the `Scales` class defining numerical scales appropriate on a case by case basis. This way the flexible behavior of the code is maintained, facilitating multiple convenient scaling choices for each individual module, while future extensions and other user defined scales are easily integrated into the code.

[3] Or at the top of the atmosphere to be precise.

`Scales` is largely reliant on the `Numbers` class, extracting physical constants from the Astropy collection, as well as converting them to cgs-units, to ensure a single collection of consistently defined constants to be used by all modules. It's for these classes the Astropy library was used. In particular the underlying *Constants* and *Units* modules, defining physical and astronomical constants and units according to various collections and standards, and allow for conversion between units. By default on our system installation, the physical constants are fetched from the CODATA 2018 collection, with the relevant numerical values as we've used them listed in chapter A.[4] However, to optimize for calculation speed, none of the three main modules use any of the Astropy functionality directly. Everything regarding units and unit conversions is done before and after calculations, by utilizing `Scales`.

All the scaling is based on the same logic and strategy, and is described by relations on the following form

$$Q = Q'Q^o, \tag{5.1}$$

where Q is the physical quantity with value and cgs-units, Q' is the scaled or *primed* quantity without units, and Q^o is the *scaling coefficient* between the physical and primed quantities. For individual problems, e.g. the Newtonian stellar structure, a complete set of Q^o values for the problem's constituent physical quantities and relevant equations define the problem's so-called *scaling*. For a scaling to be self-consistent, the different Q^os are dependent, and in most cases defined by choosing a *base* for one or two of the involved quantities. During the development and experimentation of this project, multiple different scales with different bases have been implemented. Here we'll restrict ourselves to the two types which we found most convenient in each case. The first is the so-called *cgs scaling*, where all Q^o coefficients are unity with only the relevant units, which is equivalent to solving the system without numerical scaling.[5] This type of scaling is defined for all the three main modules and their subclasses, and is mainly used as a set of scales to present figures in proper units. For the scaling employed in the calculations, we have to look at each of the problems we are trying to solve.

[4]The Astropy library also facilitates changing the base collection for physical constants to updated (as well as older) versions, from both the CODATA group and others. As we are fetching all our values of physical constants from their definition in Astropy, our code is flexible in terms of the collection versions defined in Astropy.

[5]Note however, cumbersome unit conversions and handling will be automatically dealt with by the `Scales` class.

Chapter 6

Solving for the Stellar Structure; `ns_models`

The matter in the neutron star is highly degenerate and thus treated as static. This simplifies the calculations considerably, by separating the one-dimensional structure calculations into a closed time-independent problem. The solution of which to be used in the cooling calculations, without having to recalculate the structure of the star between each time step of the cooling. Therefore our first milestone of development was defining the framework for solving the stellar structure; the mass $m(r)$, pressure $P(r)$, density $\rho(r)$ and metric functions $\Phi(r)$ and $\lambda(r)$, all as functions of the radius r.

In the following we've limited the discussion to the general relativistic structure equations (TOV), as the Newtonian case is not that relevant for neutron stars. However, here we meet our first example of the flexibility of our code and the way it's intended to be expandable. As mentioned, all common operations regarding initialization and scaling using the `Scales` class, the actual integration of a given set of equations, verbose reports of the solver progress, storing and treating the results, and other useful operations that is unchanging under the two gravitational theories, are combined into an underlying solver class, the `solver_structure`. To implement the models defined by the two sets of coupled equations from chapter 2, all we have to do is define a new class inheriting all functionality of the solver class – only specifying the RHS of the differential equations to be solved. The Newtonian case was therefore actually the first to be implemented, used as a simple test of the «flow» of the framework. We later just expanded the `ns_models` module, to also have classes for the TOV equations with various bases for scaling.

6.1 Boundary Conditions

Sources like Shapiro and Teukolsky (1983) and Thorne (1977) list the general relativistic stellar model equations and their boundary conditions starting at zero radius $r = 0$. We found that this immediately breaks down in a numerical treatment, clearly visible from the equations in chapter 2. Illustrating examples of this are eq. (2.6) for the Newtonian pressure gradient or eq. (2.20) for the relativistic volume correction, being undefined for $r = 0$.

A similar surface boundary condition at zero pressure, $P(r_s) = 0$, defining $R = r_s$ as the surface radius, is also suggested in Shapiro and Teukolsky (1983). However, this has multiple numerical and physical problems. Our assumptions of totally degenerate matter must break down near the surface when the pressure and density go to zero, and we'll also encounter problems when calculating a surface luminosity [cf. chapter 8] if the volume cells near the surface approach a zero particle number density. We are also integrating from large initial values of pressure at the core, all the way down to zero pressure, which is cumbersome numerically.[1] To facilitate flexible and model dependent boundary conditions[2] we instead treated the system of differential equations as an *initial value* problem, and integrated outwards throughout the radial profile of the star with initial conditions defined at the core. The surface boundary conditions are then imposed by a *termination*-event

$$\rho_0(r) < \rho_{0,\mathrm{tol}}, \tag{6.1}$$

that *if* satisfied ends the integration, where $\rho_{0,\mathrm{tol}}$ is an input parameter in the code defining a desired surface rest mass density. We chose the rest mast density for this condition, as it's the most consistently defined quantity for all the possible equations of state. We found this choice of boundary determination to be favorable over other methods for a handful of reasons. As we'll see in the eventual results in part III, most equations of state results in fairly uniform interior density and pressure profiles. Closer to the surface a large gradient is found, thus the profiles going rapidly to zero. At this point the actual observables stop increasing noticeably,[3] and so the exact value we chose for $\rho_{0,\mathrm{tol}}$ is not that important as long as it is sufficiently low and consistent across model types. We also saw an example of this in fig. 2.1, especially evident for higher core densities. In addition, different particle compositions, like the *n-p-e* equilibrium gas of section 3.3.1, turns out is only achievable above certain density limits, further advocating for a flexible non-zero surface boundary condition. To complete the integration all the way to zero density, it's rather common to *glue* on an envelope model describing the transition from the crust throughout the atmosphere of the neutron star, using the endpoint of the interior as initial boundary conditions. As such, by ending all the interior profiles at an input surface boundary density, we facilitate future implementations of

[1] Although this is somewhat dealt with through numerical scaling of the equations.

[2] Both for the models currently implemented, and possible future extensions.

[3] Observables being the radius and mass which are features of neutron stars we are actually able to observe, in contrast to pressure and density.

our own envelope models. For now, we are using the relationship between the boundary temperature and effective temperature in eq. (4.22), and by specifying the same surface density in all our structural profiles we obtained a better and more consistent foundation for the surface luminosity, which will be discussed further in chapter 8.

Guided by the logic outlined above we defined the initial and boundary conditions in following fashion:

1. Define a fixed low value for the initial radius point, or the *core* radius. We chose $r_c = 1 \times 10^{-4}\,\mathrm{cm}$.
2. Pick a value for the core density, $\rho(r_c) = \rho_c$. The EoS then gives the core pressure, $P(r_c) = P(\rho_c) = P_c$.
3. Assume a small core of radius r_c and constant density ρ_c. The cumulative mass of the spherical volume limited by r_c is then $m(r_c) = m_c = \rho_c \frac{4\pi r_c^3}{3}$.
4. The differential equation for the gravitational potential is linear in Φ, and is restricted to join smoothly onto the Schwarzschild metric at the surface ($r = R$). We therefore just chose an initial value at the core, and simply added a constant to Φ throughout the profile of the star post calculations so that eq. (2.18) is satisfied. We chose $\Phi(r_c) = \Phi_c = -0.5$.
5. Pick a value for the desired surface density, $\rho_{0,\mathrm{tol}}$. The point where the density reaches this desired value defines the surface values of pressure through the EoS, and the observables total radius, R, and total mass, M. Following Page et al. (2006) and Kouvaris (2008), with references therein, we chose $\rho_{0,\mathrm{tol}} = 10^{10}\,\mathrm{g\,cm^{-3}}$.

Thus the whole system is determined by the choice of EoS and the central and boundary density. We therefore solved for a wide range of initial core density values to create curves of total mass parameterized in terms of central density, for each available EoS. By later specifying a desired mass, we can find the value required as input core density to produce structural profiles corresponding to the specific mass. This is especially useful to easily compare the cooling curves of neutron star models of varied sizes [cf. chapter 8].

However, as we'll see in part III, this total mass versus core density relationship is a bit more complicated than the Newtonian theory make it seem to be in fig. 7.1. Direct comparison of the two theories of gravity is not straightforward as so much of the gravitational effects in general relativity is attributed to the temporal component of spacetime, for which there are no analogous parts in Newtonian theory. Without going into too much detail, when regarding compact objects such as neutron stars and black holes, the effects of «gravity» is stronger in general relativity – which can be inferred from looking at eq. (2.25), all the relativistic adjustments being ≥ 1. We'll briefly come back to this in section 9.2.1. For now we just point out that under general

relativity we find a maximum achievable total mass at a specific core density, call it $\rho_{c,\max}$, and solutions with higher core densities turn out to be unstable. Therefore, only the solutions resulting from the range of core densities equal to and below $\rho_{c,\max}$ is used in the parameterization.

6.2 The Schwarzschild Scale

We found the most convenient scaling to be based on the solar mass and solar Schwarzschild radius

$$M^o = 1M_\odot \tag{6.2}$$

$$R^o = 1R_{\mathrm{S}\odot} = \frac{2GM_\odot}{c^2}. \tag{6.3}$$

Neutron stars having typical mass $\sim 1M_\odot$ and radius $\sim 10\,\mathrm{km}$, this results in our primed quantities for mass and radii being of order unity.[4] Then the scaling of pressure and density was found, based on the chosen coefficients for mass and radii, by demanding that physical constants like G and c vanish from our equations. For this we used

$$\rho^o = \frac{c^6}{32\pi G^3[M^o]^2} = 6.14 \times 10^{15}\,\mathrm{g\,cm^{-3}} \tag{6.4}$$

$$P^0 = \rho^o c^2 = 5.52 \times 10^{36}\,\mathrm{Ba}, \tag{6.5}$$

where square brackets around primed quantities or scaling coefficients with exponents are used to avoid confusing them with function variables. By inserting the mass, radius, density, and pressure written on the form of eq. (5.1) in the equations for stellar structure [cf. eqs. (2.24) to (2.26)], we solved for the primed quantities to obtain the dimensionless equations

$$\frac{dm'}{dr'} = \left[r'\right]^2\rho' \tag{6.6}$$

$$\frac{dP'}{dr'} = -\frac{m'\rho'}{2[r']^2}\left(1+\frac{P'}{\rho'}\right)\left(1+\frac{[r']^3P'}{m'}\right)\left(1-\frac{m'}{r'}\right)^{-1} \tag{6.7}$$

$$\frac{d\phi'}{dr'} = -\frac{1}{\rho'}\frac{dP'}{dr'}\left(1+\frac{P'}{\rho'}\right)^{-1}. \tag{6.8}$$

In the code the boundary conditions are given as input prior to scaling in cgs-units. The primed boundary conditions are then found according to the $Q' = Q/Q^o$ relations, before the system of dimensionless equations is solved. Post calculation, the solved physical quantities are reformed as $Q = Q'Q^o$.

[4] Also, a lot of the GM/c^2 factors from general relativity are easy to cancel out.

6.3 Integrating Through the Profile

With the initial conditions defined we used `solve_ivp`, SciPy's *initial value problem* solver to integrate the set of dimensionless equations. The SciPy library offers faster, more precise, and flexible solvers than we would have time to develop from scratch, being highly customizable, with multiple rigorous and optimized integration methods built-in. From among these, the *'DOP853'* method was applied, an explicit Runge-Kutta method of order 8 with a 7-th order polynomial interpolation fit of the solver data to create continuous functions. 'DOP853' was chosen based on it's recommendation in the documentation[5] of `solve_ivp` to solve with high precision. Instead of user-defined radial infinitesimal step length, `solve_ivp` takes a relative- and absolute tolerance as parameters. The local step length between each grid point i and $i+1$ is then optimized through a finite differencing scheme according to the specified integration method while requiring that the local error estimate in each step is less than

$$\Delta_a + \Delta_r \cdot \max |y_{i+1}|. \tag{6.9}$$

Here Δ_a is the absolute tolerance, Δ_r is the relative tolerance and $\max |y_{i+1}|$ is the absolute value of the largest solution quantity at step $i+1$, obtained through finite differencing. The optimal values of Δ_a and Δ_r for each specific case are hard to define. Instead we experimented with multiple models at once, gradually increasing the tolerance values until we reached the first noticeable changes in any of the results. This way we also got some insight into the numerical stability of different EoSs and numerical scales. The tolerance values were then chosen to be equal, and two orders of magnitude lower than the first value producing noticeable errors

$$\Delta_a = \Delta_r = 1 \times 10^{-6}. \tag{6.10}$$

Both the integration *method* and tolerance values are possible input parameters to the code, allowing user modifications.

Through explicit methods, values for the integrated quantities at some grid point $i+1$ are obtained using the values from the previous grid point i. When implementing eqs. (6.6) to (6.8) numerically it has to form a closed system dependent only on the actual solver variables m_i', P_i' and Φ_i'. As discussed, to close the system the EoS is also required, but it is actually needed on the form $\rho_i' = \rho_i'(P_i')$ to fit in the numerical scheme. We'll continue this discussion in chapter 7.

After integration, `solve_ivp` returns interpolated objects of the main solver variables which we can use to create arrays of the solution profiles with any number of grid points within the interval of the interpolation. For the structural profiles we chose to use 10^4 number of points to extract m_i', P_i', and Φ_i', which then is used to calculate the corresponding arrays for rest mass and energy density profiles from the EoS. Here

[5] docs.scipy.org/scipy.integrate.solve_ivp

we found the termination-effect methods integrated into `solve_ivp` to be less precise than desired. The density profile gradient is very steep at the boundary, evident in the Newtonian example of fig. 2.1 but even more extreme in some of the results we'll see in part III. Therefore the last step of integration is prone to overshoot the given input boundary density. Instead, we utilized the interpolated objects to define our own post calculation smoothing of the endpoints to be used for each solution. As we have an interpolation for $P(r)$, we find the exact radius value that in turn gives a rest mass density $\rho_{0,\mathrm{tol}}$ through the EoS, which then defines the boundary radius r_b we use as the total radius of the star R. The part of the solutions overshooting the tolerance value is just discarded. The metric function Φ_i' is also treated following section 2.2.2. The surface condition value defined by eq. (2.18) is found using the total mass and radius, then the whole interior profile for Φ' is adjusted as

$$\Phi' \to \Phi' + \Delta\Phi'_{\mathrm{b}}, \tag{6.11}$$

where $\Delta\Phi'_{\mathrm{b}}$ is the difference between the boundary value required by the Schwarzschild metric and the actual value obtained for the surface through integration. We also evaluate the function for radii 20 % beyond the radius of the star, still using the mass $M = m(R)$, as a test to ensure that it's continuous all the way from the core extending out into empty space. Lastly, the λ metric function is found by eq. (2.17) using the full mass and radius profiles. All of these arrays are stored, along with the interpolation objects and other useful solver info in a dictionary inspired by the *'json'* format, one such dictionary for each solution of different initial core densities.

The mentioned post calculation smoothing technique is also expandable and flexible. We found the surface density tolerance to be favorable for the comparison we've done, but as the framework is intended to study neutron stars under various conditions we also facilitate simple implementation of other conditions used to define the boundary. In addition to the mentioned method to ensure a consistent surface density across all model types, we've experimented with a few other termination or tolerance events, but will not mix in the results of using them in the thesis. Two of these defines the boundary at the radius where the mass stop *increasing* significantly, or where the pressure stop *decrease* significantly – both compared to tolerance values of the gradients.[6]

[6]This was developed to deal with problems we encountered when using the ultra-relativistic polytropic formula [cf. section 9.2.1].

Chapter 7

Implementing the Equation of State; `eos_models`

As in the `ns_models` module, `eos_models` is a collection of classes where each class is defining the different equations of state from chapter 3. For each class implemented, and future possibilities, there are two minimum behaviors that must be met. The $P = P(\rho)$ relation for the initial conditions [cf. section 6.1],[1] but also the inverse $\rho = \rho(P)$ which is needed in the TOV-equations [cf. section 6.3]. This was implemented using a similar strategy for each model from chapter 3, with appropriate scaling and numerical details outlined below. The strategy is simply put to precompute and tabulate monotonically increasing quantities to create the inverse relations by interpolation.

7.1 Common Features

For coherency between different models, the template EoS class is constructed with one method giving the pressure with *rest* mass density as input, and one method giving *both* the rest mass density and full mass density with pressure as input.

The scaling is dependent on the scale in use for the structural equations, particularly the scale for pressure and density. Hence, a scheme demanding all numerical constants to vanish is unfeasible in general. Instead we aimed to group such eventual numerical constants into precalculated dimensionless factors, reducing the number of floating point operations (FLOPS) wherever possible [cf. eqs. (7.5) to (7.7)]. In each case, the scale for pressure and density is continued from the accompanying structural scaling, as they

[1] In hindsight, we could have defined the core boundary values from an input pressure and only really required the inverse relation. However, it is conventional to use the central density and the $P = P(\rho)$ form in most sources. For a general model, the reverse relations are obtained through solving and tabulating the given $P = P(\rho)$ relations, thus requiring its numerical implementation anyway.

describe the same quantity. The energy density and number density is then conveniently scaled as

$$\epsilon^o = \rho^o c^2 = 5.52 \times 10^{36}\,\mathrm{erg\,cm^{-3}} \tag{7.1}$$

$$n^o = \frac{\rho^o}{m_n} = 3.67 \times 10^{39}\,\mathrm{cm^{-3}} \tag{7.2}$$

so that the primed mass and energy density are equal, $\rho' = \epsilon'$, and the primed number and rest mass density, $\rho'_{0,n} = n'_n$, are equal for models including only neutrons. The numerical values listed in this section assume the Schwarzschild scaling introduced in section 6.2 has been chosen for `ns_models`. Possible other scales for the structural part are treated automatically in the `Scales` module, resulting in different obtained values for the coefficients of energy and number density. For the rest of the dimensionless constants we have to consider the remaining relevant equations for each model separately. In each case we describe the process for implementing the desired equations while referring to the full equations from chapter 3 for simplicity, but keep in mind that the scaling of each model is determined at initialization – and all solving is done on the dimensionless equations.

7.2 Contributions to the Mass

The equations of state presented in chapter 3 are all by construction including similar contributions to the mass of the star [cf. section 2.2.2]. Of course, the rest mass energy should always be included. The kinetic energy is incorporated in the definition of energy density from eq. (3.3), so at least the two Fermi EoS provide the same types of contributions. The simple polytropic formula indicates that only the rest mass energy should contribute to the mass, from solving the algebraic equation for the rest mass density. However, as discussed in section 2.2.2, it would be wrong to only allow *rest* mass contributions to the total mass in relativistic theory. To account for this we implemented the EoS in such a way that the rest mass resulting from solving eq. (3.21) is in turn used to find the relativity parameter, and then the corresponding full energy density using eq. (3.15).[2] This is described in more detail in section 7.3. Thus, the polytropic EoS is constructed to also include kinetic energy contributions. The last and most realistic EoS, from Gandolfi (2012), includes the kinetic energy, but also the energy associated with the 2n- and 3n-interactions as the ideal gas approximation is abandoned.

To demonstrate the discrepancy in the resulting neutron star profiles when wrongly using only rest mass energy in the TOV equations, the polytropic and QMC EoS classes

[2] We found during the research phase of this project that many authors seem to not recognize this discrepancy, or at least makes it really hard to determine exactly what sort of density that is described in different circumstances by using poor notation. That's why we have gone out of our way to distinguish between the *rest mass density* and *mass density* throughout this thesis.

in `eos_models` are accompanied by simplified sibling-classes. These classes intentionally only consider the rest mass density in both the two outputs of the $\rho = \rho(P)$ relationship. In the case of the polytropic EoS this was trivial, as we only had to solve the algebraic equation. For the QMC EoS, this was done by just not adding the kinetic and interaction energies to the rest mass before returning them. The purpose of this was mainly to mend our own sanity, after struggling to reproduce results found in similar papers and theses during development – the authors of which not describing how they dealt with this issue when using the polytropic approximation. Hence, reproducing and comparing to their claimed results proved difficult.

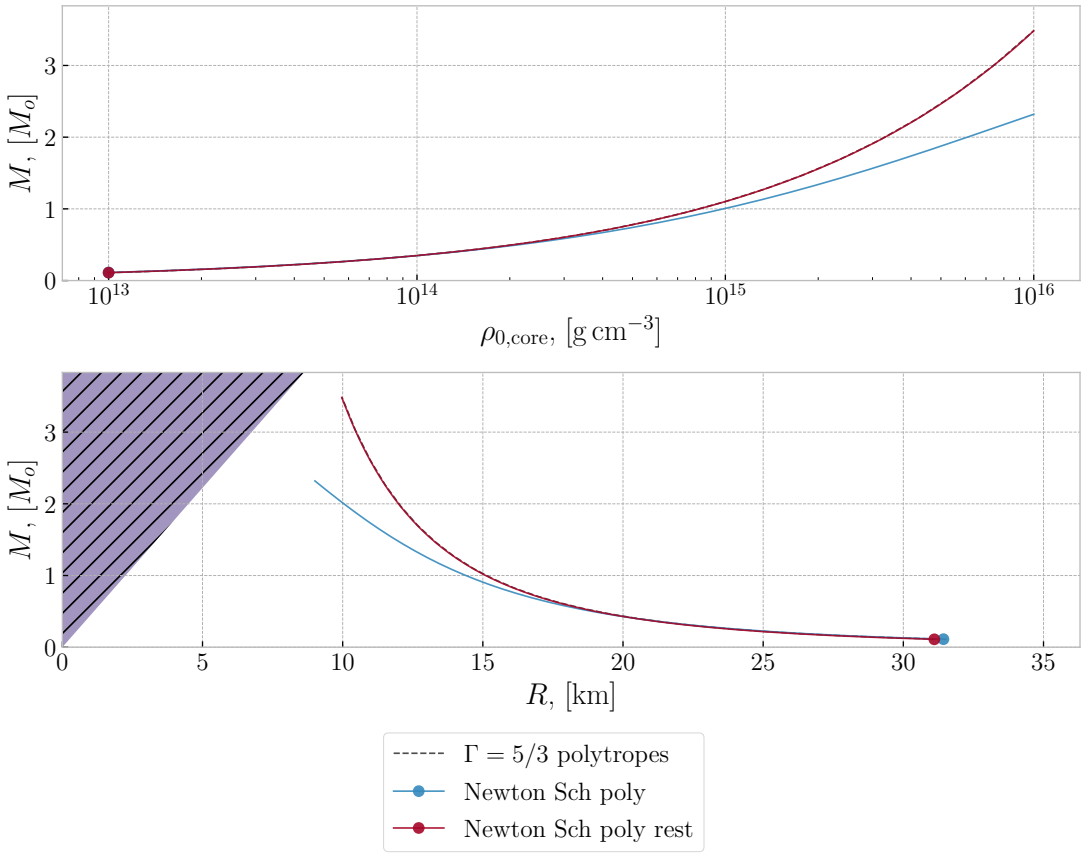

Figure 7.1: Demonstration of the contribution to total mass from the polytropic EoS under Newtonian gravity. In blue and red are the non-relativistic polytropic EoS, where the red curve is the rest mass only model. The dashed black line shows the analytical Newtonian *polytrope* of the same adiabatic index. In the top panel the parameterized total mass vs core density is shown, and the total mass vs corresponding total radius is shown in the bottom panel.

By having the «rest mass only» version available, we can also easily solve the Newtonian case without the added mass from relativistic theory, providing proper grounds

for comparison between fully relativistic theory, relativistic theory with Newtonian gravity, and pure classical theory. We have intentionally not mentioned this regarding the demonstrative profile figure in section 2.1, as too many details were lacking.[3] At this point however, we are equipped to describe the two subtly different curves seen in fig. 2.1. The mentioned parameterized total mass and radius obtained from a wide range of core density values is shown in fig. 7.1, conveying the effect of including kinetic contributions to the mass. The blue curve describes a Newtonian neutron star using the proper polytropic EoS, with kinetic energy included in the energy density. The red curve shows the other case, using the same polytropic EoS but only rest mass energy contributions. As we can see, at low densities the two models are more or less equal, as the relativistic energy of particles is small compared to their rest mass energy. At higher densities however, the difference is substantial. There's also a black dashed line in fig. 7.1, barely visible under the red one, showing the analytical solution from a so-called Newtonian *polytrope*. These are approximations can be solved analytically for the total mass and radius as functions of central density, with a specified adiabatic index, assuming only rest mass density in the cumulative mass. As we can see, the analytical solutions are a good fit to our results from the pure classical theory. The analytical expression we've used are taken from Shapiro and Teukolsky (1983), given as

$$R = (14.64\,\mathrm{km})\left(\frac{\rho_{0,c}}{10^{15}\,\mathrm{g\,cm^{-3}}}\right)^{-1/6} \tag{7.3}$$

$$M = (1.102\,\mathrm{M_\odot})\left(\frac{\rho_{0,c}}{10^{15}\,\mathrm{g\,cm^{-3}}}\right)^{1/2} \tag{7.4}$$

7.3 The Polytropic EoS - Pure Neutron Gas

The polytropic formula lends itself easily to numerical implementation as a simple algebraic expression between the pressure and *rest* mass density [cf. eq. (3.21)]. However, it's the full mass density that's needed in accordance to the template class.[4] Therefore, the $P = P(\rho_0)$ relation [cf. eq. (3.21)] is tabulated before any structural calculations in the initialization of the full neutron star model. The wide range of rest mass densities and corresponding pressures are interpolated to create the «continuous» $\rho_0 = \rho_0(P)$ relation needed, spanning all achievable values during the calculations. The number density is found from the rest mass density, and then the relativity parameter is found by eq. (3.11). Finally, the relativity parameter is used to calculate the full energy density using eq. (3.15), and a $\rho_0 = \rho_0(\epsilon)$ relation is established by interpolation. To optimize the number of FLOPS, an $\epsilon = \epsilon(x)$ interpolation is also created to avoid recalculating eq. (3.16) in full many times.

[3] However, a deductive reader may have noticed the connection between *rest* mass and the label «rest» in the legend of fig. 2.1, after the discussion in section 2.2.2.

[4] Remember that the template class is constructed to answer the demands of the numerical implementation of the TOV-equations.

At initialization of the EoS, the relativistic or non-relativistic limit must be defined, and by default, the non-relativistic approximation is chosen. This affects the stiffness of the system, but also the numerical scaling and grouping of factors. Equations (7.5) to (7.7) demonstrates the applied logic to find the mentioned eventual numerical factors, with the values obtained listed in table 7.1.

$$P' = \frac{\kappa[\rho^o]^\Gamma}{P^o} \cdot \left[\rho'\right]^\Gamma = \mathcal{P}_{\text{poly}} \cdot \left[\rho'\right]^\Gamma \tag{7.5}$$

$$\epsilon'_n = \frac{m_n c^2}{\lambda_n^3 \epsilon^o} \cdot \chi(x_n) = \mathcal{E}_{\text{Fermi,n}} \cdot \chi(x_n) \tag{7.6}$$

$$\rho'_0 = \frac{m_n}{3\pi^2 \rho^o \lambda_n^3} \cdot x_n^3 = \mathcal{N}_{\text{Fermi,n}} \cdot x^3 \tag{7.7}$$

7.3.1 A Uniform Density Solution

For comparison to analytical cooling results of isotherm, uniform neutron stars [cf. section 8.2], an additional EoS «model» was needed, providing a simple example of the expandability of the code structure. We simply defined a new class in the `eos_models` module, inherited all functionality of the normal polytropic EoS, but redefined the method calculating the resulting density of a given pressure. Instead of applying the inverse polytropic relation, the input core rest mass density and full mass density are returned for *any* input value of pressure.

7.4 The Fermi EoS

7.4.1 The Pure Neutron Gas

The full Fermi EoS is of course very similar to the polytropic case, but without the same simple algebraic expression to easily find the rest mass density and relativity parameter. To obtain the reverse relations the EoS was tabulated at initialization as before, but with a slightly different approach. As both the pressure and energy density are monotonically increasing in x_n, the tabulation is now based on a wide range of possible neutron relativity parameter values. The reverse $x_n = x_n(\epsilon_n)$ and $x_n = x_n(P_n)$ relationships are obtained by solving eqs. (3.13) and (3.15). Then, by eqs. (3.11) and (3.12), the rest mass density corresponding to the same range of x_n values was found to create $\epsilon_n = \epsilon_n(\rho_{0,n})$. The methods required by the template class is then achieved as

$$P'_n\big(\rho'_{0,n}\big) = P'_n\big(x_n\big(\epsilon'_n\big(\rho'_{0,n}\big)\big)\big) \tag{7.8}$$

$$\epsilon'_n\big(P'_n\big) = \epsilon'_n\big(x_n\big(P'_n\big)\big) \tag{7.9}$$

$$\rho'_{0,n}\big(P'_n\big) = \rho'_{0,n}\big(x_n\big(P'_n\big)\big), \tag{7.10}$$

Table 7.1: Dimensionless factors obtained from scaling, following the logic outlined in eq. (7.11), assuming the Schwarzschild scaling base applied for `ns_models` [cf. section 6.2]. By using or defining another base scaling the `Scales` class would output adjusted dimensionless factors.

Factor	Composition		Obtained numerical values		
		*model:	$\mathrm{QMC}_{\mathrm{none}}$	QMC_3	$\mathrm{QMC}_{\mathrm{UIX}}$
$\mathcal{E}_{\mathrm{QMC,a}}$	n		0.063	0.064	0.071
$\mathcal{E}_{\mathrm{QMC,b}}$	n		2.248	7.825	12.32
$\mathcal{P}_{\mathrm{QMC,a}}$	n		0.031	0.031	0.037
$\mathcal{P}_{\mathrm{QMC,b}}$	n		5.080	19.33	30.00
		†i:	n	p	e^-
$\mathcal{E}_{\mathrm{Fermi,i}}$	n or npe		29.4	29.3	2.58×10^{-12}
$\mathcal{N}_{\mathrm{Fermi,i}}$	n or npe		0.994	0.99	1.6×10^{-10}
		‡limit:	$x \ll 1$	$x \gg 1$	
$\mathcal{P}_{\mathrm{poly}}$	n		0.201	0.251	

* We show three of the QMC EoS from table 3.1 using our label names.
† For pure n Fermi EoS, the values under p and e^- are just not considered.
‡ For the non-relativistic ($x \ll 1$) and ultra-relativistic ($x \gg 1$) limits respectively.

with eqs. (3.11), (3.13) and (3.15) reduced to the dimensionless form

$$\begin{aligned} P'_n &= \mathcal{E}_{\mathrm{Fermi,n}} \cdot \Theta(x_n) \\ \epsilon'_n &= \mathcal{E}_{\mathrm{Fermi,n}} \cdot \chi(x_n) \\ n'_n &= \mathcal{N}_{\mathrm{Fermi,n}} \cdot x_n^3. \end{aligned} \tag{7.11}$$

Here the numerical factor for pressure and energy density are equal, again listed in table 7.1.

7.4.2 The *n-p-e* Gas

The Fermi EoS for a pure neutron gas is actually a special case of the Fermi npe EoS, only with a zero contribution from the electrons and protons. The actual class implementing the EoS discussed above is in practice a subclass of the full Fermi EoS, redefined to only include contributions from neutrons. Thus, the general approach is already described for the pure neutron gas, but we have to consider some details. Equations (3.32) to (3.34) are defined as sums over individual particle contributions, each contribution determined by x_i for particle species i. However, the beta equilibrium

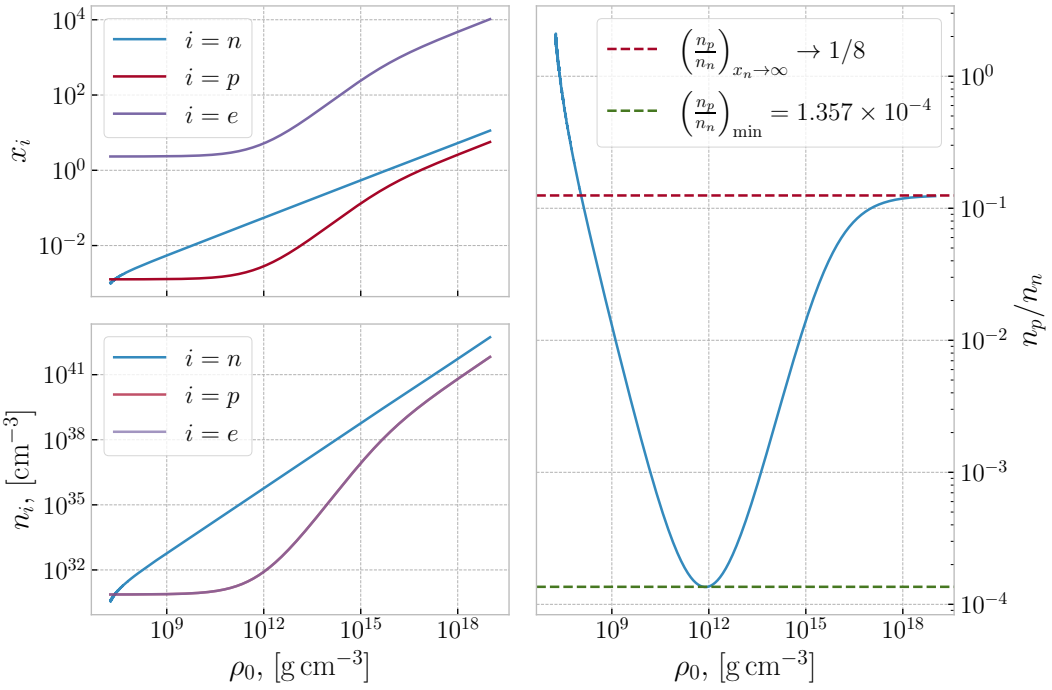

Figure 7.2: Relativity parameter, number density and proton-neutron fraction for the Fermi npe. In the right panel the green and red horizontal dashed lines indicate the theoretical limits of the proton-neutron fraction. For densities $< 1.2 \times 10^7$ g cm^{-3} the beta-equilibrium solution should no longer include neutrons ($n_n \to 0$), consistent with our solution becoming slightly unstable for the lowest densities shown.

solution enforce a $1-1$ relation between the relativity parameters at any given density, as discussed in section 3.3.1. By inserting eq. (3.31) into eq. (3.28), the proton to neutron number density fraction is given as a function of x_n

$$\frac{n_p}{n_n}(x_n) \simeq \frac{1}{8}\left(\frac{1 + 4Q/(m_n x_n^2) + 4(Q^2 - m_e^2)/(m_n^2 x_n^4)}{1 + 1/x_n^2}\right)^{3/2}, \tag{7.12}$$

where Q is the difference in mass between neutrons and protons [cf. eq. (3.26)], and we have used that both m_e and Q are $\ll m_n$ (Shapiro and Teukolsky, 1983). We therefore solved eq. (7.12) for the relevant range of x_n values, to find the proton-neutron ratio. The individual number densities are then easily obtained from the ratio, applying charge neutrality to infer the electron density. Then the relativity parameters are found by eq. (3.11), scaled appropriately to each species. Finally, the electron and proton relativity parameters corresponding to the range of x_n values were interpolated as before. With these $1-1$ relations at hand, we followed the same approach as for the pure neutron case for finding the reverse EoS relations as functions of the neutron relativity parameter. But instead of only neutrons contributing, the relativity parameter of electrons and protons corresponding to the given x_n are first found, before summed according to

eqs. (3.32) to (3.34) to give the total pressure and density. The baryon number density was found by the neutron number density and the proton-neutron ratio. The resulting x_is, n_is and proton-neutron fraction for increasing rest mass density is demonstrated in fig. 7.2.

The numerical factors for each species are listed in table 7.1, following the logic in eq. (7.11). The full quantities are then obtained by summing over each particle's contribution, e.g.

$$P'_{\text{tot}}(x_n) = \mathcal{E}_{\text{Fermi,n}} \cdot \Theta(x_n) + \mathcal{E}_{\text{Fermi,p}} \cdot \Theta(x_p(x_n)) + \mathcal{E}_{\text{Fermi,e}} \cdot \Theta(x_e(x_n)). \tag{7.13}$$

7.5 The QMC EoS

The equation given in terms of non-rest mass energy per particle in Gandolfi (2012), we find a set of equations on a form similar to that of sections 3.2 and 3.3 by writing eq. (3.36) in terms of the energy density instead of energy per particle. For N neutrons in a volume V, each with energy E, the total energy is simply $E_{tot} = NE(n)$ and the associated energy density is $\epsilon = E_{tot}/V = nE(n)$. The pressure is found from the energy density through the identity

$$P \equiv n^2 \frac{\partial(\epsilon/n)}{\partial n} = n\frac{\partial \epsilon}{\partial n} - \epsilon.$$

Equation (3.36) only includes the energy associated with the interaction potentials and the kinetic energy of each neutron, so to get the full energy density similar to before we must add the rest mass energy density as well. We arrive at the EoS, now determined in terms of eqs. (7.14) and (7.15)

$$\epsilon(n) = a\frac{n^{\alpha+1}}{n_0^\alpha} + b\frac{n^{\beta+1}}{n_0^\beta} + \rho_0(n)c^2 \tag{7.14}$$

$$P(n) = a\alpha\frac{n^{\alpha+1}}{n_0^\alpha} + b\beta\frac{n^{\beta+1}}{n_0^\beta}, \tag{7.15}$$

where the rest mass density ρ_0, is given by eq. (3.12).

The implementation of the QMC EoS followed closely the approach of the pure neutron Fermi EoS, but with eqs. (7.14) and (7.15) being functions of number density, the tabulation was now based on a wide range of n_n values. The numerical factors are, as for the polytropic case, dependent on the choice of model – i.e. choice of 3n-potential. By specifying the desired label-name for the QMC EoS as described in table 3.1, the fitting coefficients are determined, and the numerical factors follow as

$$\begin{aligned}\epsilon' - \rho'_0 =& \frac{a[n^o]^{\alpha+1}}{\epsilon^o n_0^\alpha} \cdot \left[n'\right]^{\alpha+1} + \frac{b[n^o]^{\beta+1}}{\epsilon^o n_0^\beta} \cdot \left[n'\right]^{\beta+1} \\ =& \ \mathcal{E}_{\text{QMC,a}} \cdot \left[n'\right]^{\alpha+1} + \ \mathcal{E}_{\text{QMC,b}} \cdot \left[n'\right]^{\beta+1}.\end{aligned} \tag{7.16}$$

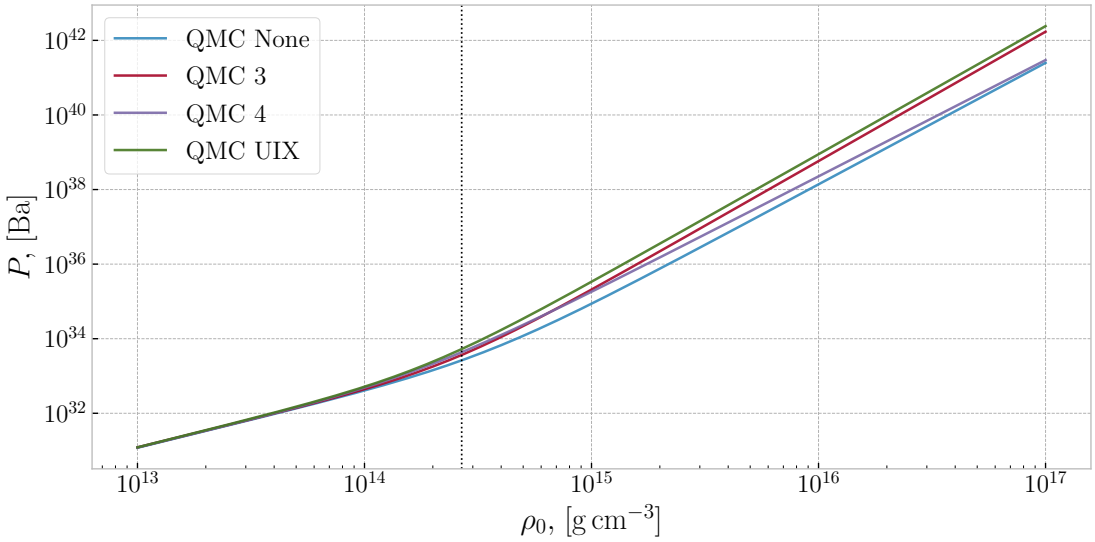

Figure 7.3: The resulting pressure as function of rest mass density for the three different QMC EoS listed in table 7.1. Note how each model converges for low densities, where the contribution from the 3n potential should be small. In the high density regime, the effect of the poorly constrained 3n potentials causes the different models to converge. We also see the transition above the saturation density, effectively stiffening the EoS.

where the contribution from the rest mass density is dealt with separately, easily obtained from the number density. Similarly for pressure the factors are determined as

$$\begin{aligned} P' &= \frac{a\alpha[n^o]^{\alpha+1}}{P^o n_0^\alpha} \cdot \left[n'\right]^{\alpha+1} + \frac{b\beta[n^o]^{\beta+1}}{P^o n_0^\beta} \cdot \left[n'\right]^{\beta+1} \\ &= \quad \mathcal{P}_{\mathrm{QMC,a}} \cdot \left[n'\right]^{\alpha+1} + \quad \mathcal{P}_{\mathrm{QMC,b}} \cdot \left[n'\right]^{\beta+1}. \end{aligned} \tag{7.17}$$

The resulting $P(\rho_0)$ relationship we found for the four emphasized models are included in fig. 7.3. Following the discussion in section 3.4, we find the QMC none and UIX to be on each side of the extreme, differ roughly one order of magnitude in the resulting pressure at high densities. The QMC 3 (red) and 4 (purple) are shown in the middle. We showcase these two in particular as they have an interesting relationship slightly above the saturation density n_0 marked with the vertical dotted line. The QMC 3 model is constructed with a high value for β (steep slope above n_0) and low value for b (low pressure for low densities) compared to the QMC 4, constructed the other way around. The behavior is evident in our results, especially clear at higher densities where the QMC 3 model approaches the extreme UIX pressures while the QMC 4 is closer to the soft QMC none model. It's a bit harder to make out at low densities, but we see the red line initially at a lower pressure than the purple, before they cross at densities $\sim 7 \times 10^{14}\,\mathrm{g\,cm^{-3}}$.

Chapter 8

Solving for the Cooling Curves; `cooling_models`

With the time-independent neutron star profiles dealt with, the last remaining problem is to solve for the cooling curves. As discussed in section 4.3, neutron stars may be approximated as isothermal due to the high thermal conductivity of the degenerate matter. Thus, before developing the heavier numerical methods for cooling of inhomogeneous profiled objects, we experimented with a basic model to solve for isothermal stars following section 4.1. This proved beneficial, being a much simpler numerical implementation to get running in the first place, and more importantly providing analytical approximations to test our solutions. Section 8.2 briefly summarize this simplified cooling model for pure neutron compositions, before the full problem is treated in section 8.3. As mentioned, this module is implemented in the same type of structure as `ns_models`, where all common operations are collected into the underlying `solver_cooling` class. Built upon this are the individual models, defining the RHS of the cooling equation and heat capacity, as well as the relevant cooling and heating mechanisms present by summing the contribution from various emissivities. As we'll try to point out along the way, there are a few more «nobs» to tune and adjust in terms of parameters and accuracy in the cooling calculations than in the structural part. As such we'll lay out the scaling in detail for the homogeneous problem, and avoid the clutter of scales involved in the profiled cooling – found in a similar fashion.

8.1 Common Features

The cooling models are implemented to require as input an *instance* of a neutron star structure model, with at least one solution precomputed.[1] Preferably the input instance is already solved over a wide range of initial densities, having the total mass parameterized in terms of core density as we discussed in section 6.1. To study the cooling process of a neutron star with a specific mass, the core density corresponding to the desired mass for the given structure model is found. This density is then used as input to the structure solver to produce the actual structure profiles to be used in the cooling calculation.

For scaling we found it most convenient to rebase each scaling coefficient from the structural solution to better fit with the relevant equations for cooling, following the normalization implied by the emissivity equations:

$$\begin{aligned} M^o &= 1\, M_\odot, \qquad & R^o &= 10\,\mathrm{km} \\ \rho^o &= 1\, \rho_{\mathrm{nuc}}, \qquad & T^o &= 10^9\,\mathrm{K}. \end{aligned} \tag{8.1}$$

Working in a different scale than in the structural problem, we first extract the full profiled quantities from the newly obtained solution with the desired mass, convert them to cgs-units, before rescaling them according to 8.1. All of this of course is dealt with in the `Scales` class.

As the cooling equation, in both the homogeneous and profiled case, are indeed initial value problems,[2] we just continued our use of SciPy's `solve_ivp`. One important distinction between the cooling and structural problem is that the heat transport equation is a diffusion equation – requiring an *implicit* integration method to be numerically stable. Fortunately, `solve_ivp` offers three different implicit methods, of which the *'BDF'* method was chosen; an implicit multi-step method of variable order from one to five based on backward differentiation, with accuracy determined by the mentioned absolute and relative error tolerances. Not yet optimized for speed, we found the same set of tolerances as in the structural part to produce consistent results for all our models

$$\Delta_a = \Delta_r = 1 \times 10^{-6}, \tag{8.2}$$

which also may be given as input parameters, as well as the integration method.

[1] Instance being a common phrase in object oriented programming, refers to one particular occurrence of a class. The instance is initialized following specifications given by the type of class it is representing, and can then be treated as a type of «object» within the context of the computer programming.

[2] The «value» being a collection of points in the inhomogeneous case, the whole temperature profile.

8.2 Isothermal Cooling

8.2.1 Analytical Approximations

To find some simplified analytic solutions to compare our eventual numerical results against [cf. section 8.2 and fig. 8.1], we assume an canonical isothermal neutron star of homogeneous density $\bar{\rho} = \rho_{\text{nuc}}$, mass $M = 1M_\odot$ and radius $R = 10\,\text{km}$.[3] We can then write the total heat capacity and the luminosity for (Urca) neutrinos and photons on approximate forms to emphasize the temperature dependencies as

$$C_v = CT, \qquad C \sim 10^{30}\,\text{erg}\,\text{K}^{-2} \tag{8.3}$$

$$L_\nu = \nu T^8, \qquad \nu = 5.3 \times 10^{-33}\,\text{erg}\,\text{K}^{-8}\,\text{s}^{-1} \tag{8.4}$$

$$L_\gamma = \gamma T_s^4 \approx \gamma T^{2.2}, \qquad \gamma = 7.13 \times 10^{8}\,\text{erg}\,\text{K}^{-4}\,\text{s}^{-1}, \tag{8.5}$$

where we have grouped the non-temperature terms into constants, and used the rough $T_s \sim T_b^{0.55}$ relationship. We can then find solutions to the cooling equation [cf. eq. (4.4)] in the two regimes of the cooling process dominated by neutrinos and photons respectively. First, at high temperatures, we can neglect L_γ, and find

$$\frac{dT}{dt} = -\frac{L_\nu}{C_v} = -\frac{\nu T^7}{C}. \tag{8.6}$$

We can solve this simple separable equation by integrating from an initial temperature T_i to a final T_f, over the time period $\Delta t = t_f - t_i$, giving

$$\left(\frac{1}{T_f^6} - \frac{1}{T_i^6}\right) = \frac{6\nu}{C}\Delta t. \tag{8.7}$$

From here we have an equation giving us the time it takes to cool from T_f to T_i, which we can test against our results [cf. fig. 8.1]. We can also approximate the slope of temperature as a function of time, by assuming $T_f \ll T_i$ and taking $t_i = 0$, which gives

$$\frac{1}{T_f^6} \approx \frac{6\nu}{C}t \quad \Rightarrow \quad T_f \approx \left(\frac{C}{6\nu}\right)^{1/6} t^{\,-1/6}, \tag{8.8}$$

suggesting a $T \propto t^{\,-1/6}$ power law.

With the same procedure one can find the approximate solution in the photon dominated regime, albeit a bit more troublesome for the full T_b-T_s relationship we are using in our code. Instead we've compared our results in this regime to those obtained in other sources, which we'll come back to in part III. However, it's simple to find the

[3] The resulting expression would be the same whatever mass and radius we choose, as long as the density is homogeneous.

temperature where photon cooling should start to dominate, by equalling L_γ and L_ν at the temperature T_{eq}

$$\gamma T_{\mathrm{eq}}^{2.2} = \nu T_{\mathrm{eq}}^{8} \tag{8.9}$$

$$\Rightarrow T_{\mathrm{eq}} = \left(\frac{\gamma}{\nu}\right)^{\frac{1}{5.8}} \gtrsim 10^7\,\mathrm{K}. \tag{8.10}$$

8.2.2 Numerical Implementaion

To study isothermal cooling consistently, we found ourselves in need of a neutron star model with constant density, easily implemented using the polytropic formula as described in section 7.3. For a constant density interior, the luminosities and heat capacity are given by eqs. (4.5), (4.19) and (4.20).

With the new base for scaling defined in 8.1, the rest of the scaling coefficients are again determined to remove physical constants wherever possible. For the simple isothermal cooling equation this was done as

$$C_v^o = \frac{M^o k_{\mathrm{B}}^2 T^o}{m_n^2 c^2} = 1.503 \times 10^{37}\,\mathrm{erg\,K^{-1}} \tag{8.11}$$

$$t^o = \frac{C_v^o T^o}{L^o} = 2.836 \times 10^6\,\mathrm{s} \tag{8.12}$$

$$g_s^o = \frac{GM^o}{[R^o]^2} = 1.327 \times 10^{14}\,\mathrm{cm\,s^{-2}} \tag{8.13}$$

$$L^o = 5.3 \times 10^{39}\,\mathrm{erg\,s^{-1}}. \tag{8.14}$$

Then, the dimensionless quantities are found as

$$L_\nu^{\mathrm{Urca}\prime} = M' \left[\rho'\right]^{-1/3} \left[T'\right]^8 \tag{8.15}$$

$$L_\gamma{}' = \frac{4\pi [R^o]^2 \sigma_{\mathrm{SB}} [T^o]^4}{L^o} \left[R'\right]^2 \left[T_s'\right]^4 \tag{8.16}$$

$$= 1.345 \times 10^5 \cdot \left[R'\right]^2 \left[T_s'\right]^4 \tag{8.17}$$

$$C_v' = \frac{\pi^2 \sqrt{x_n^2 + 1}}{x_n^2} M' T', \tag{8.18}$$

with the dimensionless surface temperature as

$$T_s' = \left(\frac{0.87 \times 10^6\,\mathrm{K}}{T^o}\right)\left(\frac{g_s^o}{10^{14}\,\mathrm{cm\,s^{-2}}}\right)^{1/4}\left(\frac{T^o}{10^8\,\mathrm{K}}\right)^{0.55}\left[g_s'\right]^{1/4}\left[T'\right]^{0.55}$$
$$= 0.0033 \cdot \left[g_s'\right]^{1/4}\left[T'\right]^{0.55}. \tag{8.19}$$

With a constant mass density follows a constant number density and relativity parameter, found by eqs. (3.11) and (3.12) using the rest mass density in cgs units. Given

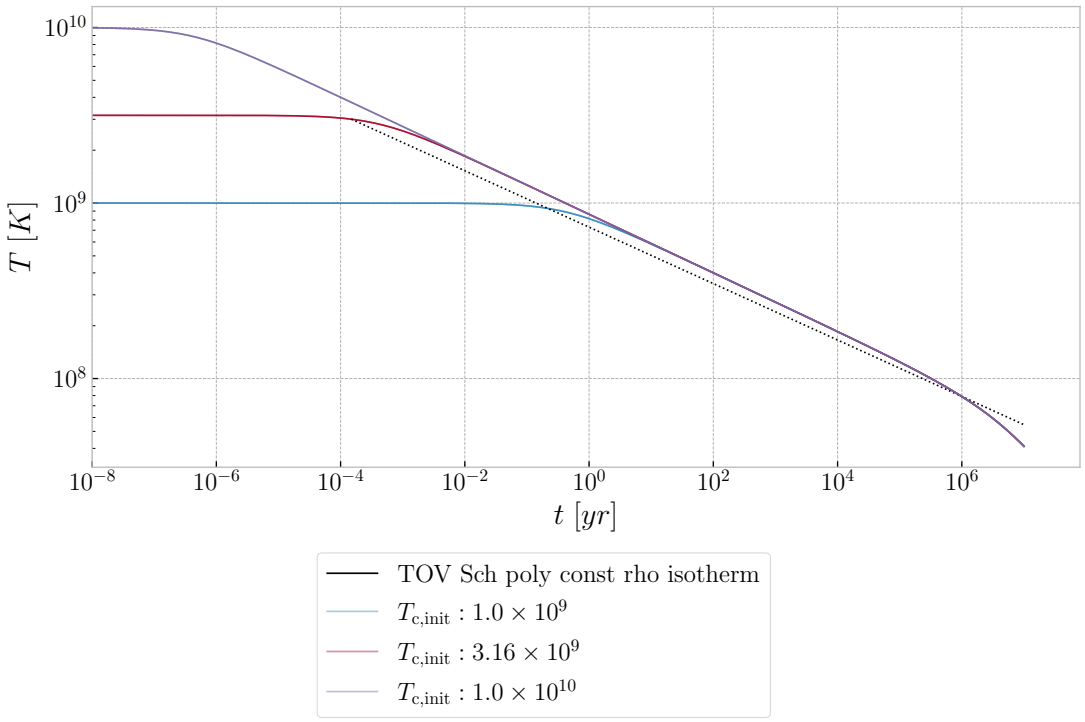

Figure 8.1: Demonstration of cooling curves for isothermal bodies. Three different initial temperatures are shown, which all converge within the first year. The slope of the curves follows relatively close to the analytic approximation of the cooling we expect from the modified Urca rate, shown in the dotted black line. After $t = 10^6$ yr, the contribution from photons start dominating the cooling.

an initial temperature, the cooling curves are found by integrating the dimensionless cooling equation until some input end time is reached[4]

$$\frac{dT'}{dt'} = -\frac{L_\nu^{\mathrm{Urca}\prime} + L_\gamma{}'}{C_v'}. \tag{8.20}$$

In fig. 8.1 we see an example of three different obtained cooling curves for a uniform neutron star, with three different initial temperatures between 10^9 and 10^{10} K. As we can see, the assigned initial temperature becomes irrelevant within the first year of integration as each curve converges to the equilibrium solution for the given model. The analytical approximation from eq. (8.7) is included as the black dotted line in the figure. As we can see, the numerical solution follows closely the slope suggested by the analytical result. As we are also including photons, our solution is found to have a slightly steeper slope, and when the temperature drops to a few 10^7 K the cooling becomes dominated by photon cooling.

[4]Or until the temperature drops below an input tolerance value, similar to that of the input surface density value for the structure.

8.3 Full Profiled Cooling

As mentioned in section 8.1, the full profiled cooling is by far the most complicated system we've modeled. Much of the theory describing the physics we are modeling is based on Page et al. (2004), who also has written a similar code for calculating cooling curves, which we have used as inspiration. By now we hope the techniques employed for scaling have been made clear, and avoid overloading this section with scaled equations. Instead we'll refer to the full physical equations as listed in section 4.3.1, but all the numerical solving is still done on the scaled equations. We'll also just use the terms temperature and luminosity, instead of explicitly specifying that the quantities are *redshifted* throughout. To emphasize the difference between the boundary temperature and the effective surface temperature, we'll use the term *boundary* (subscript b) to describe quantities as they are at the last point on our radial profiles, while *surface* (subscript s) indicate quantities related to the envelope model. At initialization of the model, three parameters may be given as input, which we'll encounter in the following sections.[5] The first is the number of grid points to be used in the radial profile, N. We'll also need to specify an initial temperature profile «type» and boundary value. The last is the local dark matter density $\mathcal{A}_{\text{WIMP}}$, determining the heating rate.

8.3.1 Descretization of the Radial Profile

The full profiled cooling may be described as a series of smaller, connected isothermal objects, i.e. uniform *shells*, as described in section 4.3. From eq. (4.43) we can see how the profiled cooling is a kind of generalization of the isothermal problem already described above, using the volume-dependent emissivities and specific heat capacity instead of the corresponding uniform quantities. In addition we have to account for the conductive term, transporting energy between connected neighboring shells expressed through the luminosity gradient. Remember, the gradients of temperature and luminosity in this context are taken with respect to the baryon number density da, not the radius dr. The luminosity and temperature are closely related by eqs. (4.42) and (4.43), the luminosity determined by the temperature gradient, and the time evolution of the temperature in turn determined by the luminosity gradient. Therefore, to model these shells numerically, we discretized the radial profile of the star into a linearly spaced grid of points $j = [0, 1, 2, 3, \ldots, N-1]$. That is N number of points, where N *must* be an even number, and the boundary $j = b$ is at $N-1$. N may be given as input to the cooling model, acting as one of the «nobs» we can increase to improve accuracy.[6] For the results presented in this thesis we used $N = 200$. The individual shells are then defined between the even-numbered j, with thickness equal the radial distance between these points. The temperature is defined in the middle of each shell, on the odd-numbered grid points, whereas the luminosity, being interpreted as an energy flux between shells,

[5] The parameters turn to default values if not provided

[6] However, also increase computation time significantly in the current implementation.

is defined on the even-numbered points. Following the analogy to isothermal cooling, the temperature can be thought of as the average temperature of the shell, with the luminosity defined at the boundaries.

8.3.2 Setup from Structure

To define the initial conditions to be used for the cooling calculation we first need some quantities from the structure model. As discussed in section 8.1, a new structure solution is found with a desired total mass before the obtained profiles are extracted to fit in the cooling grid.[7] The desired mass, or «target» mass, is also one of the possible input parameters to give the solver, making it easy to compare two cooling curve solutions of the same model but with varied mass and radius. The extracted quantities include the metric coefficients and surface gravity acceleration; the mass, radius, pressure and density; and the baryon number density and relativity parameter.[8] Then the infinitesimal baryon number da_j is found following eq. (4.39), where $dr = r_j - r_{j-1}$ is taken to be the radial equally spaced distance between grid points. All these quantities are defined on every cooling grid point j.

8.3.3 Initial Conditions for Cooling

In chapter 4 we briefly mentioned that, within reasonable limits, we are free to choose how the initial physical temperature profile is assigned. We'll come back to this statement in section 9.3, for now we describe how these profiles are determined. When solving with an instance of the cooling model, not only the desired total mass of the star may be given as input, but also a specific type of initial temperature profile and initial boundary temperature $T_{b,init}$. The temperature profiles are constructed to have precisely the given temperature at the boundary, with the interior shape determined according to the specified profile type. These profiles have been given descriptive names, and are defined as follows

- **Isotherm** – the simplest profile. As the name suggests, this profile is defined to be isotherm from the start. This profile type may be useful if we're only interested in the cooling process after the neutron star has become isothermal.
- **Quadratic** – a profile designed to decrease roughly proportional to the inverse square of the radial distance from the core, being equal $T_{b,init}$ at the boundary.

[7] If the target total mass is higher than the achievable maximum mass of the model, the solver will produce a warning message and default to use the solution corresponding to maximum mass.

[8] Extracting the baryon number density and relativity parameter is slightly more complicated in the presence of multiple particle species. We'll consider the pure neutron models here, which after all includes the most realistic QMC EoS, and summarize the changes required to include protons and electrons in section 8.3.5.

This is thought to give one representation of a possible initial temperature profile with a hot core and cooler surface, appropriate for the cooling process we are looking at ($T \lesssim 10^9\,\mathrm{K}$). Specifically, a profile of $N/2$ equally spaced numbers between 0 and 0.5, called it q, is used to give the initial temperature profile as $T_i = T_{b,init} \cdot \big(2.34 + 1/\big(q^2 - 1\big)\big)$.

- **Ideal gas-like** – a profile inspired by the ideal gas law. The temperature profile resulting from the profiles for pressure and number density is found as $T = P/(nk_\mathrm{B})$, and then adjusted to be equal $T_{b,init}$ at the boundary by multiplying the hole profile by a constant. Again thought to represent a profile with some relevant physical reasoning behind it. Compared to the 'quadratic' profile, this one gives an exaggerated initial temperature gradient.

Again, from Page et al. (2004, 2006), we knew these profiles should not be too important in the long term cooling process of neutron stars. And so the exact quantitative shape of the profiles is found through simple experimentation. Alongside the initial temperature profile, which is stored separately for later comparison, we initialize the arrays for the temperature and luminosity as well as their gradients.

8.3.4 Integrating the Temperature Time Derivative

To follow the process of solving the coupled set of equations in eqs. (4.42) and (4.43), we have to think along two discretized numerical grids. The first being the radial profile of the star divided into shells, where the actual structure of the star is static, but we assign the matter a physical temperature profile. This temperature profile is in turn changing in time, making time the second «grid». With `solve_ivp` we are easily able to treat the time evolution of the whole temperature profile, as long as we specify the exact value of all the quantities in eq. (4.43) at each individual grid point. We therefore used the same approach as for the homogeneous cooling, but we have to find the total emissivity, the heat capacity, and the luminosity gradient at every grid point, for every time step of integration. Naturally, this is the most demanding computational task of the framework, and is a bottleneck for computation time.

As mentioned, the temperature and luminosity are only defined on alternating grid points, even for the temperature and odd for luminosity. Thus, there are only $N/2$ grid points for each of these quantities. And so the part solving the time evolution of the temperature in each shell is only treating the odd-numbered grid points. This means, for every time step,[9] we have to approximate the luminosity gradient at the odd-numbered grid points. This is done by iterating over the even-numbered grid points to approximate the temperature gradient giving the actual luminosity, which finally gives the luminosity gradient at odd-numbered grid points. We do this in a single

[9] Following the *implicit* backwards differentiation scheme.

iteration over $j = [2, 4, \ldots, N-2]$, following the schematic order outlined below where the subscripts indicate grid point number. The endpoints are treated with boundary conditions following Thorne (1977); Page et al. (2004). To get the luminosity gradient at the last temperature grid point, $N-1$, we have to use the envelope model to find the luminosity of the surface – not a part of the cooling grid. This is actually where the whole photon contribution is treated, which only occurs at the surface as discussed in section 4.2.2. Again note, in the code, everything is scaled to dimensionless equations, with numerical factors grouped into single factors to reduce the number of FLOPS as we did for the equations of state.

- `for j = 0:`
  As we have no temperature defined interior this point we may set the core luminosity to zero $\mathcal{L}_0 = 0$. An alternative is to use the total luminosity of a homogeneous core, giving $\mathcal{L}_0 = 4\pi r_0^2 \sigma_{\rm SB} \mathcal{T}_1^4$. We've implemented both to compare the effects, and didn't observe any difference in the resulting cooling curves between the two choices. Note we have to use the temperature defined at $j = 1$.

- `for j = [2,4,...,N-2]:`
  Approximate the temperature gradient and the average temperature, to find the thermal conductivity [cf. eq. (4.34)] and luminosity [cf. eq. (4.42)] at j, before approximating the luminosity gradient at $j-1$:

$$\left.\frac{d\mathcal{T}}{da}\right|_j = \frac{\mathcal{T}_{j+1} - \mathcal{T}_{j-1}}{da_{j-1} + da_j} \tag{8.21}$$

$$\bar{\mathcal{T}}_j = \frac{(\mathcal{T}_{j+1} + \mathcal{T}_{j-1})}{2} \tag{8.22}$$

$$\text{which gives} \quad \lambda_{th,j} = \lambda_{th,j}(\bar{\mathcal{T}}_j) \quad \text{and} \quad \mathcal{L}_j = \mathcal{L}_j\left(\left.\frac{d\mathcal{T}}{da}\right|_j, \lambda_{th,j}\right)$$

$$\text{then} \quad \left.\frac{d\mathcal{L}}{da}\right|_{j-1} = \frac{\mathcal{L}_j - \mathcal{L}_{j-2}}{da_{j-2} + da_{j-1}} \tag{8.23}$$

- `for j = N-1:`
  To approximate the luminosity gradient at the boundary like 8.23, we need the surface luminosity. The effective surface temperature $\mathcal{T}_s = \mathcal{T}_s(\mathcal{T}_b)$ is found using the envelope [cf. eq. (4.22)], which gives the surface luminosity as $\mathcal{L}_s = 4\pi R^2 \sigma_{\rm SB} \mathcal{T}_s^4$, where $R = r_b$ is the radius at the boundary. Then the luminosity gradient at the boundary is found as

$$\left.\frac{d\mathcal{L}}{da}\right|_{N-1} = \frac{\mathcal{L}_s - \mathcal{L}_{N-2}}{da_{N-2} + da_{N-1}}. \tag{8.24}$$

We also get the specific heat capacity and emissivities on the odd-numbered grid points using the proper temperature profile, found from the inverse transformation

in eq. (4.38).[10] Then, the time evolution of the temperature in each shell is determined by solving cooling equation for odd numbered j

$$\left.\frac{d\mathcal{T}}{dt}\right|_j = -\left((\epsilon_c - \epsilon_h)_j \mathcal{R}_j^2 - n_{B,j} \left.\frac{d\mathcal{L}}{da}\right|_j\right) \frac{1}{c_{v,j}}. \tag{8.25}$$

8.3.5 Including Additional Particle Species

So far in this section we've discussed the model assuming only neutrons are present in the gas. To include other particles we have to account for a few adjustments to the equations in the model, serving as a good example to demonstrate the ease of extending the framework. Following the same logic and structure as for the `ns_models` module, by either inheriting from another model class as we'll demonstrate for the addition of protons and electrons here, or by defining whole new classes inheriting the underlying solver, all we have to do is define the new desired behavior.

The only change we are making to the model here is the addition of protons and electrons. Thus, we need to change the specific heat capacity and include protons in the baryon number density. The rest of the implementation stays the same, so we only need to implement our new cooling class as a *child* of the already developed class we have discussed so far regarding neutrons.[11] Then include the number density and relativity parameter of each particle, and overwrite the method that calculates the specific heat. Following the arguments from sections 3.3 and 4.1, we find the total specific heat by summing each particle's contribution defined in eq. (4.29)

$$c_{v,\mathrm{tot}} = \sum_{i=n,p,e} c_{v,i}, \tag{8.26}$$

in a similar fashion as sources like Page et al. (2004, 2006)

This same process of modifying and expanding upon the base cooling models we have defined is easy to extend to more and exciting physics and particle species, varied envelope models, and as many cooling and heating mechanisms we want – as long as we can express the resulting specific heat, and (cooling and heating) emissivities along the radial profile.

[10] The quantities are found with the temperature profile not redshifted, as the adjustments from general relativity are dealt with in eq. (8.25).

[11] The new class `profiled_npe` is defined to inherit from the `profiled_n` class instead of the underlining solver-class – copying every method of the neutron only model including the emissivities.

Part III

Results and Conclusion, A Modular Neutron Star Calculator

Chapter 9

Our Numerical Framework

Throughout part II we tried to explain the numerical methods and techniques applied to solve the relevant equations describing each of the three pieces of the puzzle that is neutron star structure and cooling. Along the way we've also argued for the stability, clear structure, and conciseness of the implementation while facilitating flexibility for future improvements and expansion, as well as the ease of using the framework. In this chapter we try to justify this latter statement by giving an example of its use in section 9.1. Here we showcase the actual code as it is used to produce some of the first results and figures for structure and cooling, which we then discuss in sections 9.2 and 9.3 based on the theory presented in part I.

9.1 How Everything Works Together

As we've seen, the code consists of three main modules working together, one for every subject in chapters 2 to 4. Each of these modules is a collection of classes where the different desired behavior is defined, with common behavior inherited from underlying solver-classes. Neutron star models are constructed by combining these modules, following the schematic in fig. 9.1. Here we've tried to emphasize the main objective of each module, and how they are all connected through the various utility classes. The three modules doing the heavy lifting all follow the same type of code structure and connection to the utilities, to make it clear and easy to expand and work with. Especially the `eos_models` module are a candidate for future expansion to include more exiting physics and particle species, as we discussed in chapters 3 and 7. This is also true for the `cooling_models`, which we'll get back to in section 11.1 when we discuss some future prospects.

Figure 9.1 also mention the `Plotter` module as one of the included utilities. This class is used to create all of the graphs in this thesis. The plotter was continuously

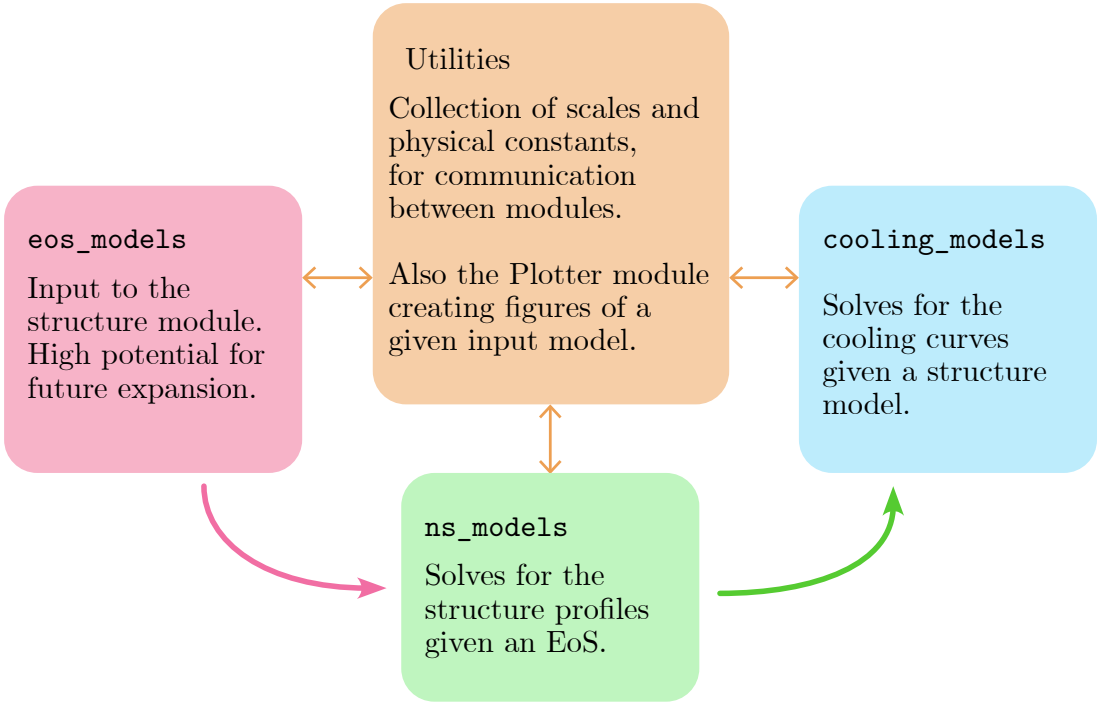

Figure 9.1: Code structure schematic of the framework, illustrating how the individual modules are dependent on each other, interconnected with the utility classes. Figure credit: Renate Røsæg.

developed alongside the gradual process of this project to consistently compare and test the result of the different models while implementing them. It has served faithfully for this purpose, but some customization has been done to produce the figures showcasing individual special features. An honorable mention that did not make the cut,[1] are time evolution animations of the temperature and luminosity profiles, as well as their gradients, who proved very useful for debugging the profiled cooling process.

To demonstrate the use of the framework, lets «build» some neutron stars! The following are some of the actual lines of code used to produce the figures we'll see in this chapter, albeit a bit taken out of context for the sake of demonstration. As repeated throughout part II, we are solving over a range of initial density values to create the parameterized total mass and radius relations. We'll come back to this in section 11.1, but we've left out some technical syntax used to group all these models into dictionaries to streamline the looping. Nevertheless, the code listed here is good to go, and would produce *one* solution for each model. We've tried to emphasize the most important input parameters that may be given to each part. Note however that there are more possibilities provided, most of which have been described in part II.

[1] Animations being kind of boring on paper, we didn't prioritize making them informative for an «outside observer» . . . i.e. someone unfamiliar with the process.

First of all, let's import the modules and initialize three neutron star instances. To showcase the use, we create one star with the Fermi npe EoS (the one in the following figures), and one with the QMC4 EoS [cf. chapter 10], both with the TOV equations under Schwarzschild scaling. In addition we create a Newtonian neutron star with the polytropic EoS in the non-relativistic limit, again for demonstration purposes. Each model in `ns_models` takes as input a class (uninitialized) of the desired EoS along with accompanied keyword parameters, to initialize the structural part with the assigned EoS at the same time, connected through the `Scales` class:

```
import ns_models, eos_models, cooling_models, utils

NS_npe = ns_models.TOV_Sch(eos_models.Fermi_npe)
NS_QMC4 = ns_models.TOV_Sch(eos_models.QMC, hamiltonian=4)
NS_Newt = ns_models.Newton_Sch(eos_models.Polytropic, rel=False)
```

We can then «set the boundary conditions», following section 6.1, by giving the rest mass density $\rho_{0,c} = 10^{15}$ in units of $\mathrm{g\,cm^{-3}}$ as input, and solve each model until the desired outer boundary rest mass density is reached, following section 6.3:

```
NS_npe.set_boundary_conditions(rho_core=1e15)
NS_npe.solve(rho_tol=1e10)
```

This syntax is the same for every class in `ns_models`, and we therefore skip the lines regarding the other two models. As mentioned, all unit handling and scaling are done prior and post calculations by `Scales`. Handling of the solutions is done at the end of the `solve` method, as described at the end of section 6.3.

With the structure models precomputed, given we've done the above solving over a range of density values,[2] we are ready to cool them down. For this, we'll demonstrate the use of the profiled cooling models developed for a pure neutron gas, and the one including protons and electrons, appropriate for the QMC4 and Fermi npe EoS respectively. Here we are free to give the number of radial cooling grid points and the type of initial temperature profile as input,[3] as well as specifying the desired density of dark matter particles $\mathcal{A}_{\mathrm{WIMP}}$ determining the heating rate. Giving $\mathcal{A}_{\mathrm{WIMP}} = 0$ will turn off the effect of heating entirely. The only required input is the actual structure model to be used in each case, the other parameters taking default values if not specified.

```
Cool_npe = cooling_models.Profiled_cooling_npe(NS_npe,A_WIMP=0,\
                              T_init_profile="quadratic")
Cool_QMC4 = cooling_models.Profiled_cooling(NS_QMC4,A_WIMP=10,\
                              T_init_profile="ideal gas-like")
```

[2] If this is not the case, and we only have the one solution found with the input density from above, the cooling model will just use the one solution it finds available and produce a warning message.

[3] To avoid over cluttering the code listing, we neglect to specify the number of grid points which then defaults to 200.

The boundary temperature value and target mass may be given as input to the `solve` method of the cooling models for each solution. We're also free to adjust some other parameters like integration accuracy and the desired end time. However, if the temperature drops below 10^3 K we end the integration early. As we have not included any heating in the npe model, the temperature should reach this tolerance value and end the integration at some point, so we just set a high end time value. As we'll see in fig. 9.2, neutron stars with the Fermi npe EoS are not able to reach very high total masses. For demonstration purposes we'll therefore ask the cooling model to find a structural solution with an unobtainable target mass, let's say $5M_\odot$, which will print a warning message to the terminal and inform of the maximum total mass it defaulted to use instead [cf. section 8.3.2]. We'll also specify a boundary initial temperature of $T_{b,init} = 10^{10}$ in units of K, resulting in a core initial temperature of $T_{c,init} = 1.34 \times 10^{10}$ K using the quadratic temperature profile. For the model with the QMC4 EoS we give a more reasonable target mass, and a lower initial temperature. We expect the heating rate to stabilize the temperature at around $t \sim 10^7$ years, making integrating much further than this uninteresting, so we end the integration at $t = 10^8$ yr.[4]

```
Cool_npe.solve(T_surface=1e10, t_end_yr=1e9, target_tol_mass=5)
Cool_QMC4.solve(T_surface=1e9, t_end_yr=1e8, target_tol_mass=1.4)
```

The last step of the process is to produce figures of our newfound solutions, for which we use an instance of the `Plotter` class briefly introduced earlier.[5] As mentioned, in creating the figures included in this thesis we did some minor adjustments to each plot to better display the relevant details. To showcase how the plotter is intended to be used to compare different models at once, we instead show the simplest way to produce each type of figure available with *both* the QMC4 and npe solutions plotted in each figure, with model-specific details included in the legends. To do this the plotter takes as input a list of model instances appropriate to each type of plot: one full figure of all main structure variables, as well as a figure of the metric coefficients similar to figs. 2.1 and 2.2; one figure for the parameterized total mass and radius like in fig. 7.1; and finally one figure of the cooling curves like in fig. 8.1.

```
plotter = utils.Plotter()
plotter.plot_1D_multi_models([NS_npe,NS_QMC4])
plotter.plot_max_mass_multi_models([NS_npe,NS_QMC4])
plotter.plot_cooling_fig([Cool_npe,Cool_QMC4])
```

[4] We'll see examples of this in chapter 10, albeit for other QMC models.

[5] The plotter does take some input like data paths and filenames for saving of figures. We'll skip that for this demonstration.

Computation Time

As mentioned, solving for the cooling curves is the bottleneck for computation time, although it's not too bad. This entire project has been run on a standard MacBook Pro from 2017, with a dual-core i5 processor and 8 GB of ram. We'll discuss some possibilities for optimizing run time in section 11.1, but `solve_ivp` is heavily optimized already and we expect the code to scale rather well to more powerful computers.

We'll report on the involved time for a complete solution of the most demanding model regarding computation time, the Fermi npe EoS with npe profiled cooling. Solving for 100 core densities logarithmically spaced from 10^{13} to $10^{16}\,\mathrm{g\,cm^{-3}}$ is done in about 11 seconds. That includes the time for all initialization, scaling, solving, storing the full profiles, create the parameterized total mass curves, and then solving one more time to obtain a solution with profiles corresponding to a specific total mass.[6] From there, the cooling calculation time is dependent on the input of $\mathcal{A}_{\mathrm{WIMP}}$ as described for the two examples above. The choice of temperature profile and initial boundary temperature affects the required step length at early times, increasing the computation time slightly.[7] For a quadratic temperature profile and $T_{b,init} = 10^{10}\,\mathrm{K}$ as in the example, the integration is terminated by reaching the tolerance at $T \simeq 10^3\,\mathrm{K}$ after about 55 seconds of integration, that is at end time $t \simeq 10^8\,\mathrm{yr}$.

9.2 First Structure Results

With our framework at hand, there are a swell of possible results to inspect – some of which we have already seen throughout parts I and II. These have been somewhat intermediate results, in the sense that we have looked at some simplified approximations and partial results we've found during the development of the whole framework, and aimed to provide a visual guide to the reader. Here we try to summarize the results from these various approximations, and what we've learned from studying them. We'll neglect the Newtonian models for now, as they fall short to properly describe the gravitational effects in neutron stars.

In this chapter we've chosen to highlight and discuss the results obtained from the different types of equations of state from sections 3.2 and 3.3, the Fermi equations of state, for which we have laid out all the theory required to discuss them properly. We find all of the results to be consistent with theory and figures from Shapiro and Teukolsky (1983), although the source is outdated in some regards. It should not matter too much for the results from the Fermi EoS, as most of the basic theory for completely degenerate matter has remained unchanged since Chandrasekhar (1939). However, some of the numerical values for physical constants and particle masses have

[6] So technically, we have 101 solutions!

[7] Using the isothermal initial temperature speeds up the computation at early times!

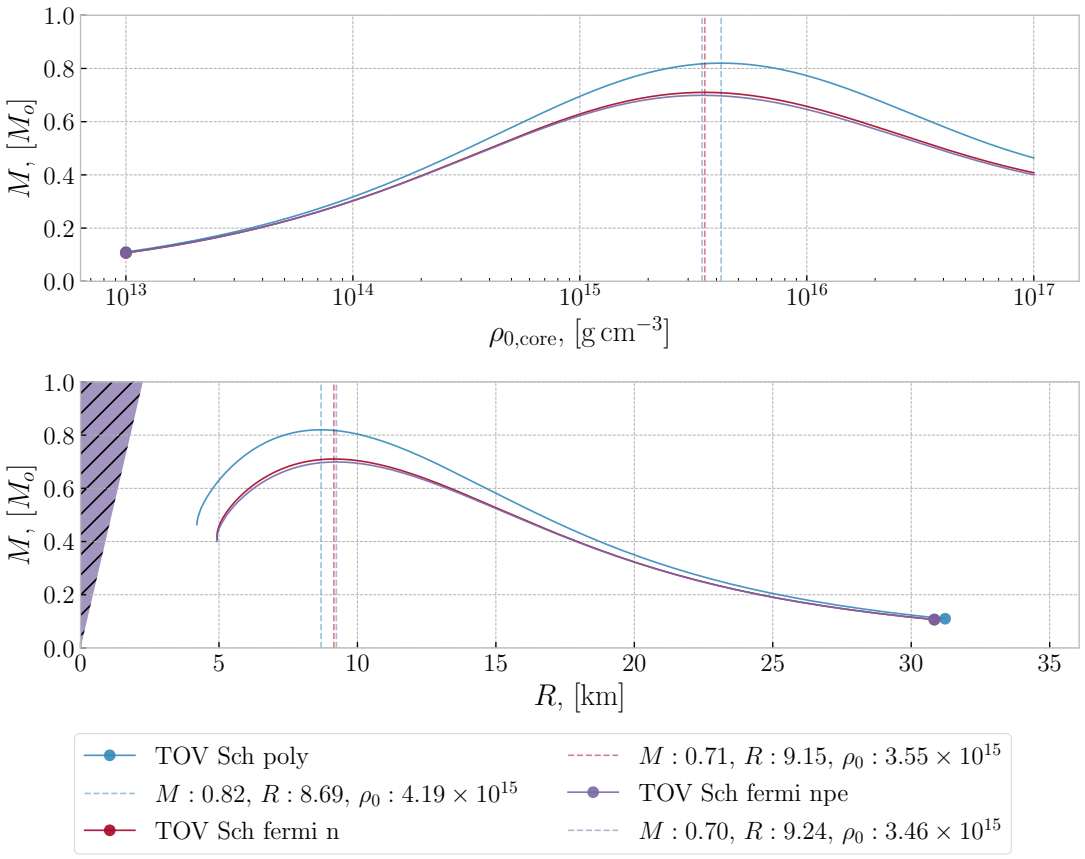

Figure 9.2: Parameterized total mass and radius for the Fermi EoS (n and npe) and the non-relativistic polytropic EoS. Maximum mass, with corresponding radius and core rest mass density in vertical dashed lines.

been updated since 1983, and there are some significant jumps in the theory and results presented in Shapiro and Teukolsky, both of which are not described. As such, we have to fill in some missing connections in the comparison.

In fig. 9.2 is the resulting total mass and radius parameterized in terms of the input core rest mass density. As this initial condition is the only variable in determining the structure profiles, we can produce this simple figure to convey most of the relevant results from these models.[8] The dashed vertical lines indicate the maximum mass achievable with each EoS. The actual values for max mass with corresponding radius and density are included in the legend. The purple dashed field in the lower figure encapsulates configurations that are forbidden following Buchdahl's theorem for the maximum compactness of objects in general relativity. That is objects where the proportion of total mass to radius is $(M/R) \leq 4/9$ (Shapiro and Teukolsky, 1983).

[8]Note the dramatic difference from the Newtonian picture in fig. 7.1, with no maximum in sight.

Table 9.1: Max mass solutions with the Fermi EoS, including the non-relativistic polytropic approximation and the original result of OV.

EoS	Max Mass	Radius	Core Density
Polytropic	$0.82\,\mathrm{M}_\odot$	8.69 km	$4.19 \times 10^{15}\,\mathrm{g\,cm^{-3}}$
Fermi n	$0.71\,\mathrm{M}_\odot$	9.15 km	$3.55 \times 10^{15}\,\mathrm{g\,cm^{-3}}$
Fermi npe	$0.70\,\mathrm{M}_\odot$	9.21 km	$3.49 \times 10^{15}\,\mathrm{g\,cm^{-3}}$
†(OV) Fermi n	$0.7\,\mathrm{M}_\odot$	9.6 km	$5 \times 10^{15}\,\mathrm{g\,cm^{-3}}$
†(OV) Fermi npe	$0.72\,\mathrm{M}_\odot$	8.8 km	$5.8 \times 10^{15}\,\mathrm{g\,cm^{-3}}$

† The original values of Oppenheimer and Volkoff (Shapiro and Teukolsky, 1983).

The dot at the end of each curve points out the lowest density solution, to indicate the reversed relation with density in the lower panel – models with higher initial densities generally results in a lower radius. As we saw in fig. 7.1, the Newtonian structure seemingly has no maximum.[9] The mass just increased while the radius decreased, with increasing initial density. In general relativity this is no longer the case, there exists a maximum at a *finite* value of core density. The exact finite value depends on the equation of state, thought to be at a density where neutrons in the star are becoming relativistic, but not ultra-relativistic.

We see the two models with the full Fermi EoS being very similar, only a slight difference near the maximum mass. The values we found for the max mass and corresponding radius and core density are very similar to those originally obtained by Oppenheimer and Volkoff (OV), in the first numerical treatment of neutron star structures ever done in 1939. There is some confusion regarding the boundary conditions and precise definition and implementation of the EoS employed by OV, which makes further comparison of the discrepancies difficult. Our results for maximum mass along those of OV are listed for comparison in table 9.1. In our case, contrary to OV, the addition of protons and electrons resulted in a slightly lower maximum mass, at a slightly larger radius.

The structure profiles of the two cases are, for the most part, indistinguishable. This is not unexpected, as the contribution to the general structure due to protons and electrons in a β-equilibrium is quite small. As we saw in fig. 7.2, the proton to neutron ratio is relatively low in the density range we are looking at. At the highest, the ratio approaches $1/8$, just as the analytic solution of eq. (7.12) in the high density limit ($x_n \to \infty$). We also find the same minimum value as the analytic solution at the minimum as given by Shapiro and Teukolsky (1983), occurring at the same mass

[9] By solving the briefly mentioned Newtonian polytropes, one can show there should exist a maximum at $M = 5.73\,\mathrm{M}_\odot$ in the limit $\rho_c \to \infty$ (Shapiro and Teukolsky, 1983).

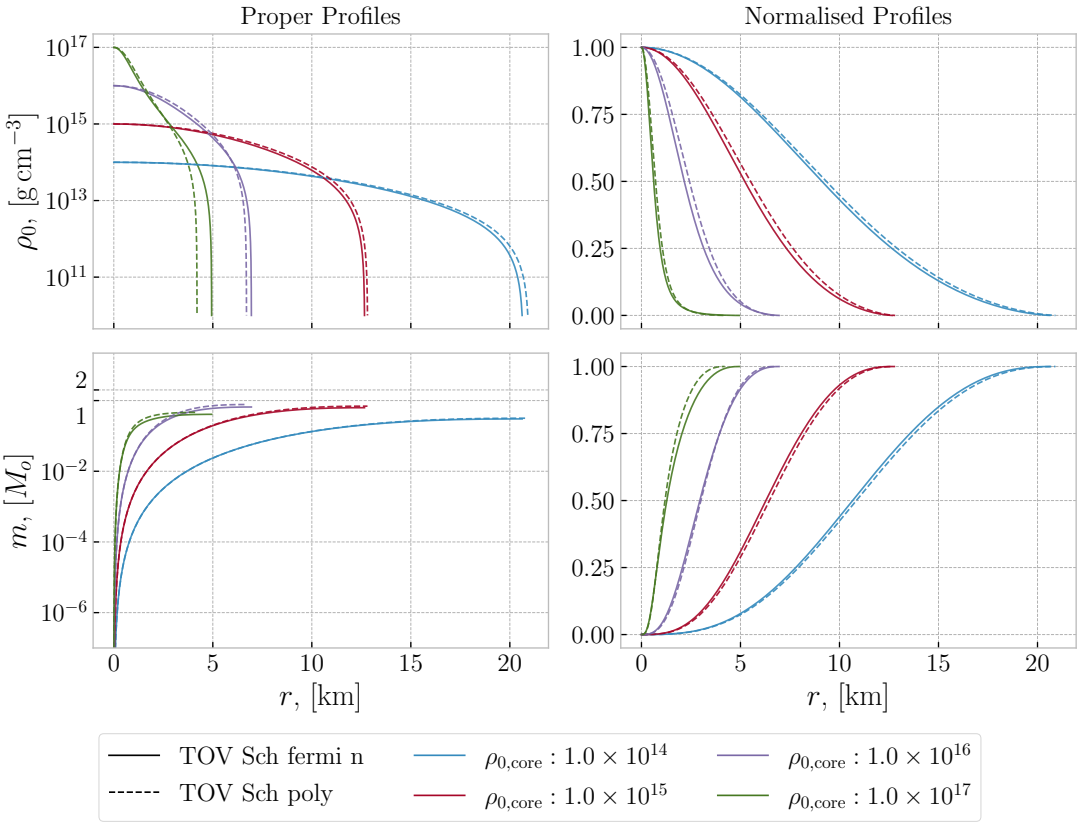

Figure 9.3: Structural mass and density profiles for comparison of the polytropic (dashed) and Fermi npe Eos, with four increasing core densities.

density $\rho_0 \sim 7 \times 10^{11}\,\mathrm{g\,cm^{-3}}$,

$$\left(\frac{n_p}{n_n}\right)_{\text{min}} \equiv \left[\frac{Q + \sqrt{Q^2 - m_e^2}}{m_n}\right]^{3/2} = 1.357 \times 10^{-4}, \tag{9.1}$$

further confirming our implementation. Thus, for all relevant densities ($\rho_0 \geq 10^{10}\,\mathrm{g\,cm^{-3}}$) the number of protons and electrons is low compared to the number of neutrons. This is also consistent with why only neutrons are considered in the QMC EoS, following arguments further justified in Gandolfi (2012). Our found numerical values for the minimum differ slightly from Shapiro and Teukolsky (1983), found with the same analytic expressions, indicating that the values for some physical constants have been updated. This is not surprising, but we have not been able to locate the exact numerical values used by Shapiro and Teukolsky, as they have neglected to list them.

For comparison to the polytropic approximation, we've included the non-relativistic limit (non-rel), applicable for core densities $\ll 6 \times 10^{15}\,\mathrm{g\,cm^{-3}}$. When comparing different equations of state, it's conventional to describe them in terms of the effective

stiffness [cf. section 3.2.1]. We can see how the non-rel approximation accurately fits the Fermi results in the low end of the interval, separating more for higher densities, as expected from fig. 3.2. The polytropic index changes in the two limits, to a lower value in the ultra-relativistic limit (ultra-rel, or just rel). We therefore expect the non-rel polytropic EoS in the high density domain to be too stiff to accurately describe the relationship between pressure and density, giving a higher pressure for a given density.

The maximum mass found for the non-relativistic polytropic EoS is achieved at core rest mass density $\rho_0 = 4.19 \times 10^{15}\,\mathrm{g\,cm^{-3}}$, and is about 15 % higher than those of the Fermi EoS. This is consistent with the polytropic EoS being too stiff. Following Shapiro and Teukolsky (1983), one of the general features observed in simulations is that models constructed with stiffer equations of state tend to have larger maximum mass and radius. We can see why in fig. 9.3, where we compare the density and mass profiles of the polytropic approximation (dashed line) to that of the pure neutron Fermi gas. For *lower* core densities, the red and blue curves, the cumulative mass at any radius is lower in the polytropic approximation than in the Fermi EoS. As such the gravitational potential is not as steep [cf. fig. 2.2], and hence an equally steep pressure and density gradient. Therefore, the boundary is reached at a moderately higher radius. This higher radius, combined with the density taking slightly higher values throughout the profile, results in a higher total mass, despite the lower accumulation rate.

Above the non-relativistic limit, the purple and green curve in fig. 9.3, the approximation is strictly no longer applicable. For these densities the particles are becoming relativistic, meaning their kinetic energy is comparable to, or even exceed, their rest mass. The Fermi EoS should account for this properly near the core, by relaxing the effective stiffness of the EoS to be more comparable to the polytropic EoS as it is in the relativistic limit. When the density drops further out in the profile, the effective stiffness increases, and the appropriate pressure gradient is maintained to define the surface. We know the polytropic formula doesn't include such a varying stiffness, which is evident in the resulting density profiles crossing below the Fermi gas profiles in this inner softer region. To better approximate the high density end of the interval, we have to account for increased relativity in the EoS. We'll look into this, and some encountered problems, in section 9.2.1.

9.2.1 Ultra-Relativistic Problems

Figure 9.4 display the parameterized mass and radius found for a wide range of core densities, now for both the ultra-relativistic and non-relativistic limit (rel poly and poly respectively). The Fermi n solution is also displayed, to show the very high density behavior. Here we see quite dramatically different results obtained from using the ultra-relativistic polytropic equation of state. As we saw in fig. 3.2, the rel poly approximation accurately fits the Fermi EoS at high densities, so what goes wrong here? The found maximum mass $M_{\mathrm{max}} = 2.03\,\mathrm{M}_\odot$ at the core density $\rho_0 = 2.11 \times 10^{17}\,\mathrm{g\,cm^{-3}}$ is well

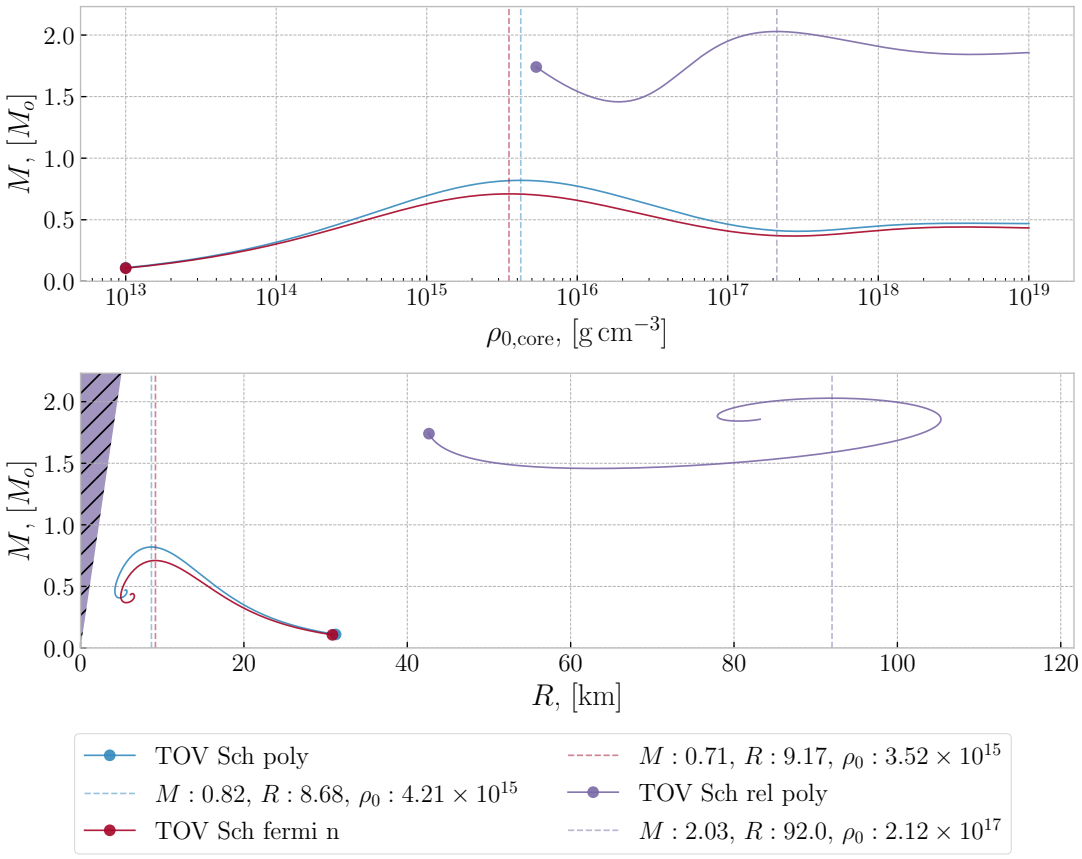

Figure 9.4: Parameterized total mass and radius for high densities comparing the polytropic formula and Fermi n EoS. Maximum mass, with corresponding radius and core rest mass density in vertical dashed lines.

within the limit for the ultra-relativistic approximation ($\rho_0 \gg 6 \times 10^{15}\,\text{g cm}^{-3}$). Note the interesting swirls in the $M(R)$ curves for high densities, present in each of the equations of state shown. The results are compared against schematic diagrams of similar curves in (Shapiro and Teukolsky, 1983, Figure 6.2 and 6.3), found to be in reasonable agreement. By studying the changes of sign in both $dM/d\rho_c$ and $dR/d\rho_c$ simultaneously, one can define restrictions on the stability of a system configuration. This is done by perturbing different oscillation modes around the minimum energy solution, i.e. equilibrium, and solving using a variational calculus principle. This is beyond the scope of this thesis, although the main takeaway is that $dM/d\rho_c > 0$ is required for stable equilibrium solutions for most cold EoS under general relativity. Therefore, we should not treat solutions found using core densities higher than the density corresponding to the maximum mass of each model as realistic to be observed in nature, and they are not dealt with by the cooling models as discussed in sections 6.1 and 8.3.2. This is also true at the low density end displayed for the ultra-relativistic approximation, where $dM/d\rho_c < 0$, indicating unstable solutions.

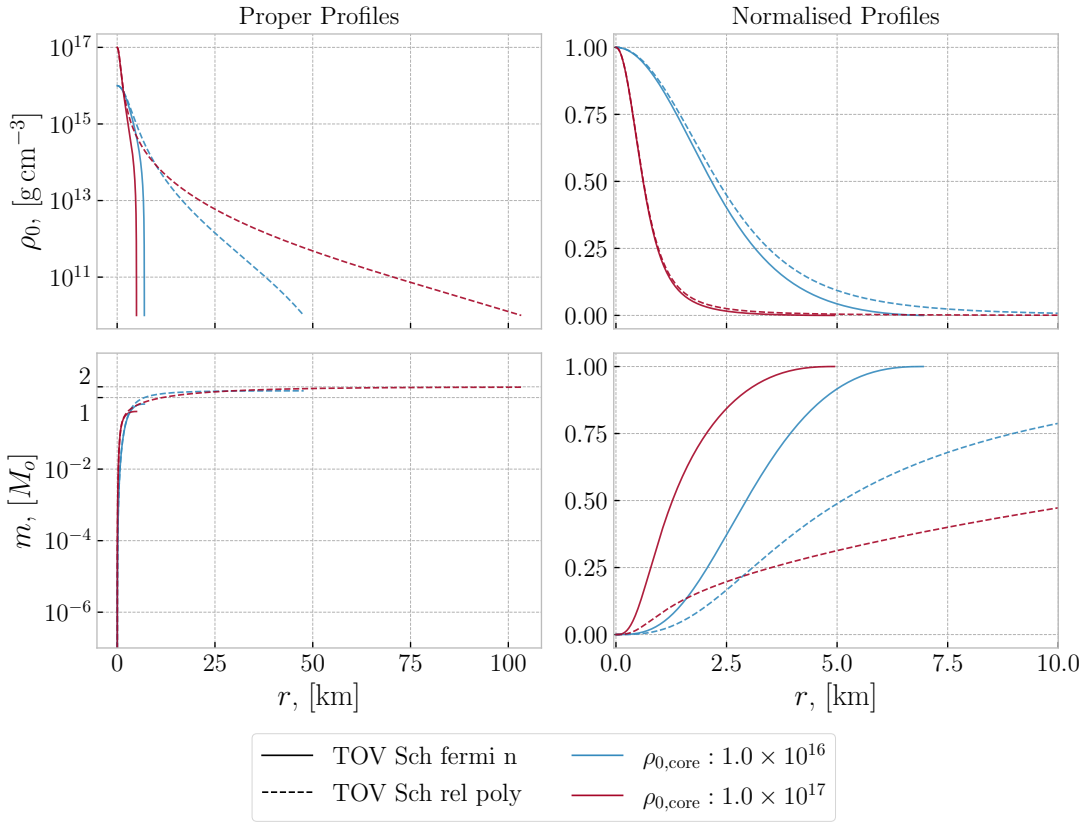

Figure 9.5: Mass and density profiles for comparison of the ultra-relativistic polytropic approximation (dashed) to the Fermi n EoS.Two high core densities are included to showcased the high density behavior, with the normalized profiles emphasizing the first 10 kms.

The max mass solution is also found to have an unusually large radius of $R = 92.05\,\text{km}$. As mentioned, stiffer equations of state tend to produce stars with higher mass and radius, which is not what we observe comparing the two polytropic versions. Again, we can understand this in terms of the issues already discussed for the non-relativistic limit, only reversed. Now, the polytropic formula accurately describes the behavior at the large densities close to the core, but fails dramatically when the density drops through the profile. We've highlighted this behavior in fig. 9.5, comparing the relativistic approximation to the Fermi EoS, where the right column is confined to only show the first 10 kms of the radius. Here we see the two equations of state following each other closely at the highest densities, but as mentioned, the polytropic version being too soft to produce a sufficient gradient near the surface. Thus, the solution requires a large radius to reach the desired surface density. We also suspect this problem of stability to be related to the Chandrasekhar limit of white dwarfs, where electron degeneracy is the source of the balancing pressure. By comparing the total internal and gravitational binding energies one finds that only for $\Gamma > 4/3$ are the system stable, and $\Gamma = 4/3$

marks the onset of unstable configurations as the EoS is too soft to equate the large gravitational potential.

9.3 First Cooling Results

In this first collection of results, we'll focus on two main features we've found regarding cooling. First, we'll argue for our previously mentioned, relatively bold statement – the way we initialize the assigned temperature profile of the star doesn't really matter. We've tried to visualize this in fig. 9.6, showing the profiled *redshifted* cooling curves of the maximum mass solution using the Fermi EoS for pure neutrons. In all of the following profiled cooling figures, we've used solid lines for the *boundary* temperature,[10] and so-called dashed-dotted lines for the core temperature. We include the quadratic profile in blue and the ideal gas-like profile in red, both with two initial boundary temperatures of $T_{b,init} = 10^9$ and $10^{10}\,\mathrm{K}$. Note how the exaggerated initial core temperature of the ideal gas-like profile is quickly cooled down to more reasonable values, caused by the high temperature dependency in the modified Urca emissivity. The integration is ended by the end time $t = 10^6\,\mathrm{yr}$ to highlight the initial phase before the solutions converge.

Keep in mind, the initial temperature profiles are constructed to have the same given input boundary temperature, and so the solid lines of fig. 9.6 appearing as purple is the result of the blue and red lines plotted on top of each other. They only differ in the interior temperature profiles, and with two profile types and two boundary temperatures, there are four different core temperatures in total. We are plotting both the core and boundary temperature, giving eight different curves in fig. 9.6. We therefore include the cooling curves normalized by initial temperature in the lower panel to show the relative behavior of each curve. Hopefully the message we are trying to convey is clear: all the mess at early times considered, arising from how we choose to initialize the temperature profile, have more or less disappeared within the first year of cooling. As we are interested in cooling curves on timescales of million years or so, this initial behavior is not that relevant. There's no change in the boundary temperature before the interior has cooled to $T_c < T_b$, when the boundary quickly catches up to the interior forming an isothermal star. We've chosen to use the redshifted temperature in this figure, to emphasize how the neutron star quickly finds an isothermal configuration. All the mentioned effects are similar for the proper temperature, but we would see a difference between the core and the boundary, separated by the constant value due to the redshifted transformation eq. (2.19). This is evident in all the remaining cooling figures, where we show the proper temperature.

The full cooling curves for the *npe* and *n* Fermi EoS is shown in fig. 9.7, with the quadratic initial temperature profile and boundary temperature of $10^{10}\,\mathrm{K}$. The

[10] Note, *not* the effective surface temperature. We'll show the effective surface temperature in the cooling figures of chapter 10 instead.

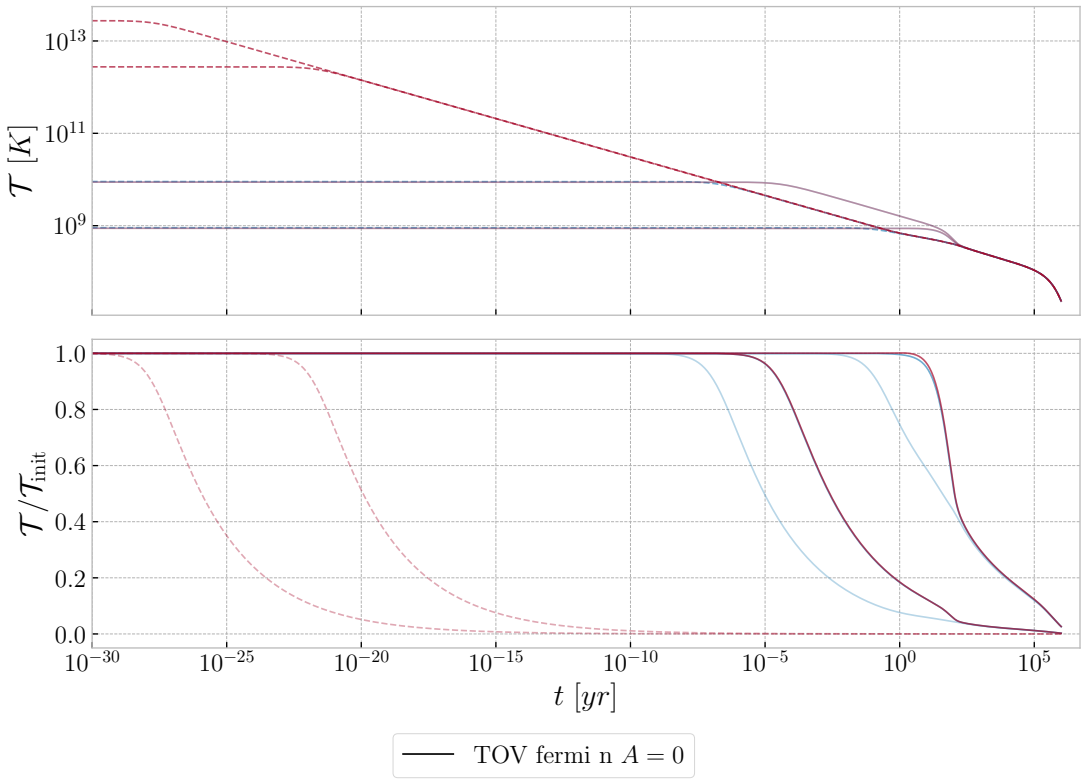

Figure 9.6: Demonstration of the convergence of different initial boundary temperatures and profiles for the Fermi n model with zero heating. The redshifted temperature is shown to emphasize the eventual isothermal profile. The 'ideal gas-like' profile in red, and the 'quadratic' in blue. Dashed lines indicate the core temperature. The line appearing as purple is the red and blue line overplotted.

results are consistent with (Shapiro and Teukolsky, 1983, Figure 11.2) in both the modified Urca- and photon dominated regime. Also in good agreement with (Page et al., 2006, Figure 15), where the photon dominated regime is reached after $t \sim 10^6$ yr for $T_c \lesssim 10^8$ K, as we have in our results. We see the same sort of behavior for both models, but with the neutron-only solution cooling more rapidly than the full npe gas.

This difference is most likely caused by the specific heat capacity being higher for the full npe-gas. Thus, more energy has to leave the star for it to cool, resulting in a less efficient cooling process. To quantify this discrepancy we list the specific heat averaged over the radial profile at $T = 10^{10}$ K in table 9.2, for the two models in fig. 9.7 of mass and radius listed in table 9.1.

Table 9.2: Specific heat capacity averaged over the radial profile comparing the pure neutron gas to the npe solution at $T = 10^{10}$ K. Note the *almost* one order of magnitude higher value for total specific heat capacity. The contribution from protons are $\sim 20\,\%$ of the total, consistent with rough estimates by Yakovlev and Pethick (2004). The electron contribution is a bit low at $\sim 1\,\%$ compared to the $\sim 5\,\%$ reported in the same source. All values in cgs-units $\left[\mathrm{erg\,cm^{-3}\,K^{-1}}\right]$.

Model	$\bar{c}_{v,\mathrm{tot}}$	$\bar{c}_{v,n}$	$\bar{c}_{v,p}$	$\bar{c}_{v,e}$
Fermi npe	1.94×10^{22}	1.37×10^{22}	3.66×10^{21}	2.02×10^{21}
Fermi n	3.63×10^{21}	3.63×10^{21}	-	-

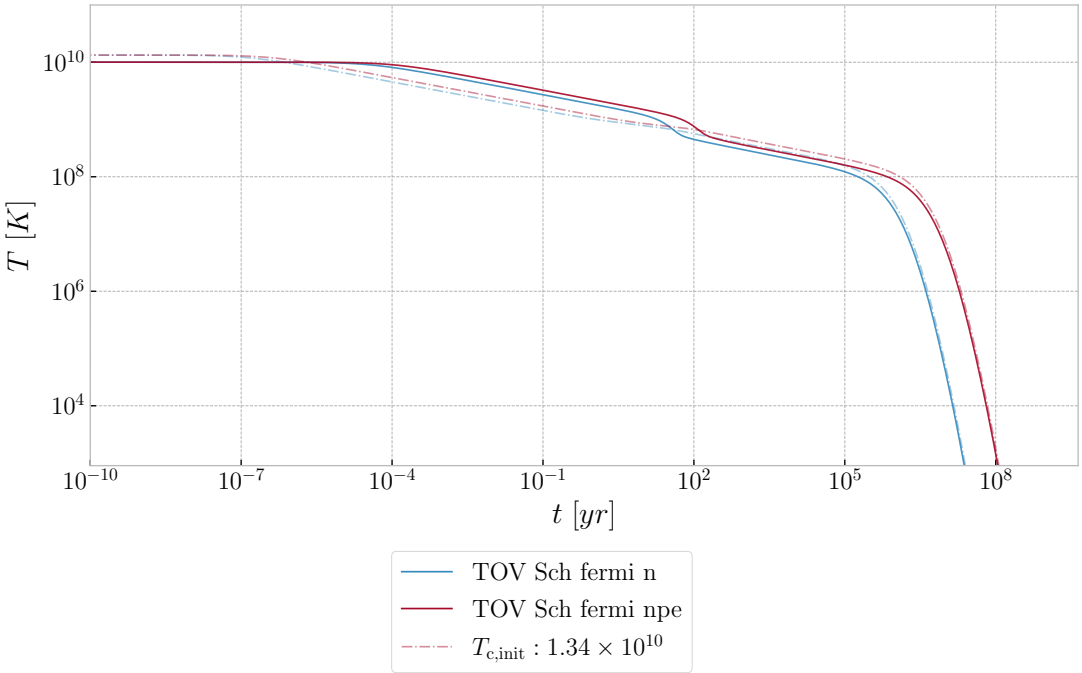

Figure 9.7: Cooling curves of the n (blue) and npe (red) Fermi EoS with quadratic initial temperature profile and $T_{b,init} = 10^{10}$ K. Solid lines for the boundary temperature, dashed for the core temperature. The photon dominated cooling regime is found to begin at $t \sim 10^6$ yr for $T_c \lesssim 10^8$ K.

Chapter 10

Most Noteworthy Results

We've chosen to gather the most interesting and realistic result obtained with the QMC EoS into this chapter. From the parameterized equation and fitting coefficients alone we are only able to scrape the surface of the intricate physics involved to discuss the equation of state when considering 2n and 3n interactions. A more detailed description of the 2n and 3n interaction energies is left for the nuclear particle physicists (Gandolfi, 2012), as we have focused more to provide a consistent framework for studying the cooling process of neutron stars. Full analysis of models under various realistic equations of state, the stability of the resulting neutron stars, and finally comparison to observations, are all subjects beyond the scope of this thesis. We'll come back to that in chapter 11, where we summarize some future prospects.

In this chapter we'll explore the same types of figures we saw in the first results in sections 9.2 and 9.3, all created with the `Plotter` class. For our purposes the general trends and behavior of the physical quantities, and how they affect each other, can be explained in a similar fashion as we did in chapter 9 in terms of the stiffness of the equation of state. As such we'll not spend too much time repeating the same arguments, but focus on the new and exciting results we find when including the heating rate due to WIMP annihilation.

10.1 Structure

Following section 3.4, the QMC EoS properly accounts for rest mass-, kinetic- and 2n interaction energy over the whole density interval we are looking at, but with varying contribution from the 3n potential between the different QMC models. We can again describe this in terms of the effective stiffness of the EoS. However, to compare the stiffness of the QMC EoS to that of the polytropic, we can't just look at the numerical value of α and β to that of Γ. Rather, the combined behavior of both terms in the

Table 10.1: Max mass solutions found for the QMC EoS plotted in fig. 10.1, in good agreement with Gandolfi (2012), and realistic equations of state described in (Shapiro and Teukolsky, 1983, Figure 9.2, 9.3 and table 9.1)

EoS	Max Mass	Radius	Core Density
QMC none	$1.76\,\mathrm{M}_\odot$	$8.16\,\mathrm{km}$	$2.88 \times 10^{15}\,\mathrm{g\,cm^{-3}}$
QMC 3	$2.22\,\mathrm{M}_\odot$	$9.94\,\mathrm{km}$	$1.89 \times 10^{15}\,\mathrm{g\,cm^{-3}}$
QMC 4	$2.08\,\mathrm{M}_\odot$	$9.77\,\mathrm{km}$	$2.04 \times 10^{15}\,\mathrm{g\,cm^{-3}}$
QMC UIX	$2.46\,\mathrm{M}_\odot$	$11.03\,\mathrm{km}$	$1.54 \times 10^{15}\,\mathrm{g\,cm^{-3}}$

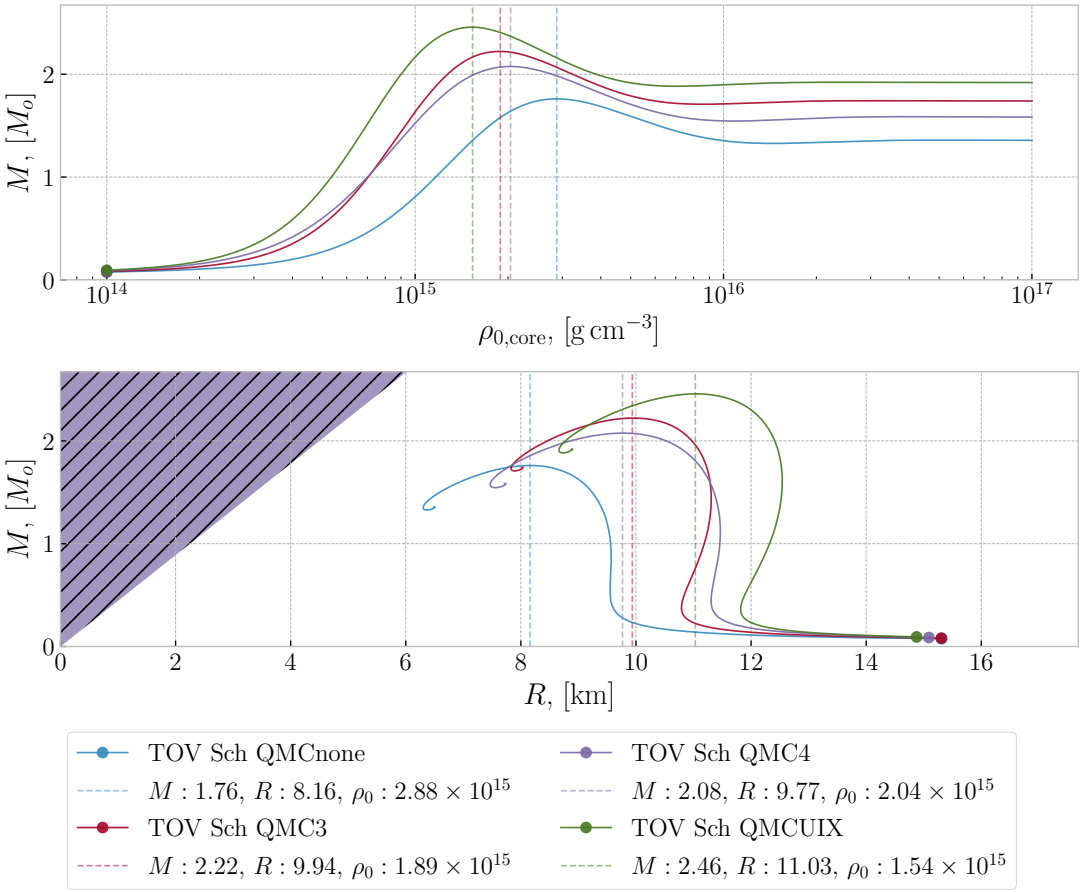

Figure 10.1: Parameterized max mass and radius found for the four QMC equations of state we showcase. The QMC none model with no 3n interaction, is in contrast to the QMC UIX model with the largest 3n contribution. In the middle of the two are the QMC 3 and QMC 4, having an interesting transition around $\rho_{0,\mathrm{core}} = 7 \times 10^{14}\,\mathrm{g\,cm^{-3}}$. The vertical lines mark the max mass solution, also listed in table 10.1.

QMC EoS must be considered, with the added effect of a and b. We summarized this effect when discussing the implementation and fig. 7.3. The main takeaway being, in contrast to the Fermi EoS, the QMC EoS is adjusted to be stiffer for higher densities. This is not surprising, as the EoS now includes not only the kinetic energy but also the interaction energies, both increasing with density. From chapter 9 we expect stiffer EoS to result in higher maximum masses achieved, as we see in table 10.1 and fig. 10.1. These results are in good agreement with Gandolfi (2012), and also comparable to other realistic equations of state we have yet to include described in (Shapiro and Teukolsky, 1983, Figure 9.2, 9.3 and table 9.1).

Here we've showcased the four models of the 3n potential we deem best to convey the general trend in all the different models, highlighting the most interesting differences, as discussed in section 3.4. The specific label names for different models in the particular order seen in table 3.1 reflects the effective stiffness of each model, starting with QMC none without any 3n interaction, followed by the numbered versions from 1 to 5, ending with QMC UIX. That is except for the QMC 3 and QMC 4 models, having an interesting transition around $\rho_{0,\text{core}} \sim 7 \times 10^{14}\,\text{g}\,\text{cm}^{-3}$ where QMC 3 start resulting in neutron stars with higher mass and radii compared to QMC 4 above this density. The structural profiles for for these two models are shown in fig. 10.2, where the transition is evident from the blue ($\rho_{0,\text{core}} < 7 \times 10^{14}\,\text{g}\,\text{cm}^{-3}$) to the red ($\rho_{0,\text{core}} > 7 \times 10^{14}\,\text{g}\,\text{cm}^{-3}$) curve. The really high densities shown in purple and green are very similar except really close to the core, where the highest density solution has a very dense core with a steep density and pressure gradient. Note however that these solutions are of core densities above the maximum mass solution, and should be further analyzed for stability.

We get additional insight when combining the proper profiles with the normalized columns, where again in contrast to Fermi Eos we see much more variety in the profiles for different densities. The normalization is done with respect to the initial density of each solution so we can see the relative behavior from the maximum to minimum of each curve throughout the profile, allowing us to compare the gradients and how the cumulative mass is distributed between neutron stars of different mass and radius. Restricting the discussion to the interesting transition at low densities, we see the same sort of behavior as we did when comparing the non-relativistic polytropic approximation to the full Fermi EoS in fig. 9.3. For $\rho_{0,\text{core}} = 10^{14}\,\text{g}\,\text{cm}^{-3}$, the QMC 4 model is the stiffest of the two, and thus we see the density to take higher values throughout the profile. This in turn causes the cumulative mass to increase more rapidly, and the density profile near the boundary to be steeper, resulting in a lower radius. The opposite is the case for the red curve, where $\rho_{0,\text{core}} = 10^{15}\,\text{g}\,\text{cm}^{-3}$ is above the transition taking place in the effective stiffness between QMC 3 and 4. This density is just below the one corresponding to maximum mass, which interestingly has a quite different shape for the profiles. Here we see the interior density being close to homogeneous before a substantial gradient is found and the boundary is reached. As such, the cumulative mass is distributed more evenly, which we can see from the normalized profiles.

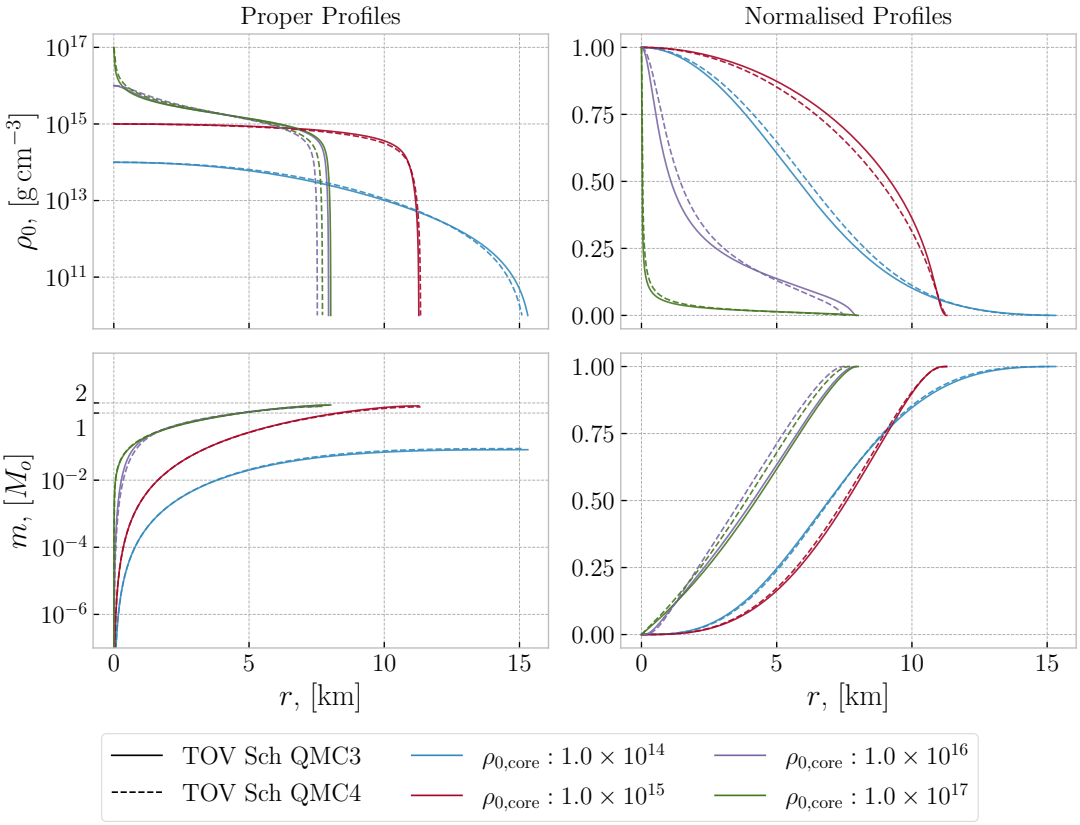

Figure 10.2: Structure profiles for the QMC3 and QMC4 EoS to accompany fig. 10.1, chosen to emphasize their differences at low and high densities.

10.2 Cooling to a Minimum Temperature

The cooling curves found with the QMC EoS share many similar features to the Fermi n solutions in regards to the shape, slope, and evolution of the temperature. We introduced this chapter claiming to focus on the new and exciting results we've found when including heating due to WIMP annihilation. Without further hesitation, we present the results in fig. 10.3. Here the boundary temperature is shown in the upper panel, and the observable effective surface temperature below, for a $M = 1.4 M_\odot$ neutron star constructed with the QMC none EoS in solid lines and the UIX in dashed. Both models are shown without any heating and for three different values of the local dark matter density. That is $\mathcal{A}_{\text{WIMP}} \in [0, 10, 100, 1000]$, where $\mathcal{A}_{\text{WIMP}} = 1 = 0.3\,\text{GeV}\,\text{cm}^{-3}$ is the estimated density of the dark matter halo here on earth. The three nonzero values for $\mathcal{A}_{\text{WIMP}}$ results in three plateaus of varied minimal temperature, listed in table 10.2 for both boundary and effective surface temperature.

In our search for cooling curves obtained by other numerical works to compare our

Table 10.2: Minimum temperature achieved when including WIMP heating in varied local dark matter densities for QMC none and UIX models, plotted in fig. 10.3.

	QMCnone		QMCUIX	
$\mathcal{A}_{\text{WIMP}}$	T_s, [K]	T_b, [K]	T_s, [K]	T_b, [K]
10	7.07×10^3	1.13×10^4	6.68×10^3	1.32×10^4
100	1.25×10^4	3.21×10^4	1.18×10^4	3.76×10^4
1000	2.24×10^4	9.13×10^4	2.11×10^4	1.07×10^5

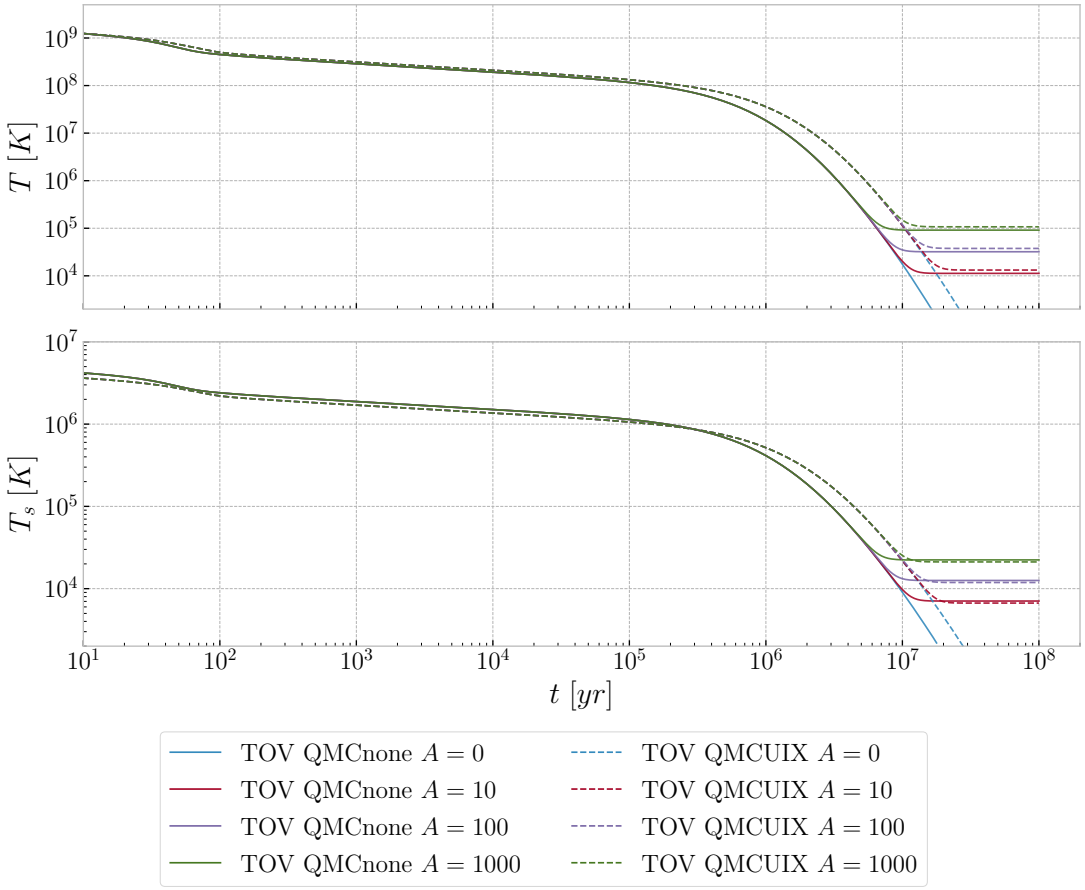

Figure 10.3: Cooling curves for $M = 1.4 M_\odot$ neutron stars with the QMC none (solid) and UIX EoS (dashed), quadratic initial temperature profile and boundary temperature of $T = 10^{10}$ K. The obtained solution without heating shown in blue crossing over the time axis approaching zero before the integration is ended. Three solutions with increasing dark matter halo densities, i.e. different radial distances from the center of the galaxy, are also included in red, purple and green.

profiled cooling results against we've mostly encountered much too simplified models, i.e. homogeneous cooling, or equally extensive profiled cooling models but with more physics included in the EoS and cooling mechanisms. As such we have no direct comparisons of the exact same configurations, we are mostly able to make qualitative comparisons. Disregarding the minimum temperature plateaus for now, the general trends and shape of our results seem to be in good agreement with several other sources with sophisticated cooling codes. For the first 10 million years the heating does not affect the temperature, we only see the other colored lines when the curves diverge at $t > 10^7\,\mathrm{yr}$, as they are «hidden» behind the green line. During the first $\sim 2 \times 10^5\,\mathrm{yr}$ the process is dominated by neutrino emission from the modified Urca reaction, before photon emission from the surface takes over. We've already mentioned and compared the cooling curves for the Fermi EoS with those of Page et al. (2004, 2006), and the results from the QMC models are equally comparable, if not better as we now are looking at neutron stars able to achieve the same mass. Similarly, we find our effective surface temperature to follow closely with theoretical and observational results for non-superfluid neutron models presented in Yakovlev and Pethick (2004); Yakovlev et al. (2008).

The most exciting feature we see in fig. 10.3 is how both models settle into similar minimum temperature plateaus. Remember, these are the results we found to emphasize the *difference* between the models. From fig. 10.1 we know a neutron star of the same mass constructed with the QMC none and QMC UIX models to have rather different radii, which in turn results in the largest discrepancy in the cooling process, also pointed out by Gandolfi (2012). That difference is only evident during times dominated by photon cooling, but before the point where the heating due to WIMP annihilation equates the cooling effect. By the time $t \sim 2 \times 10^7\,\mathrm{yr}$, both models find similar constant minimum temperatures. The resulting plateaus are consistent with the simple homogeneous cooling calculation performed by Kouvaris (2008), and comparable to the figures they present for both effective surface temperature and the boundary.

Lastly, we compared the results of the same EoS for two different total masses, both to test that they differ in the case of no cooling and if they are equal with heating. This is shown in fig. 10.4 for the QMC 4 model of mass $M = 1\,\mathrm{M}_\odot$ and $M = 1.6\,\mathrm{M}_\odot$, with no heating in the red lines and $\mathcal{A}_{\mathrm{WIMP}} = 10$ in the blue lines. From fig. 10.1 we know the QMC 4 model to have the most exaggerated differences in radii As expected, the result with no heating are found with different cooling efficiency, but the stable minimum temperature is equal for both models, suggesting that the specific temperature equating heating and cooling is insensitive to the total mass.

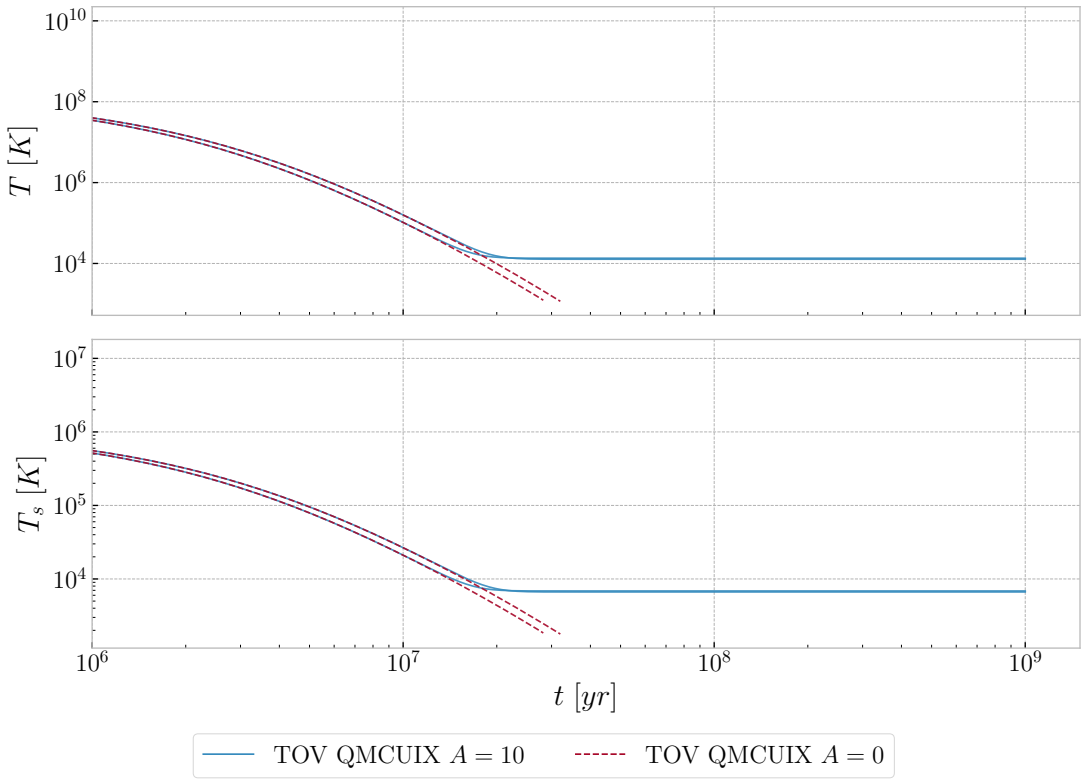

Figure 10.4: Cooling curves for the QMC UIX EoS of $M = 1.1\,\mathrm{M}_\odot$ and $M = 1.5\,\mathrm{M}_\odot$ with the quadratic initial temperature profile and boundary temperature of $T = 10^{10}\,\mathrm{K}$. We see the expected difference in long time cooling without heating for various mass and radius (Gandolfi, 2012). However, the minimum temperature seems rather insensitive to the total mass.

Chapter 11

Conclusion

We consider our goal of establishing an elegant framework designed to study neutron star structure and cooling as reached. As we've tried to emphasize throughout the thesis, the framework is probably one of a kind in terms of a closed system of logically structured and expandable modular code, treating the whole process of neutron star structure and cooling, with a variety of equations of state to chose from. Starting with determining the structural profiles by solving the TOV equations combined with the choice of EoS, and ending with a rather detailed profiled cooling of the newly obtained structure solutions – all in full general relativistic theory. Flexible and consistent utility functionality automatically handles the communication and plotting across the different modules, with multiple choices for numerical scaling bases and future expandability. The framework is intended as a tool to study the main features of neutron stars, producing results in good agreement with what we expect from qualitative and quantitative comparisons to other similar and sophisticated cooling codes. In our streamlined and simple code structure, the addition of further exotic equations of state considering additional particle- types, states, and phase transitions, is a simple case of finding sources defining the EoS through some sort of pressure-density relationship or parameterization. Again easily extended to the cooling scenario due to the interconnected nature of the modules in the framework, and the modular approach to the cooling and heating mechanisms.

During the time we've had to work on this project we've gathered experience from experimenting with the framework regarding some of the fundamental theory and physics thought to describe neutron stars. Starting with the equations governing the macroscopic structure in chapters 2 and 6, we learned how the relatively high mass and very low radius of neutron stars cause the fabric of our Universe to bend and distort in such a strong fashion that general relativistic adjustments to the classical Newtonian gravity must be considered. Gravitational effects are stronger in general relativity, expressed both through the spatial and temporal component of the metric describing the

geometry of spacetime, and so the required pressure to balance the crushing gravity is increased. This in turn causes neutron stars to have a maximum possible total mass achieved at a finite core density, solely determined by the choice of EoS. In chapters 3 and 7 we've laid out a brief introduction to the rather uncertain interior of neutron stars, and how we may describe properties of matter using equations of state of varied effective stiffness. The EoS eventually determines the resulting structure profiles and how the different fundamental variables are related throughout the radial profile, in turn dictating the achievable maximum mass and radius, as well as the radial distribution of particle number densities.

The last step of the process has been to consistently calculate the cooling curves of any given structural model, i.e. choice of EoS. This is concentrated into chapters 4 and 8 where we've learned how the number density of the involved particle species greatly affects the cooling process through the specific heat capacity and neutrino emissivity, and how the cooling can be separated into individual regimes dominated by a specific cooling mechanism. Early on, for high interior temperatures, we've seen how the modified Urca process is dominating and solely determines the temperature time evolution. And as the temperature drops, the efficiency of photon emission from the surface starts to exceed the neutrino cooling, eventually dominating the cooling process. Using our smoothed boundary definition we have a consistent foundation for the T_s-T_b relationships of any envelope model and how that relationships affects the surface luminosity. As such we are able to properly compare the cooling efficiency in the photon dominated regime for neutron stars of varied size - that is varied total mass and radius - constructed with both the same and different equations of state.

Lastly, we expanded the cooling module to include possible heating from dark matter, effectively testing the flexibility of the framework.[1] The implementation of the new heating mechanisms in the modular code proved to be very simple, and we found the resulting cooling curves to settle into stable minimum temperature plateaus when the heating effect equates the energy emitted by photons. Excitingly we found these plateaus to be relatively insensitive to the structure model both in terms of the EoS and total mass, possibly providing a measurable test versus observations of old and cold neutron stars.

11.1 Future Prospects

Although the models discussed in this thesis are by no means trivial, they are far from complete to describe a fully realistic neutron star with all its exotic properties. Some probable features of most neutron stars, like powerful magnetic fields strengths of $\sim 10^{12}\,\mathrm{Gs} = 10^{8}\,\mathrm{T}$ at the surface,[2] or rapid rotation periods of typically $\sim 0.5\,\mathrm{s}$,[3]

[1] We also discussed this flexibility considering the inclusion of protons and electrons [cf. section 8.3.5].

[2] Wheaton et al. (1979); Truemper et al. (1978).

[3] Much shorter periods are also observed, like the 1.558 ms period of PSR 1937+214 (Backer et al., 1982).

are needed to model exciting observed properties of pulsars. For a master project such as this one, designed to be a foundation for further expansion in terms of the uncertain nature of the theory, the list of future prospects and possibilities are only limited by the imagination. Here we summarize some of the most interesting and promising new physics we intend to include in the models, as well as some improvements to the framework regarding optimization and user-friendliness.

Firstly, the implementations of the coupled structural equations using TOV or Newton under our assumptions are by no means the limit of the model. As long as the fundamental physical quantities in the RHS may be expressed in terms of one-dimensional profiles, there are no constraints on the models we can define in `ns_models`. To study more exotic neutron star interiors, we can easily extend the collection of available equations of state and cooling scenarios in `eos_models` and `cooling_models` to include: additional states and phase transitions for the particles types already implemented, including neutron and proton superfluid configurations; additional particle species, including molecules near the surface, and possibly quark matter and other particles in the inner core; better estimates of the thermal conductivity across a wide range of densities, currently a lacking feature for the npe cooling model; as well as additional cooling processes such as fast and slow neutrino cooling by different types of Urca reactions.

In terms of improving the framework functionality, there are still some possible optimizations with respect to calculation times, mainly in the cooling calculations. Some of the first improvement that comes to mind is the discretization of the cooling grid. Instead of a linearly spaced grid, which we employed to ensure consistent calculation of the infinitesimal baryon number across possibly wildly different neutron star masses and metric functions, we could use a grid optimized to be denser in regions where most accuracy is required. To speed up the process of running many cooling calculations at once, we may scale the framework to run parallel on computers with more available cores, although the `solve_ivp` integration methods already spread the workload across multiple cores, expected to scale well. Another promising improvement is to wrap the demanding method looping the radial profile during cooling in a faster low level language like C using e.g. 'ctypes'. The plotter may also be extended to create more types of figures and accept additional customization options as input. One of the most interesting figures we would like to add is the specific heat contribution from each particle species throughout the radial profile. This brings us to the last improvement we mention here, which is to create a proper python package containing our framework available as a conventional python library, with a user-friendly API (Application Programming Interface). Some of the functionality intended in such an API is already ready, but separated over various scripts we've developed for our own use, and not at all error-proof for an uninitiated user. Hopefully, we'll get to all of these improvements in due time, allowing us to study the structure of neutron stars and how they cool in ever greater detail.

Appendices

Appendix A

Tables of constants and values

As we have experience some troubles when trying to reproduce results of other works as they are not specifying their numerical values used for various physical constants, we have concentrated all the constants as used in the code with numerical value and units in tables A.1 and A.2.

Table A.1: Numerical values of natural constants in cgs-units as used in the framework. These values are determined using the Astropy package CODATA 2018 collection (Astropy Collaboration, 2013, 2018).

Natural Constant	Interpretation	Used Numerical Value[†]
G	Gravitational constant	$6.674\,30 \times 10^{-8}\,\mathrm{cm^3\,g^{-1}\,s^{-2}}$
c	Speed of light	$2.997\,92 \times 10^{10}\,\mathrm{cm\,s^{-1}}$
$\hbar$	Reduced Planck constant	$1.054\,57 \times 10^{-27}\,\mathrm{erg\,s}$
m_n	Neutron mass	$1.674\,93 \times 10^{-24}\,\mathrm{g}$
m_p	Proton mass	$1.672\,62 \times 10^{-24}\,\mathrm{g}$
m_e	Electron mass	$9.109\,38 \times 10^{-28}\,\mathrm{g}$
m_u	Muon mass	$1.883\,53 \times 10^{-25}\,\mathrm{g}$
k_B	Boltzmann's constant	$1.380\,65 \times 10^{-16}\,\mathrm{erg\,K^{-1}}$
σ_SB	Stefan-Boltzmann's constant	$5.670\,37 \times 10^{-5}\,\mathrm{erg\,cm^{-2}\,K^{-2}\,s^{-1}}$

[†] To be precise, these values are as defined by the Astropy package, not meant to reflect the fundamental definition of the constants, such as e.g. the speed of light.

Table A.2: Auxiliary constants, intepretation and values in cgs-units. Combined quantities, e.g. λ_n, are found using the numerical value from table A.1. The solar mass and radius is found directly from the CODATA 2018 collection.

Auxiliary Constant	Interpretation	Used Numerical Value
$^{\dagger}\rho_{\mathrm{nuc}}$	Typical nuclear density	$2.800\,00 \times 10^{14}\,\mathrm{g\,cm^{-3}}$
$^{\ddagger}n_0$	Nuclear saturation QMC	$1.600\,00 \times 10^{38}\,\mathrm{cm^{-3}}$
$M_\odot$	Solar mass	$1.988\,41 \times 10^{33}\,\mathrm{g}$
$R_\odot$	Solar radius	$6.957\,00 \times 10^{10}\,\mathrm{cm}$
$R_{\mathrm{S}\odot} = 2\frac{GM_\odot}{c^2}$	Schwarzschild radius for one solar mass	$2.953\,25 \times 10^{5}\,\mathrm{cm}$
$\lambda_n = \frac{\hbar}{m_n c}$	Neutron compton wavelength	$2.100\,19 \times 10^{-14}\,\mathrm{cm}$
λ_p	Proton compton wavelength	$2.103\,09 \times 10^{-14}\,\mathrm{cm}$
λ_e	Electron compton wavelength	$3.861\,59 \times 10^{-11}\,\mathrm{cm}$

† Shapiro and Teukolsky (1983)
‡ Gandolfi (2012)

Bibliography

Astropy Collaboration
2013. Astropy: A community Python package for astronomy. A&A, 558:A33.

Astropy Collaboration
2018. The Astropy Project: Building an Open-science Project and Status of the v2.0 Core Package. AJ, 156(3):123.

Backer, D. C., S. R. Kulkarni, C. Heiles, M. M. Davis, and W. M. Goss
1982. A millisecond pulsar. Nature, 300(5893):615–618.

Bahcall, J. N. and R. A. Wolf
1965. Neutron Stars. II. Neutrino-Cooling and Observability. *Physical Review*, 140(5B):1452–1466.

Borriello, A. and P. Salucci
2001. The dark matter distribution in disc galaxies. MNRAS, 323(2):285–292.

Boylan-Kolchin, M., V. Springel, S. D. M. White, A. Jenkins, and G. Lemson
2009. Resolving cosmic structure formation with the Millennium-II Simulation. MNRAS, 398(3):1150–1164.

Chandrasekhar, S.
1939. *An Introduction to the Study of Stellar Structure*. Chicago, Illinois: University of Chicago Press.

Chiu, H.-Y. and E. E. Salpeter
1964. Surface X-Ray Emission from Neutron Stars. Phys. Rev. Lett., 12(15):413–415.

Einstein, A.
1905. Zur Elektrodynamik bewegter Körper. (German) [On the electrodynamics of moving bodies]. 322(10):891–921.

Einstein, A.
1915. Die Feldgleichungen der Gravitation. (German) [The field equations of gravitation]. Pp. 844–847.

Flowers, E. and N. Itoh
1981. Transport properties of dense matter. III - Analytic formulae for thermal conductivity. ApJ, 250:750–752.

Gamow, G.
1970. *My world line: An informal autobiography.*

Gandolfi, S.
2012. Maximum mass and radius of neutron stars, and the nuclear symmetry energy. *Physical Review C*, 85(3).

Gonzalez, D. and A. Reisenegger
2010. Internal heating of old neutron stars: contrasting different mechanisms. A&A, 522:A16.

Hobson, M. P., G. P. Efstathiou, and A. N. Lasenby
2006. *General Relativity: An Introduction for Physicists.* Cambridge University Press.

Jungman, G., M. Kamionkowski, and K. Griest
1996. Supersymmetric dark matter. Phys. Rep., 267:195–373.

Kouvaris, C.
2008. WIMP annihilation and cooling of neutron stars. Phys. Rev. D, 77(2):023006.

Navarro, J. F., C. S. Frenk, and S. D. M. White
1996. The Structure of Cold Dark Matter Halos. ApJ, 462:563.

Page, D., U. Geppert, and F. Weber
2006. The cooling of compact stars. Nucl. Phys. A, 777:497–530.

Page, D., J. M. Lattimer, M. Prakash, and A. W. Steiner
2004. Minimal Cooling of Neutron Stars: A New Paradigm. ApJS, 155(2):623–650.

Planck Collaboration
2016. Planck 2015 results. XIII. Cosmological parameters. A&A, 594:A13.

Schmidt, K. and S. Fantoni
1999. A quantum monte carlo method for nucleon systems. *Physics Letters B*, 446(2):99–103.

Shapiro, S. L. and S. A. Teukolsky
1983. *Black Holes, White Dwarfs, and Neutron Stars. The Physics of Compact Objects*, 1 edition. Wiley-VCH.

Thompson, S. P.
1897. Cathode Rays and Some Analogous Rays. *Philosophical Transactions of the Royal Society of London Series A*, 190:471–490.

Thorne, K. S.
1977. The relativistic equations of stellar structure and evolution. ApJ, 212:825–831.

Truemper, J., W. Pietsch, C. Reppin, W. Voges, R. Staubert, and E. Kendziorra
1978. Evidence for strong cyclotron line emission in the hard X-ray spectrum of Hercules X-1. ApJ, 219:L105–L110.

Tsuruta, S.
1974. Cooling of Dense Stars. In *Physics of Dense Matter*, C. J. Hansen, ed., volume 53, P. 209.

Tsuruta, S.
1979. Thermal properties and detectability of neutron stars. I. Cooling and heating of neutron stars. Phys. Rep., 56:237–277.

Van Rossum, G.
2020. *The Python Library Reference, release 3.8.2.* Python Software Foundation.

van Uitert, E., H. Hoekstra, T. Schrabback, D. G. Gilbank, M. D. Gladders, and H. K. C. Yee
2012. Constraints on the shapes of galaxy dark matter haloes from weak gravitational lensing. A&A, 545:A71.

Virtanen, P., R. Gommers, T. E. Oliphant, M. Haberland, T. Reddy, D. Cournapeau, E. Burovski, P. Peterson, W. Weckesser, J. Bright, S. J. van der Walt, M. Brett, J. Wilson, K. J. Millman, N. Mayorov, A. R. J. Nelson, E. Jones, R. Kern, E. Larson, C. J. Carey, İ. Polat, Y. Feng, E. W. Moore, J. VanderPlas, D. Laxalde, J. Perktold, R. Cimrman, I. Henriksen, E. A. Quintero, C. R. Harris, A. M. Archibald, A. H. Ribeiro, F. Pedregosa, P. van Mulbregt, and SciPy 1.0 Contributors
2020. SciPy 1.0: Fundamental Algorithms for Scientific Computing in Python. *Nature Methods*, 17:261–272.

Wheaton, W. A., J. P. Doty, F. A. Primini, B. A. Cooke, C. A. Dobson, A. Goldman, M. Hecht, S. K. Howe, J. A. Hoffman, A. Scheepmaker, E. Y. Tsiang, W. H. G. Lewin, J. L. Matteson, D. E. Gruber, W. A. Baity, R. Rotschild, F. K. Knight, P. Nolang, and L. E. Peterson
1979. An absorption feature in the spectrum of the pulsed hard X-ray flux from 4U0115 + 63. Nature, 282(5736):240–243.

Yakovlev, D. G., O. Y. Gnedin, A. D. Kaminker, and A. Y. Potekhin
2008. Theory of cooling neutron stars versus observations. In *40 Years of Pulsars: Millisecond Pulsars, Magnetars and More*, C. Bassa, Z. Wang, A. Cumming, and V. M. Kaspi, eds., volume 983 of *American Institute of Physics Conference Series*, Pp. 379–387.

Yakovlev, D. G. and C. J. Pethick
2004. Neutron Star Cooling. ARA&A, 42(1):169–210.

Zwicky, F.
1933. Die Rotverschiebung von extragalaktischen Nebeln. *Helvetica Physica Acta*, 6:110–127.